A CONCEPTUAL MODEL OF THE PILGRIM HOT SPRINGS GEOTHERMAL SYSTEM, SEWARD PENINSULA, ALASKA

By

Joshua K. Miller

RECOMMENDED:

Dr. Christian Haselwimmer, Committee Member

Dr. Ronald Daanen, Committee Member

Dr. Michael Whalen, Advisory Committee Co-Chair

Dr. Anupma Prakash, Advisory Committee Co-Chair

Dr. Sarah Fowell, Chair,
Department of Geology and Geophysics

APPROVED:

Dr. Paul Layer, Dean,
College of Natural Science and Mathematics

Dr. John Eichelberger, Dean of the Graduate School

Date

A CONCEPTUAL MODEL OF THE PILGRIM HOT SPRINGS GEOTHERMAL SYSTEM, SEWARD PENINSULA, ALASKA

A

THESIS

Presented to the Faculty

of the University of Alaska Fairbanks

in Partial Fulfillment of the Requirements

for the Degree of

MASTER OF SCIENCE

By

Joshua K. Miller, B.S. Geology

Fairbanks, Alaska

December 2013

Abstract

This work has developed a conceptual geological model for the Pilgrim Hot Springs geothermal system supporting the exploration, assessment and potential development of this resource for direct use and electric power production. The development of this model involved the analysis of a variety of subsurface and geophysical data and the construction of a 3D lithostratigraphic block model. Interpretation of the data and block model aimed to establish the most likely scenario for subsurface geothermal fluid flow. As part of this work well cuttings were analyzed for permeability and correlated with geophysical logs from well to well to constrain the stratigraphic architecture of the unconsolidated sediments. Hydrothermal alteration of the sediments and bedrock core was also studied through reflectance spectroscopy and methylene blue titration in order to investigate past fluid migration pathways. The structure of the basin was interpreted through geophysical surveys including aeromagnetic resistivity, isostatic gravity, and magnetotelluric resistivity. Based on temperature, well logs, geophysical surveys, and lithologic data, the system is subdivided into a shallow outflow aquifer and a deeper reservoir beneath a clay cap connected by a conduit with 91°C hydrothermal fluid upflow. Stratigraphic correlations indicate several clay layers throughout the section with a dominant clay cap at 200-275 m depth. Extensive pyritization and the clay mineral assemblage suggest an argillic-style alteration facies indicative of past temperatures at or slightly elevated above current conditions of hydrothermal activity at Pilgrim Hot Springs. The conceptual model supports production from this resource in those subsurface zones where there is sufficient permeability and connectivity with the upflow zone.

Table of Contents

Page

Signature Page ... i

Title Page ... iii

Abstract ... v

Table of Contents ... vii

List of Figures ... xi

List of Tables ... xv

List of Appendices ... xvii

Acknowledgements ... xix

Chapter 1: Introduction ... 1

1.1 Overview ... 1

    1.1.1 General Introduction ... 1

    1.1.2 Research Objectives ... 2

    1.1.3 Thesis Structure ... 3

1.2 Background ... 4

    1.2.1 Geothermal Systems and Geothermal Energy ... 4

    1.2.2 Alaska Geothermal Systems ... 5

    1.2.3 History of Exploration at Pilgrim Hot Springs ... 6

Chapter 2: Study Area ... 9

2.1 Pilgrim Hot Springs Location ... 9

2.2 Regional and Local Geology and Physiography ... 11

    2.2.1 Overview of the Regional Geology of Seward Peninsula ... 11

    2.2.2 Seismicity of the Seward Peninsula ... 13

    2.2.3. Surficial and Bedrock Geology of the Pilgrim River Valley 16

Chapter 3: Data and Data Products 19

3.1 Field Data 19

    3.1.1 Rock Sample Collection 19

3.2 Geophysical Data 21

    3.2.1 USGS Aeromagnetic and Electromagnetic (EM) Survey 23

    3.2.2 Magnetotelluric (MT) Resistivity Survey 26

    3.2.3 Ground-based Gravity Survey 32

3.3 Geoprobe Data 35

3.4 Drilling Data 37

    3.4.1. Sediment Characterization 37

    3.4.2 Geophysical Well Logs 42

    3.4.3 Static Temperature Logs 44

3.5 Sample Analytical Techniques 47

    3.5.1 Reflectance Spectroscopy 47

    3.5.2 Methylene Blue Titration 57

    3.5.3 X-ray Diffraction Analysis 59

    3.5.4 Thin-section Characterization 62

3.6 Discussion of Analytical Results 64

Chapter 4: Lithostratigraphic and Temperature Model Development 70

4.1 RockWorks15 Model Parameters 70

4.2 Model Assumptions and Limitations 72

4.3 Data Integration 73

    4.3.1 Lithostratigraphic Model 73

4.3.2 Temperature Model..78

Chapter 5: Development of the Conceptual Model 85

5.1 Introduction...85

5.2 Discussion of the Conceptual Model 87

5.3 Conceptual Model in a Regional Context..106

Chapter 6: Conclusions and Recommendations 113

6.1 Conclusions...113

6.2 Recommendations..114

References...117

Appendices...125

List of Figures

Page

Figure 2.1: Pilgrim Hot Springs location map with wells 10

Figure 2.2: Seismicity map of central and western Alaska..15

Figure 2.3: Surficial and bedrock geology map of the Pilgrim River Valley....................18

Figure 3.1: Place map of rock sample locations 20

Figure 3.2: Logarithmic scale of resistivity values for geologic materials........................22

Figure 3.3: Flight path for aeromagnetic and electromagnetic survey 24

Figure 3.4: Different resistivity map at 20 m depth...25

Figure 3.5: Locations of magnetotelluric resistivity recording stations 28

Figure 3.6: Magnetotelluric resistivity profile line D..29

Figure 3.7: Magnetotelluric resistivity profile line C 30

Figure 3.8: Magnetotelluric resistivity profile line 2..31

Figure 3.9: Isostatic gravity survey station location map 33

Figure 3.10: Isostatic gravity anomaly map of the Pilgrim River Valley..........................34

Figure 3.11: Well and Geoprobe hole location map 36

Page

Figure 3.12: Logarithmic chart of particle diameter by sediment type.............................41

Figure 3.13: Lithologic and gamma ray logs for selected wells.......................................43

Figure 3.14: Temperature curves for all Pilgrim Hot Springs wells.................................45

Figure 3.15: Lithology, gamma ray, and temperature curves for selected wells...............46

Figure 3.16: AlOH and FeOH absorption features..48

Figure 3.17: Hyperspectral image cube of PS-12-2...51

Figure 3.18: The Spectral Geologist spectral analysis mineral results.............................52

Figure 3.19: White Mica Alteration Index scatter plot for PS-12-2.................................55

Figure 3.20: White Mica Alteration Index scatter plot for selected wells.........................56

Figure 3.21: Methylene blue solution halos..58

Figure 3.22: XRD results of PS-12-2 clay samples..61

Figure 3.23: Thin-section photomicrographs of bedrock core samples.............................63

Figure 3.24: AlOH absorption depths and methylene blue results combined plot............66

Figure 3.25: Lithology, temperature, spectral, and methylene blue analysis plot.............67

Figure 4.1: RockWorks15 conceptual model dimensions...71

Page

Figure 4.2: Southwest-northeast cross-section of interpolated lithologic logs 75

Figure 4.3: RockWorks15 3D model of the interpolated lithologic logs 76

Figure 4.4: RockWorks15 3D model of major clay intervals and indurated zone 77

Figure 4.5: Southeastern view of the RockWorks15 temperature model 80

Figure 4.6: Vertical and horizontal slices of the RockWorks15 temperature model.........81

Figure 4.7: Three depth maps of the RockWorks15 temperature model result 82

Figure 4.8: Two cross-sections of the RockWorks15 temperature model.........................83

Figure 5.1: Stratigraphic cross-section of the geologic model with isotherms..................88

Figure 5.2: AlOH absorption and methylene blue results plotted on MT profile.............90

Figure 5.3: MT and RockWorks15 temperature model plan maps at 50 m depth............92

Figure 5.4: MT and RockWorks15 temperature model plan maps at 100 m depth...........93

Figure 5.5: MT and RockWorks15 temperature model plan maps at 200 m depth...........94

Figure 5.6: MT and RockWorks15 temperature model plan maps at 300 m depth...........97

Figure 5.7: Simple conceptual model cross-section utilizing the W-E Profile D of the MT survey 102

Figure 5.8: 3D MT Profile 3 overlaid with lithostratigraphy...103

Figure 5.9: USGS airborne electromagnetic resistivity survey of the Pilgrim River Valley surrounding the hot springs area 105

Figure 5.10: Interpreted basin cross-section of the Pilgrim River Valley 108

Figure 5.11: Location map of inferred transfer fault 111

Figure C.1: X-ray diffraction results of glycolated clay samples for well PS-12-1 130

Figure C.2: X-ray diffraction results of glycolated clay samples for well PS-12-2 131

Figure C.3: X-ray diffraction results of glycolated clay samples for well PS-12-3 132

List of Tables

Page

Table 3.1: Average porosity values for sediment size and sorting 39

Table 3.2: Grain diameter and intrinsic permeability by sediment type...........................40

Table A.1: Mineral abundance for PS-12-1 125

Table A.2: Mineral abundance for PS-12-2 125

Table A.3: Mineral abundance for PS-12-2 core 126

Table A.4: Mineral abundance for PS-12-3 126

Table B.1: Estimated smectite content per sediment sample for PS-12-1 127

Table B.2: Estimated smectite content per sediment sample for PS-12-2 128

Table B.3: Estimated smectite content per sediment sample for PS-12-3 129

List of Appendices

Page

Appendix A: Spectral assessment of mineral abundances....................................125

Appendix B: Methylene blue (MeB) titration results 127

Appendix C: X-ray diffraction results of glycolated clay samples.........................131

Acknowledgements

I am privileged to have experienced such a wonderful collection of people and organizations in my time at the University of Alaska Fairbanks. I would first like to thank my committee members Dr. Anupma Prakash, Dr. Christian Haselwimmer, Dr. Ronald Daanen, and Dr. Michael Whalen for their constant support and direction through the process of completing this thesis research. I would like to thank Gwen Holdmann and the rest of the Alaska Center for Energy and Power organization for the opportunities I have been able to enjoy ranging from fieldwork at Pilgrim Hot Springs, support during my research, and travel to Iceland and other places. I want to acknowledge Lesli Walls and Markus Mager for going well beyond their respective roles in the project to offer any help I needed as well. The funding agencies that allowed for me to participate in this project also deserve my gratitude: Department of Energy Geothermal Technologies Program (CID: DE-EE0002846) and the Alaska Energy Authority Renewable Energy Fund Round III. I want to thank all those involved in the project who have offered vast amounts of constructive advice including Bill Cumming, Dick Benoit, Art Clark, and Ralph Wilcox. I appreciate all of the help I received from other students who were involved in this project: Charles Parr and Zachary Woodbury. I'm also appreciative of the lab support given by Dr. Tom Trainor, Dr. Franta Majs, Susana Salazar Jaramillo, and the Advanced Instrumentation Lab at UAF. Finally, I want to acknowledge my appreciation for the support of my family, friends, and colleagues at the UAF Department of Geology and Geophysics, UAF Geophysical Institute, as well as other organizations including the Institute of the North and the Alaska Division of Geological and Geophysical Surveys.

Chapter 1: Introduction

1.1 Overview

1.1.1 General Introduction

Alaska is known for its richness in many resources such as oil, gas, and valuable ore deposits. One marginalized resource under renewed state-wide scrutiny is geothermal energy. Ultimately, the goal for exploration of geothermal resources is electric power production or direct use for the nearby communities. The geothermal system being evaluated for this research is Pilgrim Hot Springs located on the Seward Peninsula. The University of Alaska Fairbanks Geophysical Institute, Alaska Center for Energy and Power, Alaska Division of Geologic and Geophysical Surveys, and private contractors have mapped, drilled, and sampled the site over a period of 30 years.

Contributions of this research will provide a concise geologic assessment of the Pilgrim Hot Springs geothermal system helping to determine the viability of this resource. A conceptual model, the end result of this work, is needed to evaluate the potential for geothermal resource development by guiding future exploration of the system. Stratigraphy of the sediments and proximal structures will be shown through well log correlations. Subsurface conduits for geothermal fluid migration will be ascertained through temperature distributions, magnetotelluric (MT) and other geophysical survey maps, and stratigraphic correlations. Characterization of hydrothermal alteration in the collected samples and bedrock core will be fulfilled through multiple analytical methods. The final model will be the combination of a wide range of collected data and derived data products which will also serve to complement and inform the numerical model for reservoir simulation and stimulation model scenarios.

1.1.2 Research Objectives

The hypothesis for this research is that Pilgrim Hot Springs can be an economically viable geothermal resource for both direct-use applications and electric power production. The desired outcome of the conceptual model is locating the deeper reservoir of hot fluids feeding the upflow from the bedrock through the synthesis of high-resolution MT survey maps, interpreted stratigraphy and structure, and temperature distributions. The conceptual model will also serve to direct the orientation and placement of proposed thermal conduits at depth. To test this hypothesis, several objectives have been proposed below:

- Describe sediment samples of five exploratory wells and estimate porosity and permeability.
- Correlate gamma ray and induction well logs to understand stratigraphic architecture.
- Assess the temperature distribution across the wells to model the mass transfer, thermal buoyancy, and transmissivity of upwelling hydrothermal fluids that interact with hydrologic barriers.
- Evaluate MT resistivity and other geophysical survey data to constrain the spatial extent of the geothermal system.

- Investigate the degree of hydrothermal alteration in clays to infer past hydrothermal activity at the site.
- Incorporate these data sets into a conceptual model of the geologic framework of the geothermal system.

1.1.3 Thesis Structure

The structure of this thesis research describes the construction, results, and interpretations of the conceptual model of the geologic framework of the Pilgrim Hot Springs geothermal system. The first chapter introduces the project and provides background information on geothermal systems and conceptual model development. Chapter two describes the geologic and physiographic setting of Pilgrim Hot Springs. The third chapter lists the data sets used in this research, along with methods used to derive data products as model inputs. The fourth chapter is the conceptualized geologic model that covers the development, inherent assumptions, limitations, and interpretations of the model. A discussion of marrying the data sets, sediment analysis results, and the conceptual model is provided in the fifth chapter. The final chapter emphasizes the principal findings of this research by reiterating the significance of the model results and also suggests future applications for this project.

1.2 Background

1.2.1 Geothermal Systems and Geothermal Energy

Glassley (2010) explains that geothermal energy and systems exist as interactions of heat escaping from the planet's interior to the outer crust. The heat, derived from early planetary formation and radioactive decay, can produce such features as hot springs, fumeroles, geysers, or sometimes no surface expression at all as in the case of blind geothermal systems. Total heat loss can be quantified for the entire Earth's surface and areas of elevated or anomalous heat flow may form a geothermal system. Different geologic settings contribute to the existence of geothermal systems. Regional extension of a continental plate thins the lithosphere resulting in a higher heat flow near the earth's surface. Intrusion of magmatic or plutonic bodies along fractures or fault systems conducive for the migration of heated fluids may also induce thermal springs. The energy of a geothermal system is transferred through conduction and convection processes. Conduction of heat occurs in low permeability settings such as a pluton or fine-grained sedimentary basin whereas convection cells are restricted to higher permeability pathways allowing for thermal buoyancy of geothermal fluids and significant thermal expansion which initiates hydrothermal systems (Glassley, 2010; Kolker et al., 2008). Several geologic settings conducive for low-high enthalpy geothermal systems exist within Alaska.

1.2.2 Alaska Geothermal Systems

Alaska contains abundant geothermal resources located in the Aleutian volcanic arc, south central Alaska, the southeastern Panhandle, and interior Alaska south of the Brooks Range. The Aleutian Islands have the greatest potential in Alaska for geothermal development as a result of Pacific plate subduction beneath North America (Swenson et al., 2012). The heat that fuels the hydrothermal activity is derived from magmatic bodies at depth generated through the melting of a subducting plate. Twelve hot springs have temperatures greater than 74°C, whereas only five springs of similar temperatures are located within mainland Alaska (Swenson et al., 2012). Several of these springs along the Aleutians produce surface discharge temperatures as high as 152°C and geothermometry estimates of reservoir temperatures up to 300°C (Swenson et al., 2012). Hot springs outside of the volcanic arc are typically low-moderate temperature systems with predicted reservoir temperatures of less than 150°C (Swenson et al., 2012). Kolker et al. (2008) concluded that within interior Alaska, with over 30 known hot springs, the principal sources of heat are proximal shallow high heat producing plutons, which was based on helium isotope studies. The regional tectonics resemble a backarc fault-block rotation in the eastern and central interior as suggested by Page et al. (1995) that provides the necessary fracturing for hydrothermal convection cells. However, the western interior/Seward Peninsula exhibits a different structural style related to the strongly transtensional tectonic regime (Biswas et al., 1986; Cross and Freymueller, 2008; Mackey et al., 1997; Ruppert, 2008). Geothermal systems associated with crustal extension are typified by deep convection cycles, circulating groundwater into and out of the heat source along major normal fault systems that feed shallow reservoirs (Blackwell and Kelley, 1994; Kolker et al. 2008). Although the heat source remains elusive, a similar process is proposed for the Pilgrim Hot Springs geothermal system (Chittambakkam et al., 2013; Miller et al., 2013).

1.2.3 History of Exploration at Pilgrim Hot Springs

Pilgrim Hot Springs is located 96 km north of Nome, Alaska, and ~120 km south of the Arctic Circle in central Seward Peninsula. This region, principally the city of Nome, is in dire need of a low-cost, reliable alternative source of energy as opposed to costly imported diesel fuel. Also included in the energy demand are local mining operations. This geothermal anomaly has been known by the native community for centuries and locals have used the site since the early 20th century as a Catholic mission. Over the past 30 years, several exploration programs have been aimed at evaluating the site for its potential as an energy source.

There is a long history of exploration and assessment of the geothermal system at Pilgrim Hot Springs. Initially, the University of Alaska Fairbanks Geophysical Institute in cooperation with the Alaska Division of Geological and Geophysical Surveys provided a report to the U.S. Department of Energy on the geothermal energy potential of Pilgrim Hot Springs (Turner and Forbes, 1980). This work was completed in 1979 and involved mapping the regional surface and bedrock geology, geochemistry of the springs, possible radiogenic heat from nearby plutons, and geophysical surveys of the area. The map produced from the study indicated normal faulting along the Kigluaik Mountains to the south as well as faults present across the basin evidenced by terraces and scarps in the adjacent hills. A radiogenic heat source was discounted after analyzing the mineralogy of the local intrusives and finding no elevated ratio of Th/U. Well testing of two 50 m wells, drilled during the 1979 exploration work, allowed estimates of permafrost depths to 100 m and established a local temperature gradient of up to 91 °C. Geochemical studies found the fluid composition to be alkali-chloride rich with dissolved carbon dioxide and hydrogen sulfide. Oxygen isotope and deuterium analysis suggested deep-seated water-rock reactions. The high-salinity and dissolved gases suggested a volcanic origin and a source temperature of ~130 °C. Geophysical surveys, resistivity and gravity, indicated a 1.5 km^2 reservoir and a downthrown block of basement to the southwest edge of the thawed ground bounded by intersecting faults at depth immediately below the springs. The recommendations from this study are complemented by exploration well data of the second phase of evaluation and are described below.

Early resource exploration, by the University of Alaska Fairbanks and Woodward Clyde Consultants, sought to determine the viability of Pilgrim Hot Springs as an energy resource (Woodward-Clyde, 1983). Initial temperature gradient wells were drilled in 1979, then resumed in 1982 with four wells of depths ranging from ~60-300 m. Drilling targets for the 1982 program were based on the earlier 1979 field work to demonstrate the extent of the resource. Wells were designed to provide detailed information on temperature variations and act as geothermal supply wells. The temperature gradients from the wells drilled from 1979-1983, coupled with soil-helium surveys, extrapolated the deeper reservoir to be 150°C at 1500 m depth. The total baseload energy that can be derived from the hot springs was estimated at 1.5 MW based on a flow of 240 gpm at 90°C (Woodward-Clyde, 1983).

Recent exploration of Pilgrim Hot Springs is the product of collaboration between the Alaska Center for Energy and Power and the Geophysical Institute (University of Alaska Fairbanks). The project is testing the application of remote sensing using Forward Looking Infrared Radiometer (FLIR) to reduce the cost of preliminary geothermal exploration by quantifying geothermal surface heat losses. Five exploration slimhole wells were drilled (in addition to the existing six wells mentioned above) with two wells at ~150 m, two wells at ~300 m depth, and one at ~400 m. Over sixty shallow Geoprobe temperature gradient holes were drilled and both airborne and ground resistivity surveys at the site were also conducted. These data sets provide input to construct an improved conceptual model of the PHS geothermal system.

Chapter 2: Study Area

2.1 Pilgrim Hot Springs Location

Pilgrim Hot Springs is located on the Seward Peninsula in western Alaska, less than 200 km south of the Arctic Circle (Figure 2.1). The springs are within an alluvial basin in tundra underlain by discontinuous permafrost that is bounded by the glacially-eroded Kigluaik Mountains to the south and two prominent hills to the north, Marys Mountain and the Hen and Chicken Mountains. The basin is dissected by the east to west meandering Pilgrim River that borders the thawed ground of the springs, which occupies an ~1.5 km^2 area. The thawed ground is associated with anomalous vegetation that includes cottonwood trees, alders, grass, and various flowers. The site lies only a few meters above sea level and elevation changes are small.

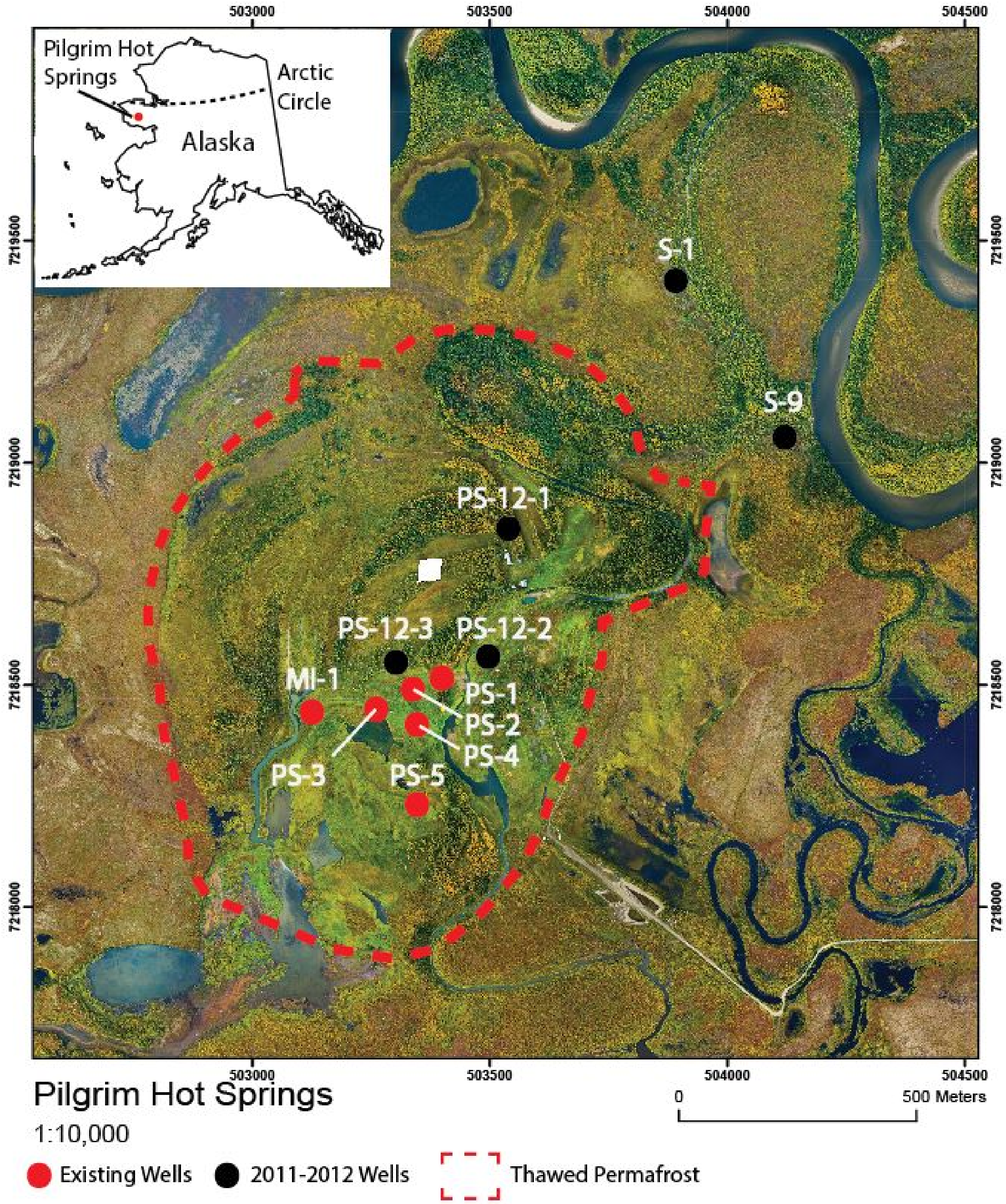

Figure 2.1: Pilgrim Hot Springs location map with wells. Map shows the distribution of wells, the boundary of discontinuous permafrost, and the extent of the thawed ground anomaly (Miller et al., 2013). Optical imagery modified from Haselwimmer et al. (2011).

2.2 Regional and Local Geology and Physiography

2.2.1 Overview of the Regional Geology of the Seward Peninsula

As summarized by Till and Dumoulin (1994), the Seward Peninsula is composed of two major geologic terranes: the older Seward terrane and the younger York terrane. Located in the central and eastern peninsula, the Seward terrane comprises Precambrian-early Paleozoic blueschist-, greenschist-, and amphibolite-facies schist and marble, and localized granitic intrusions. The York terrane is located in the western peninsula and along the Bering Straits and is comprised of Ordovician-late Cretaceous limestone, dolostone, phyllite, and local granite. The extent and contact of the terranes is marred by complex faulting, including the north-trending, east-vergent Koyuk-Kugruk fault zone in eastern Seward Peninsula, with possible thrusting between the terranes. Specifically, within the Seward terrane is the Nome Group, which contains a regionally extensive metamorphic stratigraphy of pelitic schist, interlayered marble and quartz-graphitic schist, a mafic schist, and impure chloritic schist. These units were exposed to high pressure-temperature blueschist metamorphism (~34-42 km burial) in the pre-Late Jurassic coeval with a similar event in the western Brooks Range. Greenschist metamorphism progressively overprints blueschist rocks to the south and also records a major deformational event that resulted in the north-south lineated isoclinal foliations of the Nome Group. This deformational event is related to Cretaceous magmatism, sharing a comagmatic history with plutonism throughout central Alaska and extending far into eastern Siberia, represented by local Cretaceous granite and gneiss intrusives referred to as the Kigluaik Group.

The Kigluaik Mountains to the south of Pilgrim Hot Springs formed as a result of regional extension as an ascending intermediate mantle-derived magmatic diapir intruded and overprinted locally hot blueschist-facies rocks of the Nome Complex as indicated by a peripheral lack of quench textures (Amato et al., 1994; Amato et al., 2002; Amato et al., 2003; Amato et al., 2009; Amato and Miller, 2004). A granitic cap overlies the intermediate core of the pluton and is emplaced within metasedimentary rocks that grade from amphibolite to granulite facies toward the outer flanks of the mountain (Amato et al., 1994; Amato et al., 2003; Till et al., 2011). Ages obtained from U-Pb dating of zircons within the Kigluaik pluton reveal crystallization around 91 Ma (Amato et al., 1994; Amato et al., 2003; Till et al., 2011). The contact between the two groups is faulted (Till and Dumoulin, 1994). Alkalic and tholeiitc basalts from the Cenozoic basalt maar field in central and northern Seward Peninsula indicate recent volcanic activity (Beget et al., 1996; Turner and Swanson, 1981). The maar craters are the result of a particularly explosive combination of basalt eruption into overlying permafrost (Beget et al., 1996). The craters are dated to Pleistocene age and as young as 17500 years B.P. based on radiocarbon dating and tephrachronology (Beget et al., 1996).

The Kigluaik Mountains and surrounding exposures of bedrock have been subject to several intervals of Quaternary glaciation (Brigham-Grette, 2001; Calkin et al., 1998). A major advance of glaciation, the Nome River event, occurred between 580,000 and

280,000 yr ago and covered an area that stretched past Nome (Calkin et al., 1998). Several smaller advances have been noted for the Mid-Late Wisconsin glaciations and Holocene (Barclay et al., 2009; Calkin et al., 1998).

2.2.2 Seismicity of the Seward Peninsula

Seismicity and Holocene fault displacement across the Seward Peninsula is dominantly manifested by east-striking normal faulting with northwest-southeast extension, principally on the Kigluaik and Bendeleben faults (Biswas et al., 1986, Biswas and Tytgat, 1988; Cross and Freymueller, 2008; Finzel et al., 2011; Mackey et al., 1997; Page et al., 1991; Ruppert, 2008; Turner and Swanson, 1981). Seismicity across western Alaska appears diffuse and lacking any linear trends suggesting widespread movement across many active faults (Page et al., 1991). Semi-clustered activity of <2.0 M earthquakes around the Kilguaik fault occurs both north and south of the fault with uncertainty if the epicenters occur directly on the fault (Page et al., 1991). This region displays southeast-directed motion with a southwestern rotation into the Bering Sea (Cross and Freymueller, 2008; Finzel et al., 2011). The movement is attributed to the proposed Bering plate model (Cross and Freymueller, 2008). The Bering plate is defined as a clockwise-rotating, large rigid plate evidenced by GPS measurements and seismicity studies (Cross and Freymueller, 2008). The Bering plate appears to be rotating south-southwest relative to the North American plate along the eastern margin of the Bering Sea (Cross and Freymueller, 2008). The Bering plate is inferred to have a diffuse northern boundary cross-cutting the Seward Peninsula and is hinged on the Kigluaik and

Bendeleben faults (Cross and Freymueller, 2008; Fujita et al., 2002). This rotation could mark the boundary of the interpreted Bering plate. This could explain the continued extension in Seward Peninsula that extends as far inboard as the western Brooks Range (Finzel et al., 2011). Dumitru et al. (1995) proposed western Alaskan extension as accommodation for western movement of crustal fragments from interior and southern Alaska, although that is questioned by Finzel et al. (2011). A large mantle flow field or interacting microplates west of the Bering Sea may also impact ongoing western Alaska extension (Finzel et al., 2011). Regardless, continued southwestern rotation-induced tensional earthquakes coupled with Holocene offset of up to 10 m along faults in the region and the recent basaltic volcanism lends evidence to the proposed incipient rift model of Turner and Swanson (1981). Sampled alkali and tholeitic basalts from central and western Seward Peninsula reflect variable assimilation of ascending magma with country rock due to relatively rapid vertical movement common in back-arc environments (Turner and Swanson, 1981). Regional tectonic extension is evidenced by normal displacement along major faults in the Seward Peninsula. Combined with elevated heat flow throughout central Seward Peninsula, Turner and Swanson (1981) proposed a rift-related model for the sedimentary basins on the Seward Peninsula. The model is set in a back-arc extensional environment related to the Aleutian volcanic arc. This could explain the anomalous geothermal activity seen at Pilgrim Hot Springs.

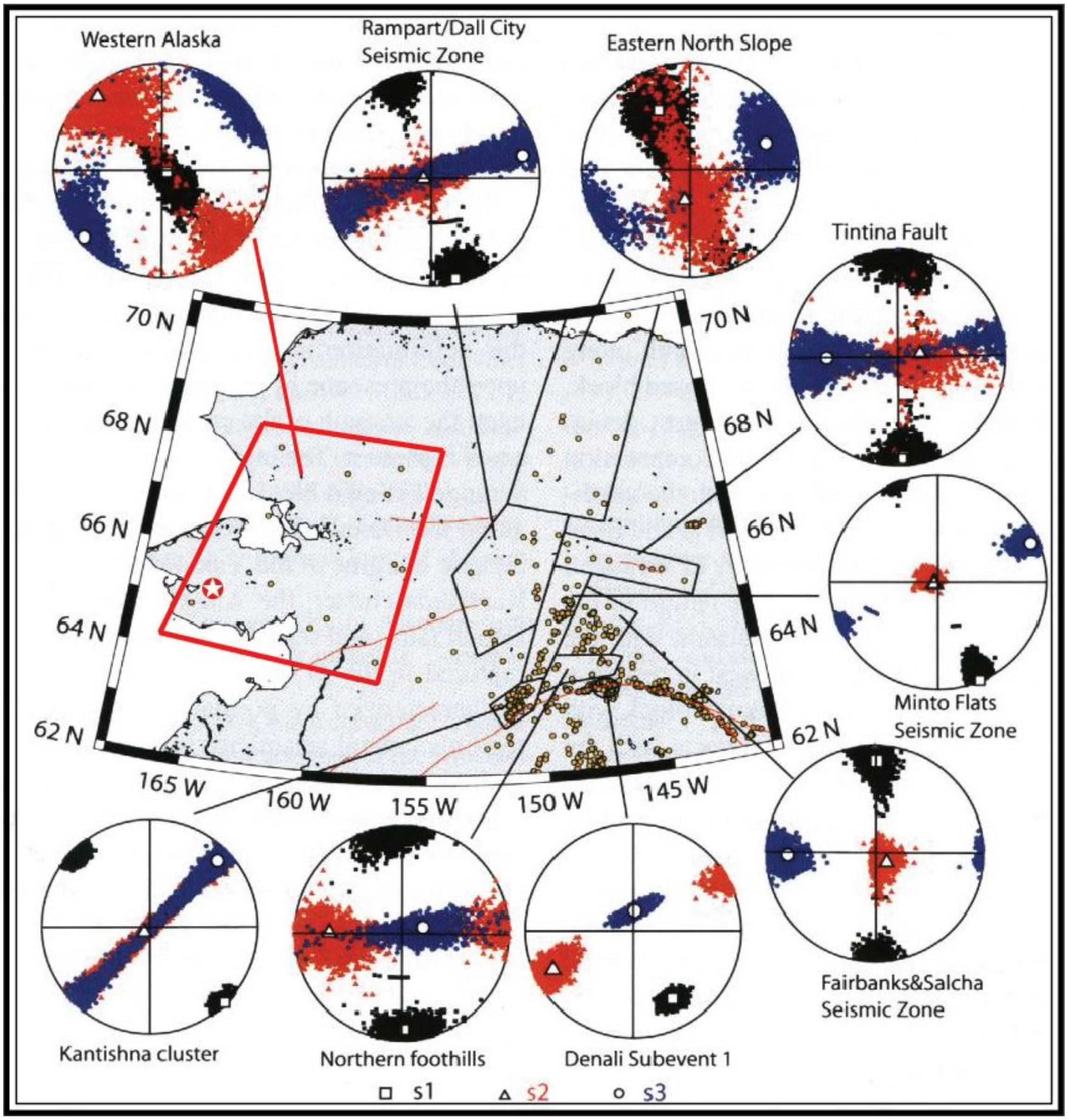

Figure 2.2: Seismicity map of central and western Alaska. Sigma 1, 2, and 3 are shown by color and symbols for the averaged sigma orientation (Ruppert, 2008). The location of Pilgrim Hot Springs is marked by the star.

2.2.3 Surficial and Bedrock Geology of the Pilgrim River Valley

Pilgrim Hot Springs is located in the middle of a graben valley with alluvial-fill derived from the glacially-eroded Kigluaik Mountains immediately to the south (Till et al., 2011; Turner et al., 1979). The surface expression of bedrock is only apparent in the nearby mountains (Figure 2.3). The composition of the basement block underlying the springs is described as Late Proterozoic-Early Paleozoic amphibolite to granulite facies metamorphic rock (Till et al., 2011; Turner et al., 1979). Only a few kilometers to the north lie Marys Mountain and the Hen and Chicken Mountains that are mainly composed of Late Proterozoic metasedimentary and metagranitic units intruded by undifferentiated Cretaceous granite present in both (Till et al., 2011). The older units are the same Late Proterozoic units exposed in the Kigluaik Mountains (Amato and Miller, 1994). The Kigluaik range-front fault at the northern base of the Kigluaik Mountains has an en echelon-style step over along the fault line and was previously mapped as a normal fault in a strongly extensional setting (Ruppert, 2008; Turner and Forbes, 1980). Abrupt truncation at the upper reaches of glacial moraines and outwash gravels approximately along the Kigluaik fault indicates recent movement (Turner and Forbes, 1980). A wide alluvial apron extends a couple of kilometers from the mountains where the Pilgrim River has reworked the valley floor leaving behind a visual trace of past channels and floodplains (Figure 2.3). Throughout the valley, the tundra is underlain by discontinuous permafrost with surface permafrost-related features such as thermokarst lakes, frost-heaves, and pingos (Turner et al., 1979). Pilgrim Hot Springs is located in the middle of the valley containing a variety of vegetation including cottonwood trees, wild flowers, grassy fields, and farmed rhubarb, atypical for a predominantly tundra region. This vegetation aids in delineating the edges of the geothermal anomaly at the site by providing a clear and distinct boundary from forest to tundra. Thawed or absent near-surface permafrost and early snow-melt patterns also distinguish the areas of elevated heat flow and shallow subsurface hydrothermal upflow that feed the hot springs (Daanen et al., 2012; Haselwimmer et al., 2011). The thawed ground feature of the hot springs is only one aspect of the underlying geothermal system. A wide range of data is presented in the next chapter that provides a greater understanding of the nature of the Pilgrim Hot Springs geothermal system.

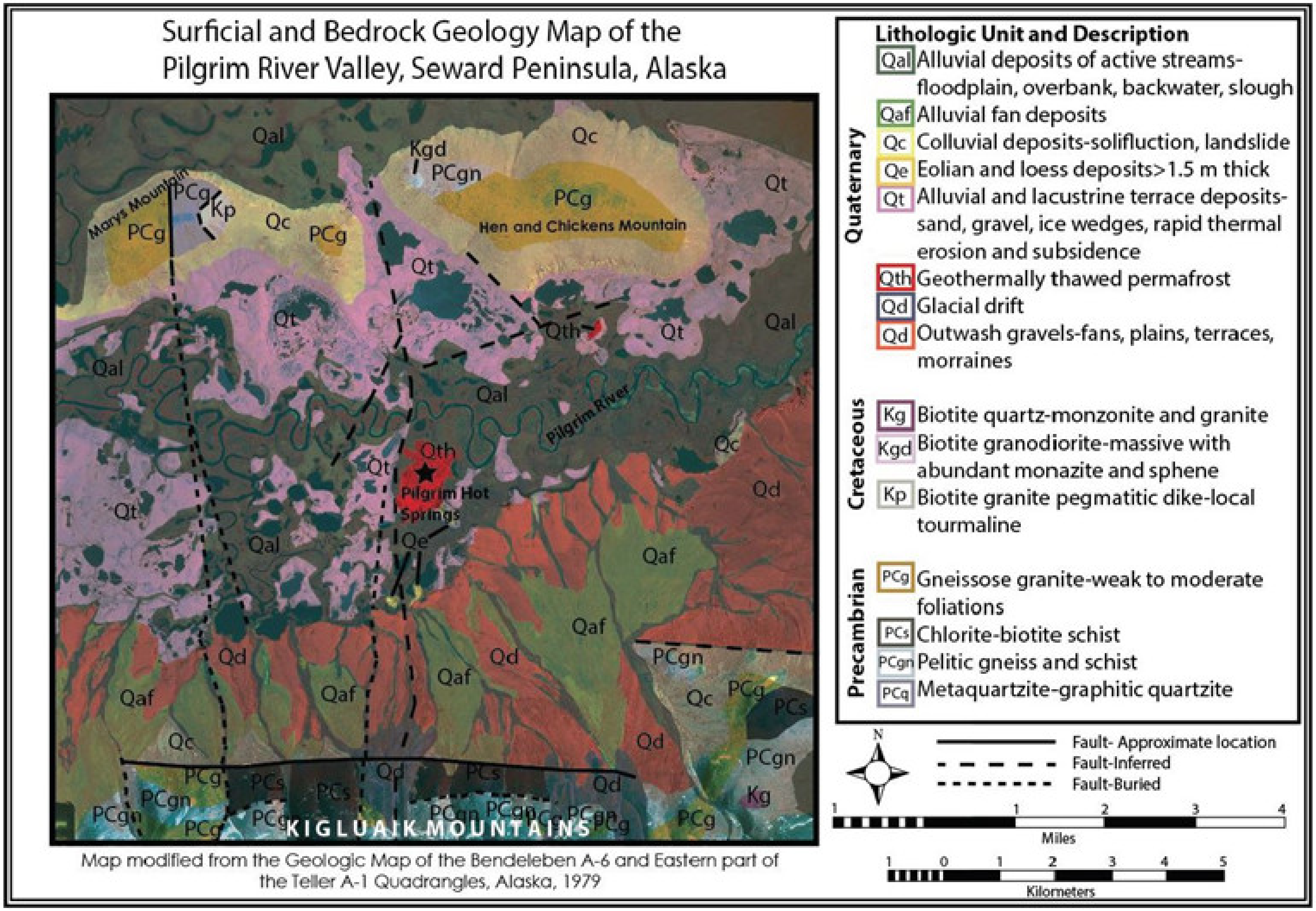

Map modified from the Geologic Map of the Bendeleben A-6 and Eastern part of the Teller A-1 Quadrangles, Alaska, 1979

Figure 2.3: Surficial and bedrock geology map of the Pilgrim River Valley. Modified from Turner et al. (1979).

Chapter 3: Data and Data Products

A range of different data sets were collected and measured at Pilgrim Hot Springs from June to September 2012. The gathered data consist of rock samples, geophysical surveys, well cuttings descriptions, and geophysical and temperature logs. These are used to frame the model by determining the stratigraphic architecture, permeability, and hydrothermal fluid upflow and outflow pathways. Subsequent analysis of sediments was conducted through multiple analytical procedures: reflectance spectroscopy, methylene blue titration, x-ray diffraction, and thin-section characterization of rock samples and drill core. An array of analytical techniques is used to assess the degree of past hydrothermal alteration in the sediments and bedrock.

3.1 Field Data

3.1.1 Rock Sample Collection

Several rock samples were collected to study the range of lithologies exposed in the proximity of Pilgrim Hot Springs (Figure 3.1). The Kigluaik Mountain samples consist of mica schist to phyllite with locally abundant garnets and gneissose granites. Hen and Chicken has similar gneissose granite exposures. A pegmatitic dike outcrop northeast of the hot springs contains quartz, k-spar, fine-grained micas, and abundant, well-developed black tourmaline. A calcareous schist/impure marble adjacent to the pegmatitic dike was also sampled as it is seldom exposed in the immediate basin area.

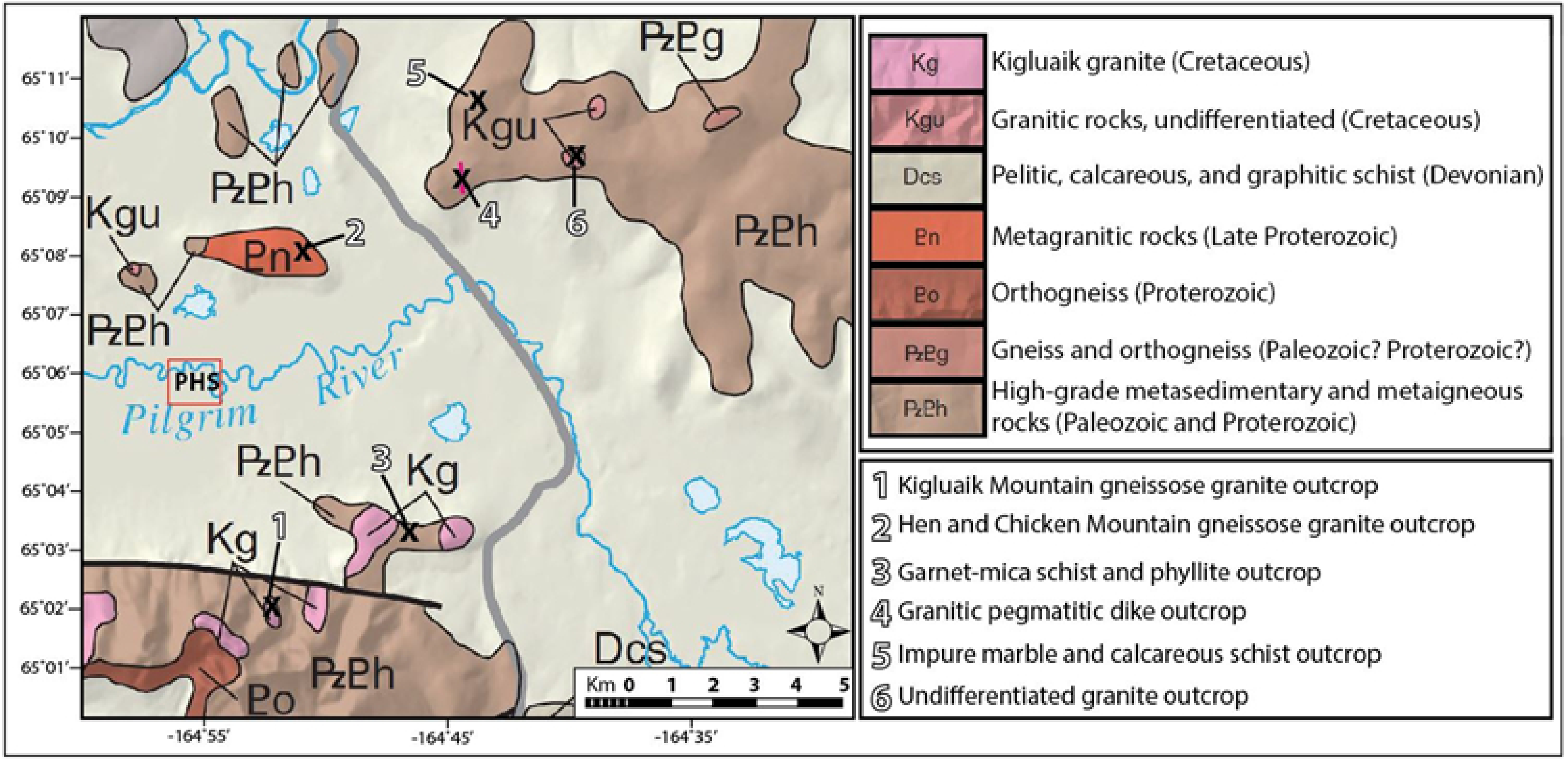

Figure 3.1: Place map of the rock sample collection sites. Outcrops are labeled by numbers and located on the geologic map to the left. Modified from Till et al. (2011).

3.2 Geophysical Data

The geophysical resistivity studies provide detailed information on the different types of sediment, fluid compositions, and conductive structures at depth in the basin. The contrast of resistivity and conductivity is associated with certain geologic materials (Figure 3.2) (Palacky, 1988). Unconsolidated glacial sediments, the most common sediment type in the basin, show a low resistivity value of ~10 ohm-m for clays and trending higher for gravels and sand. Saline fluids yield a very low resistivity (high conductivity) at <1 ohm-m and fresher fluids have a higher resistivity at >1-100 ohm-m. This is an important distinction where the resistivity surveys show areas of low resistivity associated with outflow of geothermal fluids with more dissolved constituents. At Pilgrim, the low resistivity of the hot springs are in marked contrast to a highly resistive boundary of permafrost at 1,000-100,000 ohm-m which conveniently isolates the extent of the geothermal system near the surface.

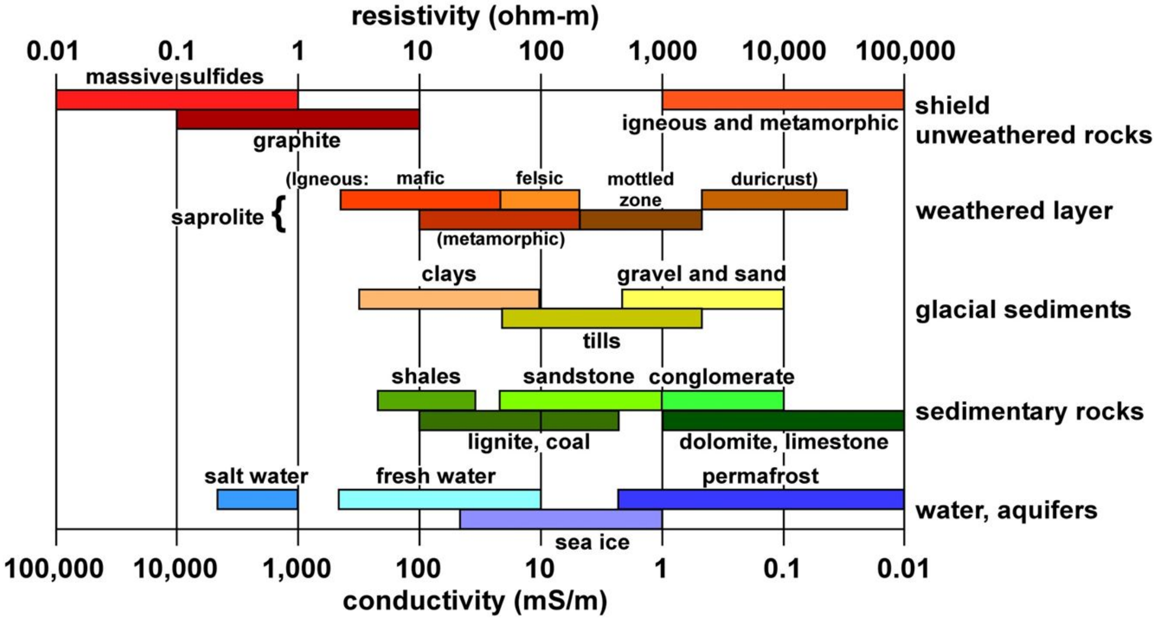

Figure 3.2: Logarithmic scale of resistivity values for geologic materials. Resistivity (ohm-m) and conductivity (mS/m) values are plotted for a range of sediments, rock types, and fluid compositions (Palacky, 1988).

3.2.1 USGS Aeromagnetic and Electromagnetic (EM) Survey

An aeromagnetic and electromagnetic survey was conducted over Pilgrim Hot Springs by FUGRO with funding support from the USGS and the Alaska Center for Energy and Power in the spring of 2011 (McPhee and Glen, 2012). The survey was conducted with a FUGRO-Resolve system flown by helicopter with a frequency range between 400 Hz and 140 kHz. A Cesium vapor magnetometer was used with a sample rate of 10 Hz and sensitivity of 0.01 nT. This survey includes diurnal corrections, differential GPS positions, 0.2-0.4 km spacing, and was acquired by helicopter at 60 m altitude. The helicopter towed a large induction coil that generated a magnetic field and measured the changes in resistivity from the ground below. Processing of the data was completed by the USGS and described in more detail in the Pilgrim Hot Springs Phase 1 Report (University of Alaska, 2012).

A differential resistivity map at 20 m depth produced by the USGS electromagnetic resistivity survey is provided below in Figure 3.4. The survey area spans the Pilgrim River valley between the Kigluaik Mountains and the hills to the north. Pilgrim Hot Springs is located in the center of the map that shows a low resistivity anomaly emanating from the site and extending north-northeast. Highly resistive zones correlate to more commonly resistive materials such as the exposed igneous and metamorphic bedrock as well as the discontinuous permafrost. The more conductive/low resistive zones outside of the hot springs site could be the result of conductive clay formation through diagenetic processes independent of the geothermal system or conductive structures at depth connected to geothermal fluid outflow.

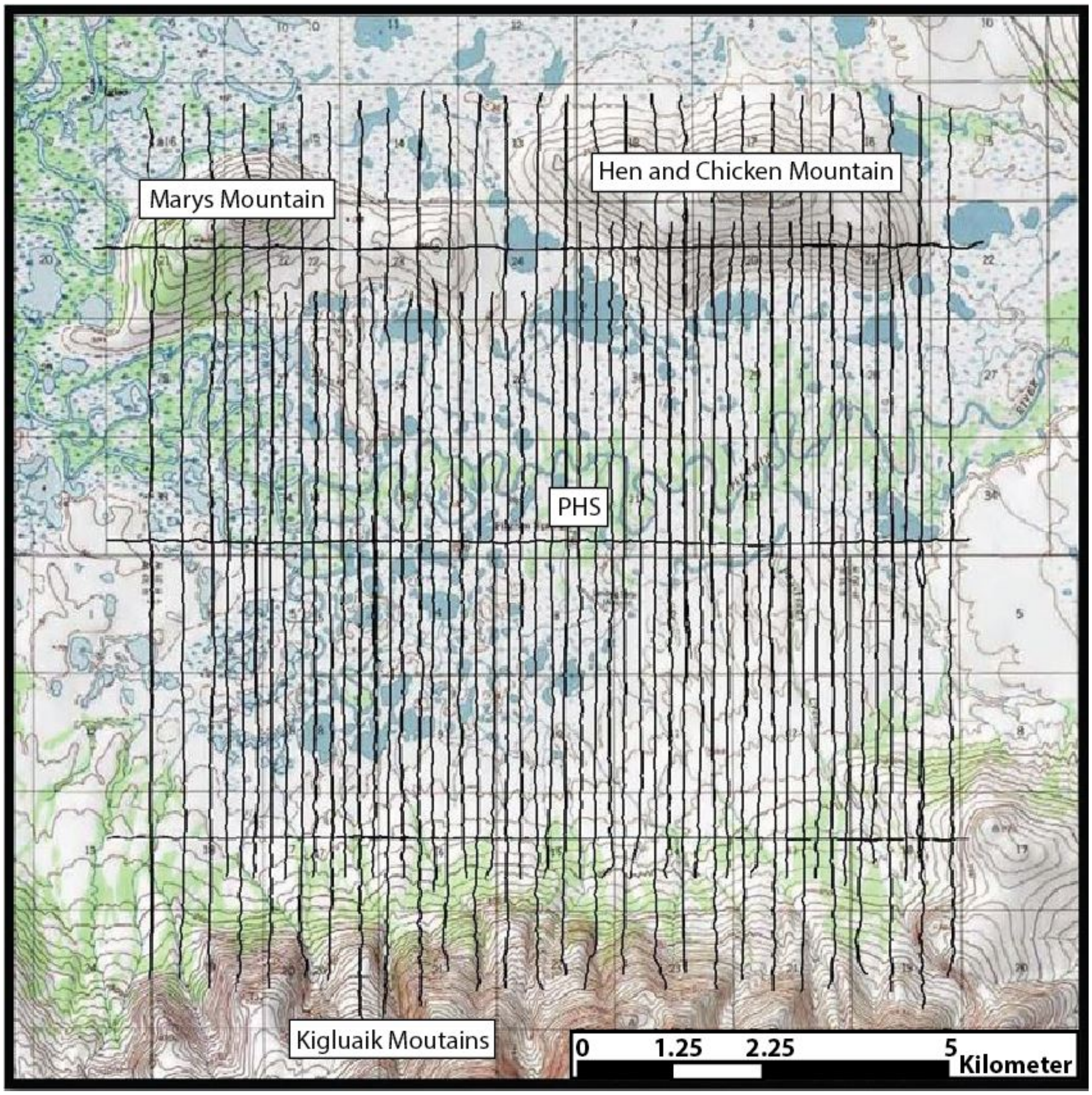

Figure 3.3: Flight path for aeromagnetic and electromagnetic survey (McPhee and Glen, 2012).

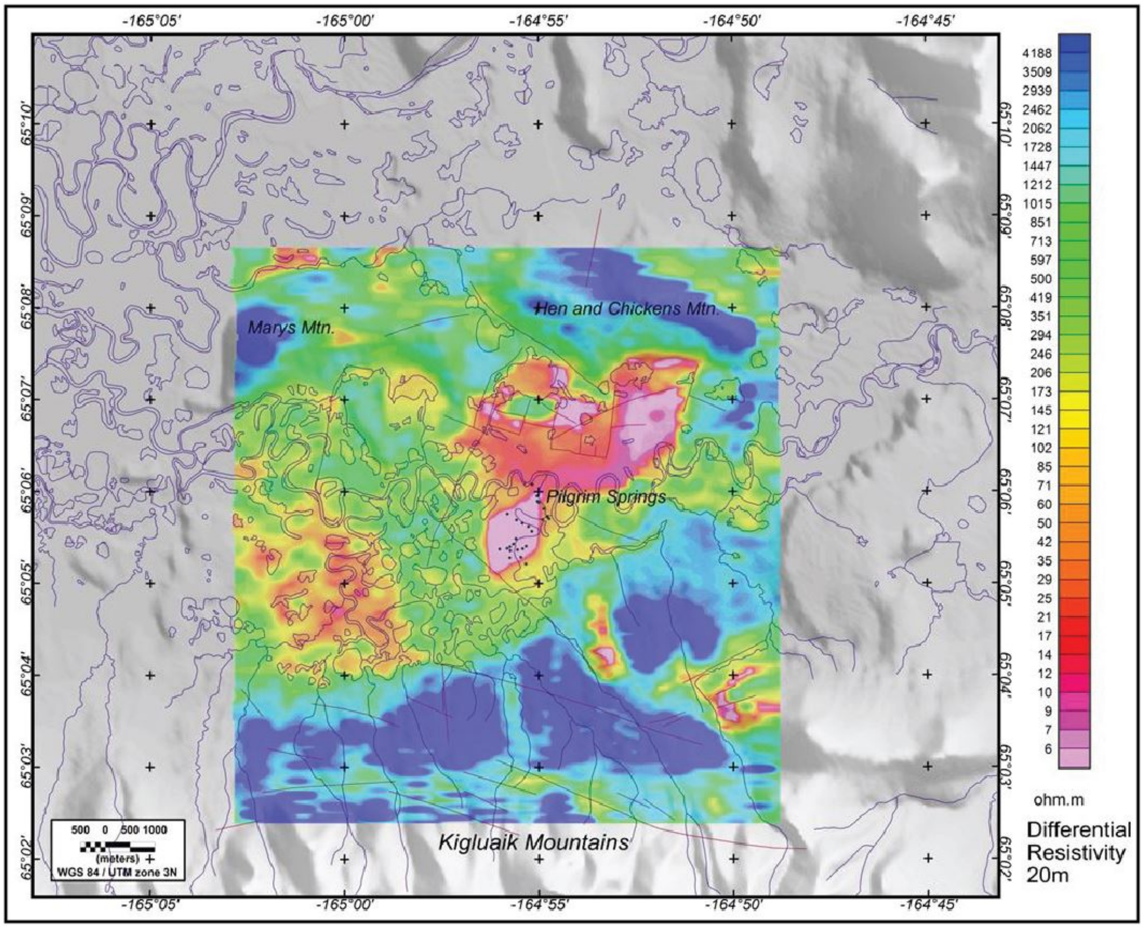

Figure 3.4: Differential resistivity map at 20 m depth. Produced by the USGS airborne electromagnetic resistivity survey (McPhee and Glen, 2012).

3.2.2 Magnetotelluric (MT) Resistivity Survey

The locations of the MT stations at Pilgrim Hot Springs were determined by maximum spacing for best resolution and constrained by accessibility. In total, 59 stations recorded at 0.001-10000 Hz range overnight with an average distance of 100 m apart with a remote station 5 km SE from the site (Figure 3.5). Data processing and recording equipment was provided by FUGRO Electric Magnetics Italy Srl. MT evaluation of the site provides insight into the changes in resistivity (decreasing resistivity is casually referred to as increasing conductivity in this discussion) to elucidate the geologic caps and plumbing of the reservoir. MT is a deeply focused electromagnetic method that measures the wide -range of surface recordings of natural fluctuations in the earth's magnetic and electric fields. This is recorded for both period and location beneath 24-hour recording stations emitting an induced current at different orders of magnitude (FUGRO, 2012). The relationship between the electric and magnetic field variations produces an impedance tensor that normalizes the observed electric resistivity in order to determine the distribution of resistivity at depth (Heise et al., 2007).

MT resistivity survey data highlights the spatial extent of the geothermal system. The dynamics of high conductivity, or inversely low resistivity, in outflowing and upflowing geothermal fluids, proximity to the heat source, and stratigraphic architecture of the hydrothermally altered swelling clays can be inferred from MT data (Cumming, 2009). Three 1D smoothed inversion profiles down to 1000 m that show resistivity variations with depth are present (Figures 3.6-3.8). A lack of station coverage over a section of the profile results in poor or no resolution at depth as apparent in the profile lines as bank spaces. Figure 3.5 is a location map of the station coverage with the profile lines plotted. MT Profile D (Figure 3.6) shows a large, very low resistivity pattern (<1 ohm-m) from 150 m to 400 m that extends into the top of the basement at 320 m and is sharply bounded by increasingly resistive zones on the west (left) and east (right). A very thin, flat-lying conductive zone near the subsurface is also apparent in the profile. Areas of high resistivity values are interpreted as permafrost (0-100 m) and cold regional groundwater influx. The same low resistivity body is seen in Profile C (Figure 3.7) in the vicinity of PS-12-2 where it intersects the sharp highly resistive boundary to the southeast. Profile 2 (Figure 3.8) shows the low resistivity body dissipating to the northeast where it becomes less distinct. Well S-1, a relatively cold well, appears to have been drilled into the more resistive zone.

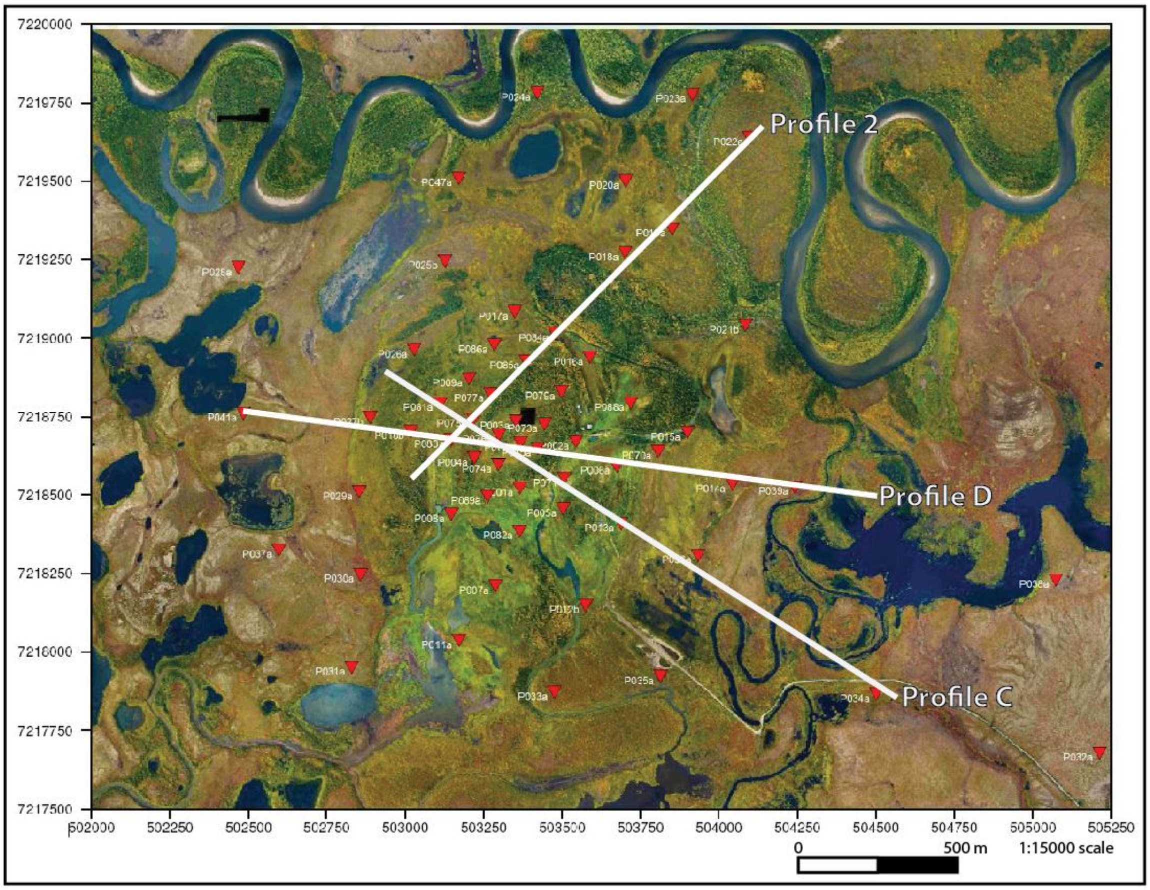

Figure 3.5: Locations of magnetotelluric resistivity recording stations (FUGRO, 2012).

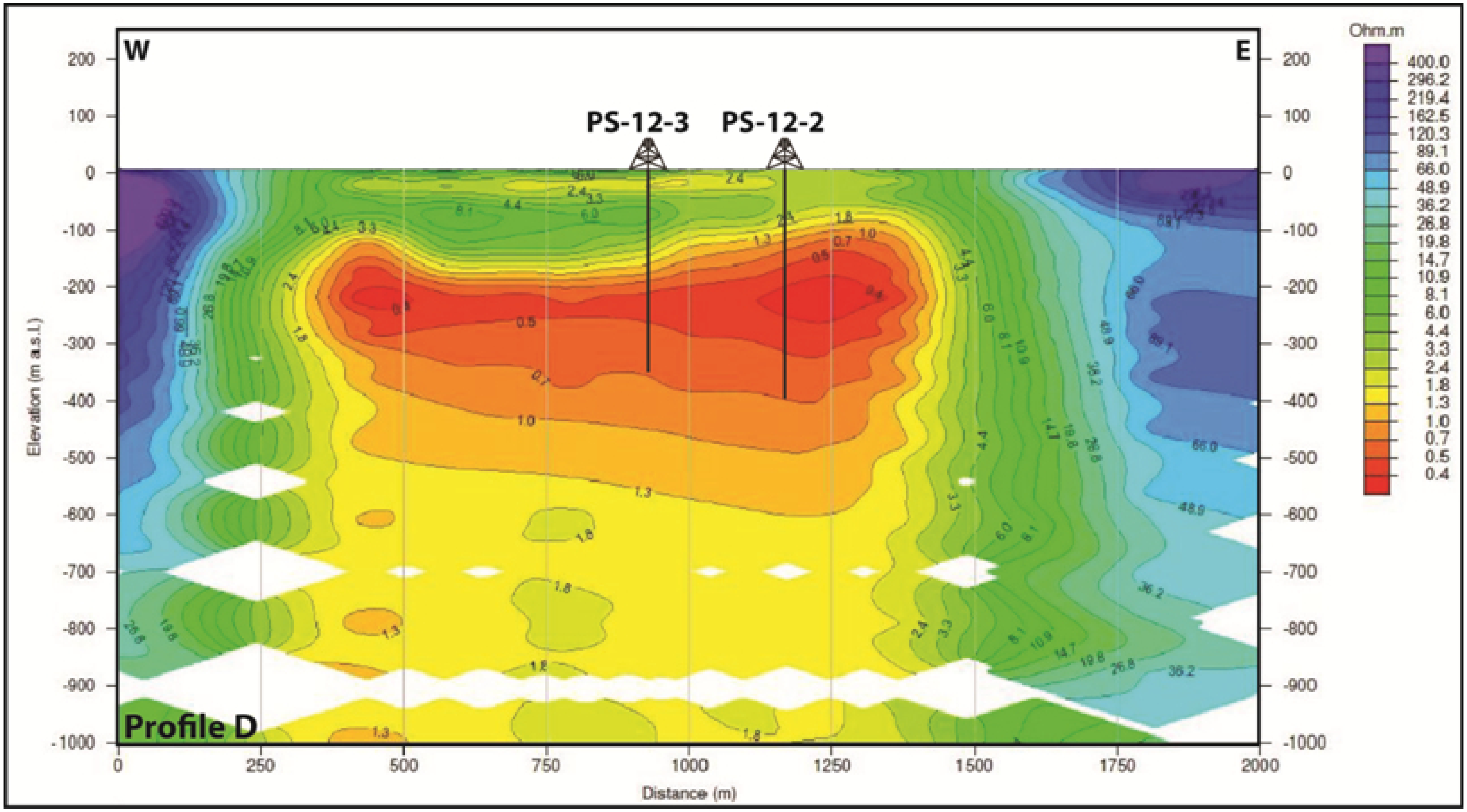

Figure 3.6: Magnetotelluric resistivity profile line D. Cross-section line is from the smoothed 1D MT inversion (FUGRO, 2012). The line is oriented west to east.

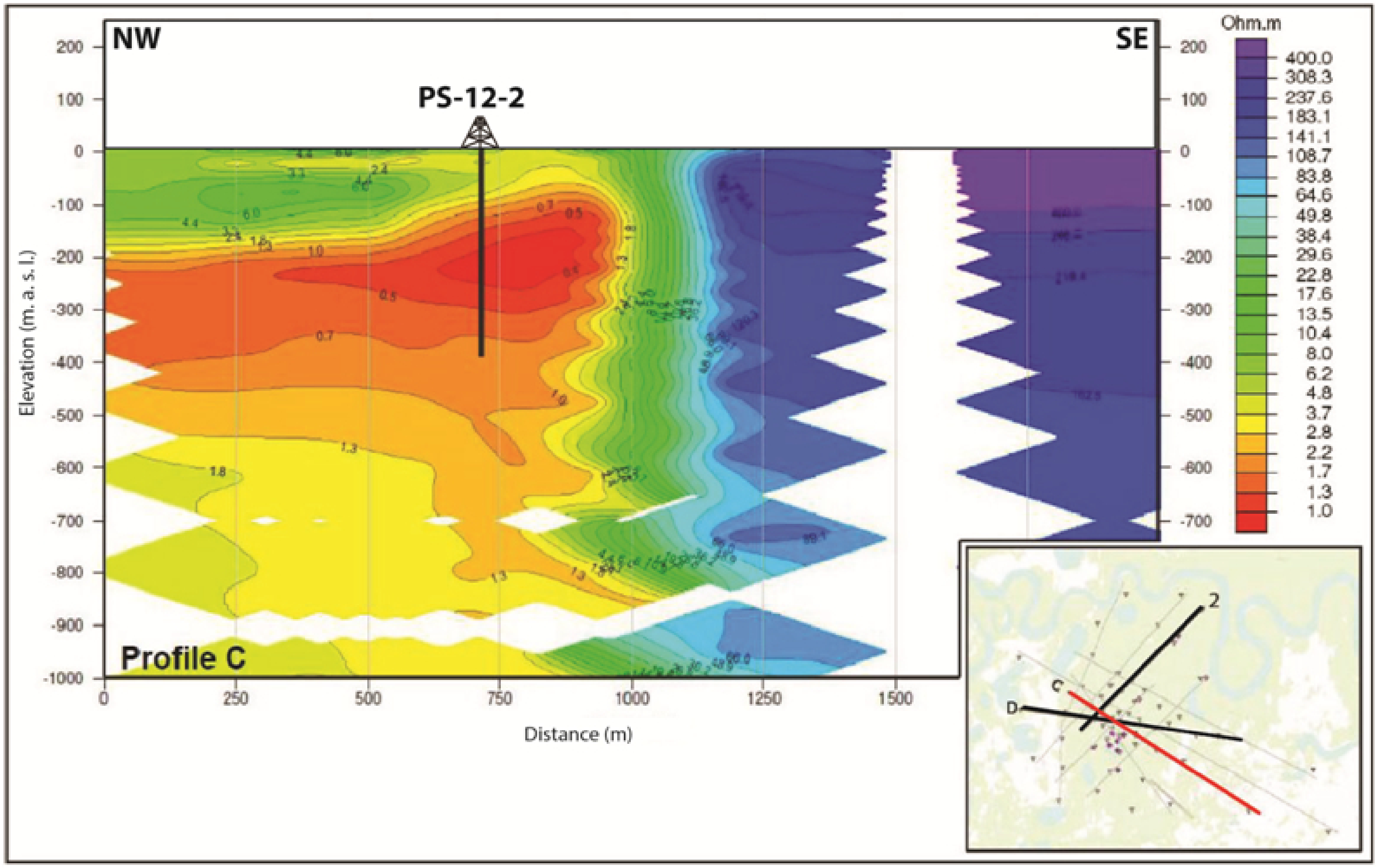

Figure 3.7: Magnetotelluric resistivity profile line C. Cross-section line is from the smoothed 1D MT inversion (FUGRO, 2012). The line is oriented northwest to southeast.

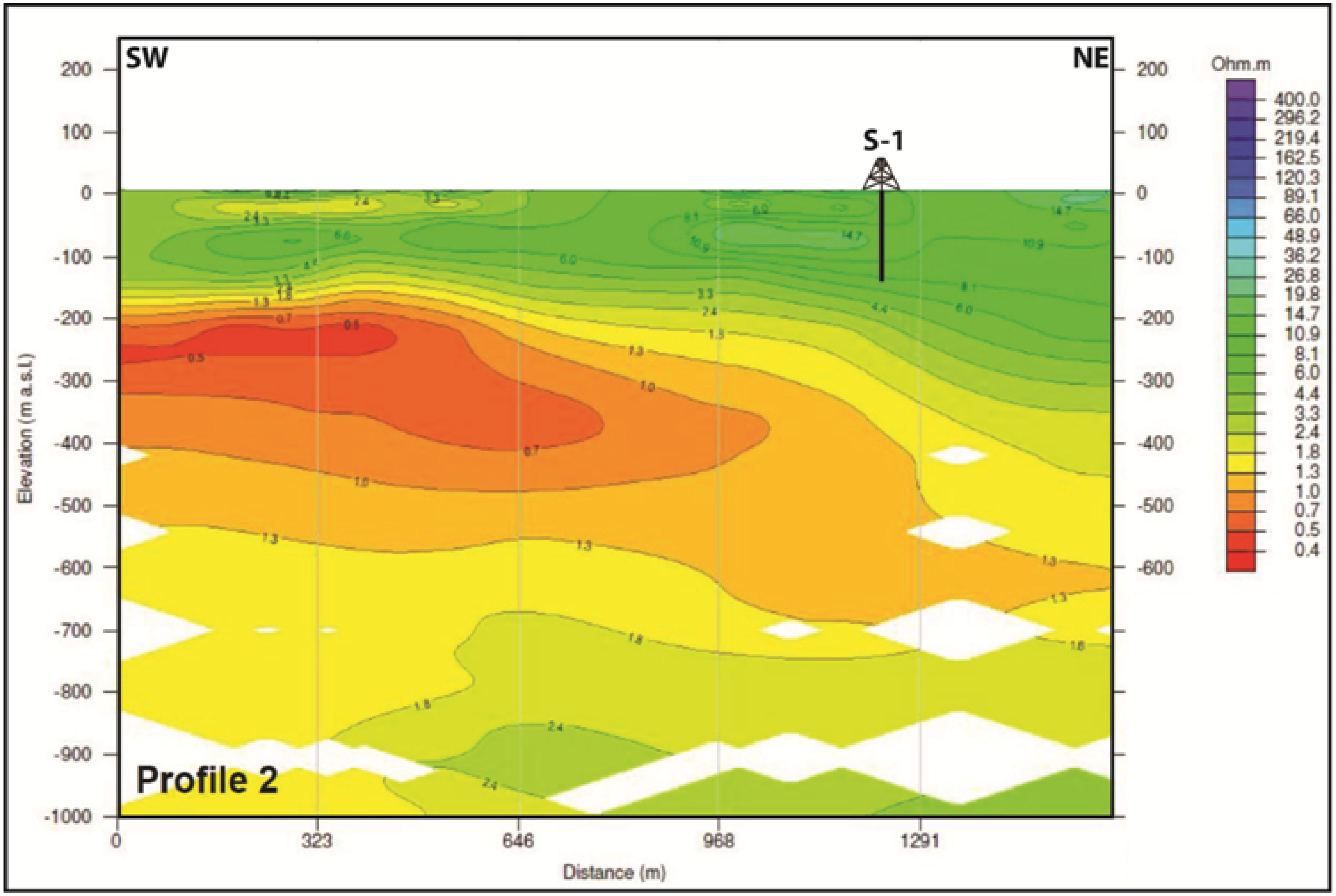

Figure 3.8: Magnetotelluric resistivity profile line 2. Cross-section line is from the smoothed 1D MT inversion (FUGRO, 2012). The line is oriented southwest to northeast.

3.2.3 Ground-based Gravity Survey

A ground-based isostatic gravity survey was conducted by the USGS Menlo Park team headed by Jonathan Glen in spring of 2010. Two teams ran several profile lines across the Pilgrim River valley. Each gravity meter station base was placed at a known elevation along the profile line. The field gravity readings were normalized to several base station gravity meters located at the site, the nearby camp, in the Nome Post Office and airport, as well as in Anchorage at the University of Alaska Anchorage and airport. By normalizing to gravity stations at known elevation points, topography can be extracted from the gravity meter readings and produce a map of changing elevation and basin depth.

Figure 3.9 shows the gravity survey lines and station locations with initial gravity readings. In general, the figure shows the shallow bedrock surface depth under much of the alluvial fan and glacial outwash deposits along the base of the Kigluaik Mountains and to the east and north of the hot springs. The blue color indicates the deeper basin appears to terminate beneath the hot springs and deepen to the southwest (Figure 3.10).

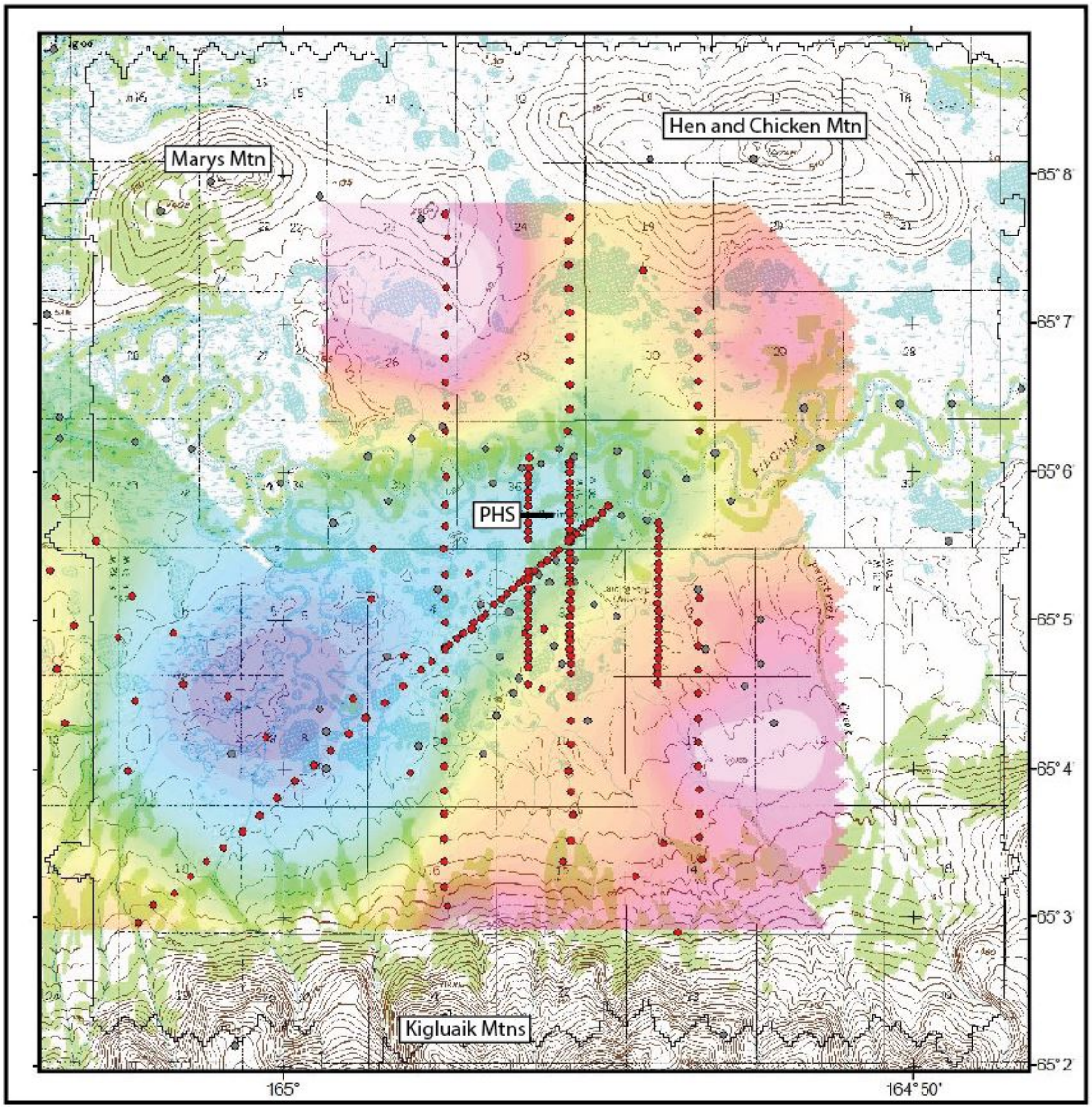

Figure 3.9: Isostatic gravity survey station location map. Map provided by Jonathan Glen. Warmer colors (orange and red) indicate above sea level, green equates to sea level, and cooler colors (blue and violet) are below sea level. In this case, light blue (immediately below Pilgrim) correlates to a basin depth to basement at 320 m (corroborated with drilling contact). The deeper basin indicated by the dark blue and violet colors, is estimated to be twice as deep as below Pilgrim to ~700 m depth (Jonathan Glen, personal communication).

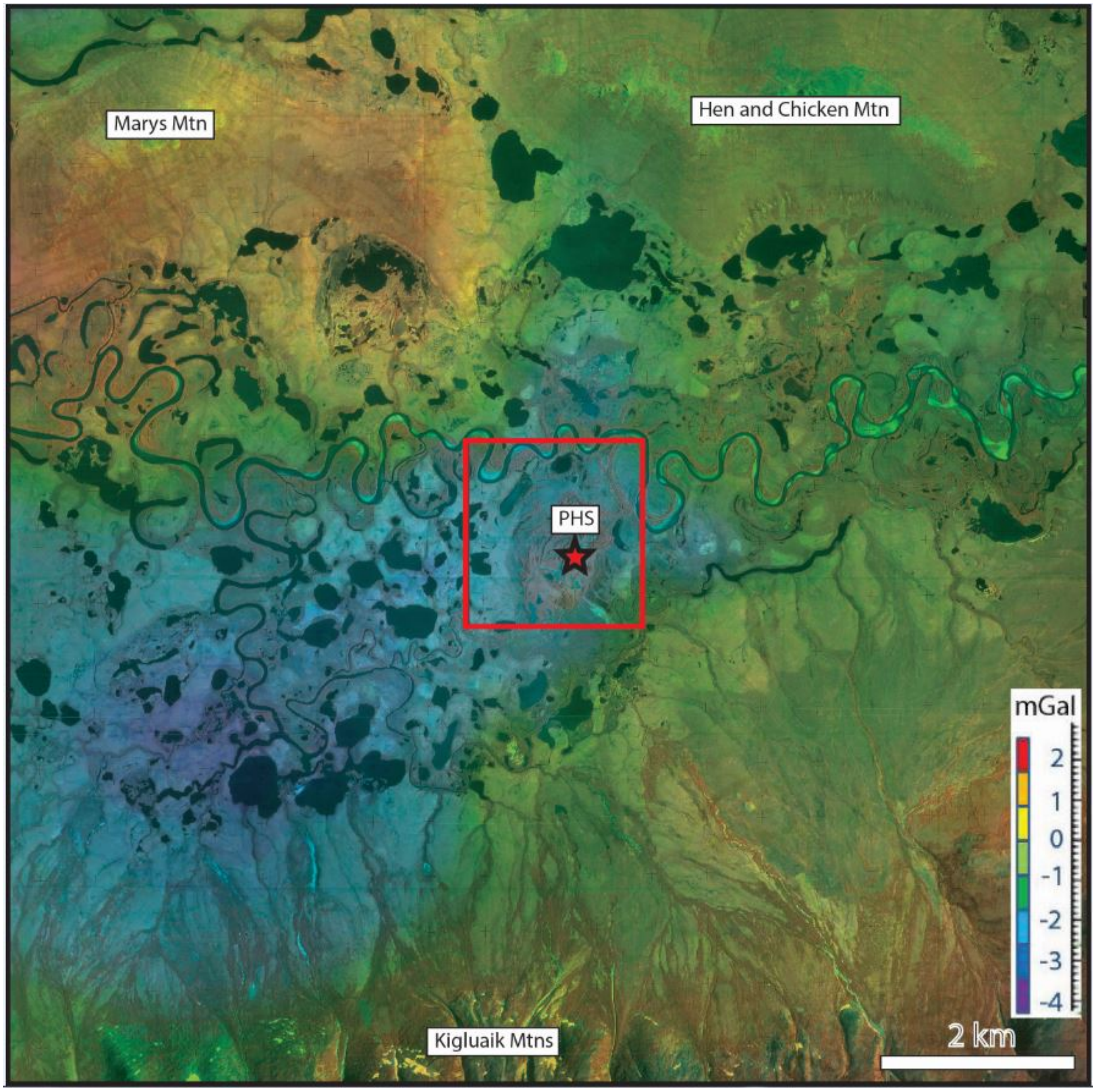

Figure 3.10: Isostatic gravity anomaly map of the Pilgrim River Valley. Overlaid by an Alaska High-Altitude Photography (AHAP) image of the Pilgrim River valley. Isostatic gravity anomaly map provided by Jonathan Glen, USGS Menlo Park. The red box around Pilgrim Hot Springs marks the edge of the conceptual model boundaries that encompasses the extent of the observed thermal anomaly at the surface.

3.3 Geoprobe Data

The Geoprobe, operated by the USGS Central Region Research Drilling Team and the Alaska Center for Energy and Power, is a small drilling track vehicle that uses the direct push method of hammering pipe to shallow depths via a small hydraulic system. This unit was used to conduct a shallow temperature survey with 64 holes of 10-60 m depths that covered the hot springs site as well as several holes in the surrounding tundra, some intercepting permafrost (Figure 3.11). The Geoprobe holes outside of the thermal expression provide a background temperature gradient that is not enhanced by the heat flux of the geothermal system. This wealth of data provides extensive coverage of temperature variations at the surface and in the shallow reservoir that complements the data obtained from the deeper drilling.

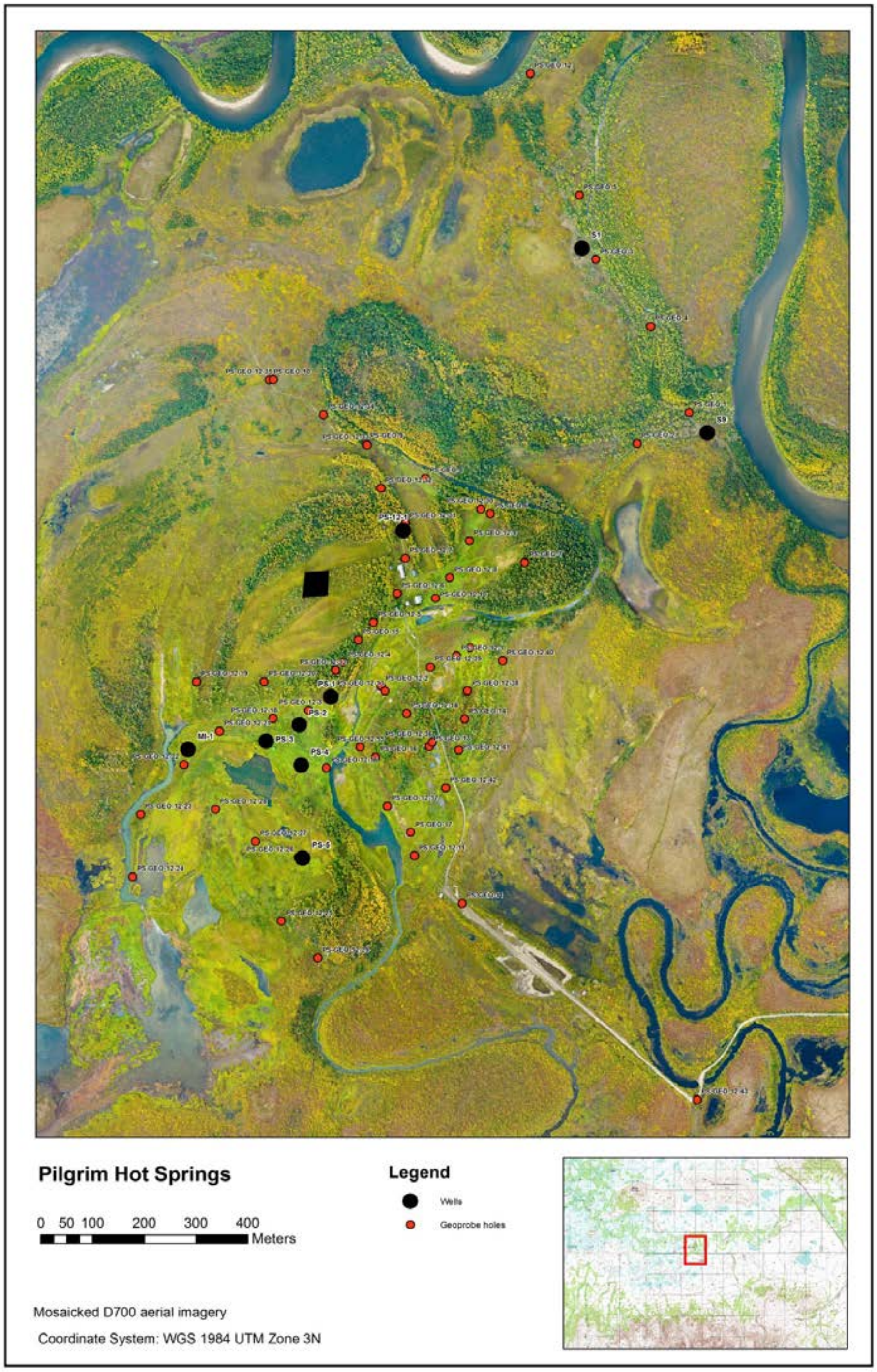

Figure 3.11: Well and Geoprobe hole location map. All Geoprobe holes drilled on site (red dots) with several of the deeper wells plotted (black dots). Image credits, Christian Haselwimmer.

3.4 Drilling Data

3.4.1 Sediment Characterization

Sediments obtained through sieve tables from reverse circulating mud while drilling were described and characterized to quantify the porosity and permeability of the sampled depth intervals. The descriptions of the sediments include grain size, shape, sorting, and mineralogy. These are critical input parameters for defining the lithostratigraphy of each drilling interval, making the construction of lithologic well logs and stratigraphic correlations possible. Also derived from this data is the calculation of the porosity and permeability of the sediments.

The permeability of a porous medium, k, is its natural ability to transmit fluids through interconnected pores. The unit of measurement for permeability, defined as m^2, is Darcy ($D=9.86923*10^{-23}$ m^2) (Bundschuh and Suarez Arriaga, 2010; Fitts, 2005). Permeability can be divided into four distinct types: permeability related to the intergranular spaces of the porous medium, micropermeability associated with interconnected microfractures, permeability related to nets of fractures, and macropermeability of open faults (Bundschuh and Suarez Arriaga, 2010; Fitts, 2005). The volume of intergranular space in the sediments is the focus of this assessment. Permeability also accounts for the fluid dynamic viscosity and pressure gradient of the aquifer (Bundschuh and Suarez Arriaga, 2010). However, without these fluid parameters, the intrinsic permeability can be estimated from sediment measurements.

To properly quantify intrinsic permeability, the sediment grain diameter, distribution, and porosity are calculated. Grain diameters of the clay to gravel-sized sediments are measured by grain size card. The distribution of the grain diameters for every given sample interval (~3 m of drilling depth) are also recorded through visual determination. For every sampled interval, a percent is given for clays through gravel adding to 100%. This allows for an average grain diameter to be estimated for that interval by multiplying the percent of each grain diameter by the representative diameter and summing the results for an average diameter for the interval. Porosity values are obtained from the table of average porosity values for unconsolidated sediments (Table 3.1). Beard and Weyl (1973) obtained porosities of the range of poorly to well-sorted sediments. The average porosity of each sorting parameter is multiplied by the average grain diameter for intrinsic permeability (Shepherd, 1989).

Bear (1972) showed distributions of various sediment types by plotting particle diameter versus percent clay finer by weight (Figure 3.12). Percent finer by weight plots the distribution of coarse to fine grains in a given mix of sediments by percent. Gravelly sand to common clay minerals (montmorillonite and kaolinite) also appear in the examined sediments of Pilgrim Hot Springs (Table 3.2). The particle diameters of the range of sediment types for the Pilgrim samples match closely to the diameters reported by Bear (1972) (Figure 3.12).

Table 3.1: Average porosity values for sediment size and sorting. Average porosity values are for very well to very poorly sorted, coarse to fine sands. The shaded section represents the values used in the intrinsic permeability calculations for the Pilgrim Hot Springs drill cuttings. Modified from Beard and Weyl (1973).

Size	**Coarse**		**Medium**		**Fine**		**Very Fine**		**AVG Porosity**	**Std. Dev. (%)**
Sorting	Upper	Lower	Upper	Lower	Upper	Lower	Upper	Lower		
V. Well	40.8	41.5	40.2	40.2	39.8	40.8	41.2	41.8	40.8	0.6
Well	38	38.4	38.1	38.8	39.1	39.7	40.2	39.8	39	0.8
Moderate	32.4	33.3	34.2	34.9	33.9	34.3	35.6	33.1	34	1
Poor	27.1	29.8	31.5	31.3	30.4	31	30.5	34.2	30.7	1.8
V. Poor	28.6	25.2	25.8	23.4	28.5	29	30.1	32.6	27.9	2.8
AVG Porosity	35	35.2	35.3	35	35.5	36.4	36.7	37.4		
Std. Dev. (%)	6	6.3	5.5	6.2	4.9	5.3	5	4.2		

Table 3.2: Grain diameter and intrinsic permeability by sediment type. Representative grain diameters (d) in mm and intrinsic permeability (mm^2) for sampled intervals in wells PS-12-1, PS-12-2, and PS-12-3. The samples are organized with gravel as the highest permeability to clay with the lowest. Listed representative diameters are the commonly accepted diameters of these sediment types.

Sediment Type	Diameter (mm)	Intrinsic Permeability (mm^2)
Gravel	2	2E+00
Very Coarse Sand	1.2	6E-01
Coarse Sand	0.6	1E-01
Medium Sand	0.3	4E-02
Fine Sand	0.08	3E-03
Silt	0.03	4E-04
Clay	0.002	2E-06
Indurated Sand	0.1	4E-03

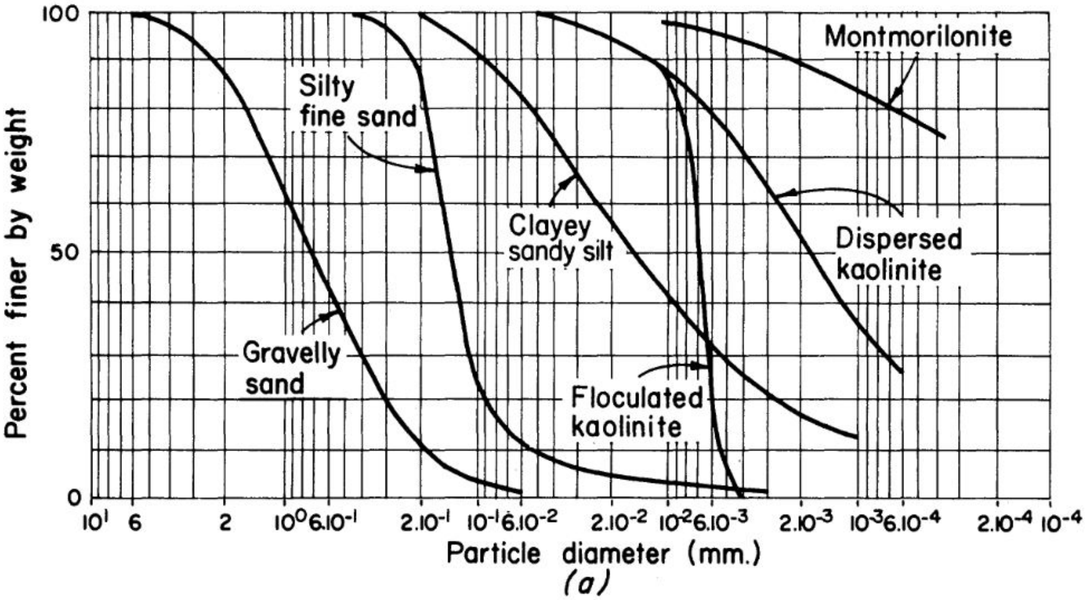

Figure 3.12: Logarithmic chart of particle diameter by sediment type. Figure from Bear (1972).

3.4.2 Geophysical Well Logs

The USGS Central Region Research Drilling Team ran geophysical logs for the Pilgrim Hot Springs wells consisting of gamma ray, conductivity, and resistivity. The equipment used to run the tools consisted of a computer-controlled winch system that lowered the tools downhole at a constant speed with real time depth readings. Gamma ray is the most valuable log as it allows for real time lithology prediction at the well site and can be run in cased holes, thus avoiding downhole logging issues with swelling clays. Conductivity and resistivity logs were only run for PS-12-1 and PS-12-2 due to the demanding drilling schedule and drilling issues in PS-12-3. Gamma ray logs are provided next to the lithologic logs for direct comparison (Figure 3.13).

Lithology and gamma ray logs for several wells are correlated by depth with equidistant spacing (Figure 3.13). The construction of the lithologic logs is guided by correlations of similar gamma ray peaks. Sticking issues with logging PS-5, PS-12-3, and PS-12-1 prevented more complete well log profiles to total depth. Gamma ray counts are highest and most definitive in clay at 175-300 API. Low counts from 0-100 API are observed for the gravels and mixed sands. Indurated zones are typically within 100-200 API. The thick clay interval at 180-260 m depth occurs in PS-12-1, PS-12-2, and PS-12-3.

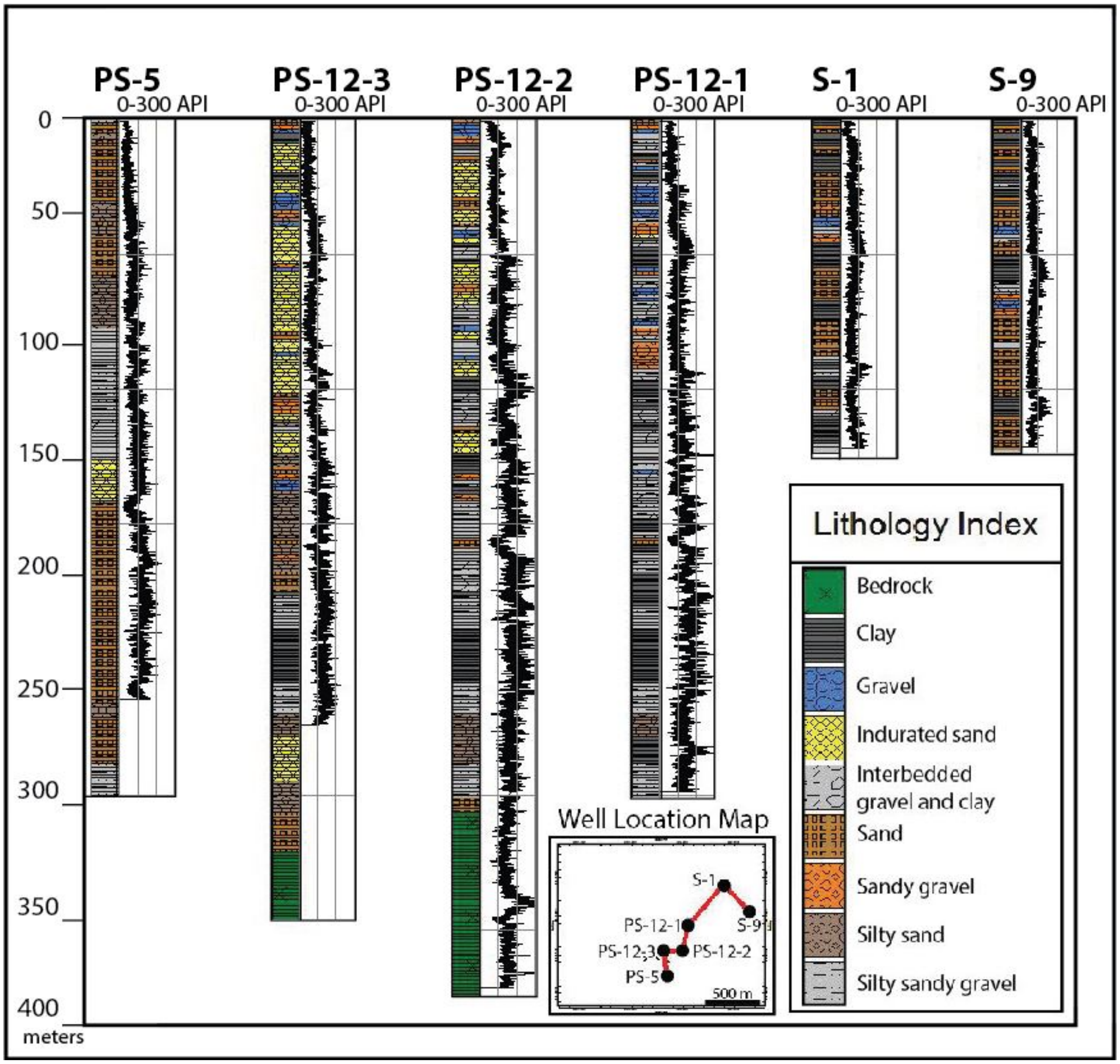

Figure 3.13: Lithologic and gamma ray logs for selected wells.

3.4.3 Static Temperature Logs

Well temperatures were recorded using a Kuster Strain temperature probe. A continuous logging technique of recording temperatures every 3 m per minute allowed the probe to measure the equilibrated ambient temperature in the well at detailed intervals. This approach was typically run at least a week after drilling ceased and the well was cased to allow for equilibration. Temperature curves for several wells on site show a spike in temperature up to 91 °C at 25-50 m and subsequent reversal at 30-100 m (Figure 3.14). All wells show an increasing temperature gradient below the reversal. The shallow temperatures are highest in wells PS-12-2 and PS-12-3 which also have the highest bottom hole temperatures of 91 °C and 80 °C, respectively. The influx of groundwater is estimated to have a flow rate of ~200 gpm flowing through the system from the south to the north, eventually feeding into the Pilgrim River (Lofgren, 1983). It should be noted that the curve for PS-4 is not reliable below 140 m and the multiple fluctuations in PS-5's curve are equipment-related. These measurements were recorded during earlier exploration in the 1980's (Woodward-Clyde, 1983). The shallow peak in temperature is the result of the outflow of geothermal fluids and the increasing temperature gradient is due to the heating of the deeper geothermal reservoir. Wells S-1 and S-9 seem to have only residual outflow fluids and a higher degree of mixing with meteoric groundwater water. These wells also have low temperatures compared to the other wells at the corresponding depth of peak outflow temperatures. The reversal from 30-100 m is attributed to a large degree of mixing with this colder meteoric water where permeability is sufficiently high (Daanen et al., 2012; Woodward-Clyde, 1983).

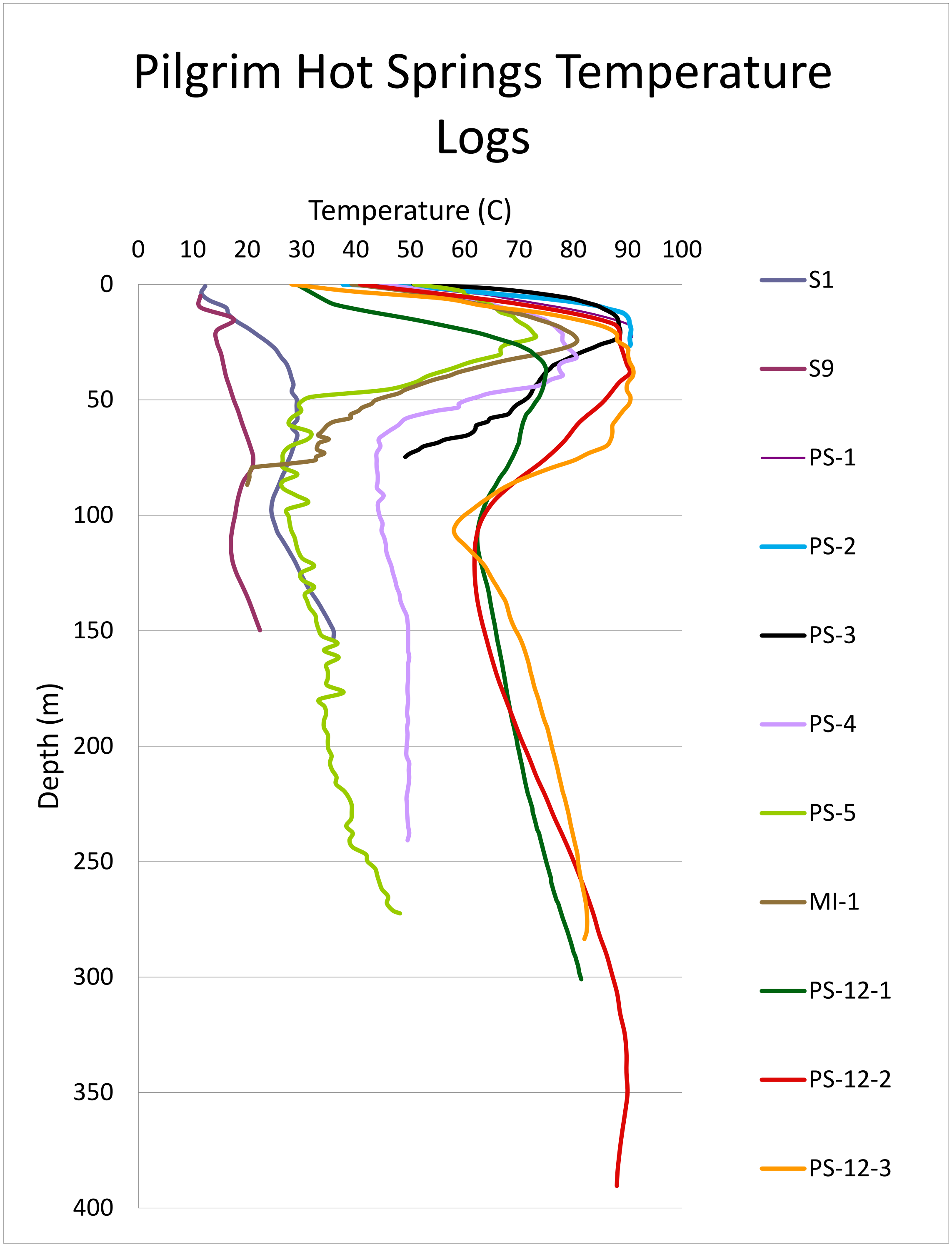

Figure 3.14: Temperature curves for all Pilgrim Hot Springs wells. Measured in Celsius from 0-400 m depths.

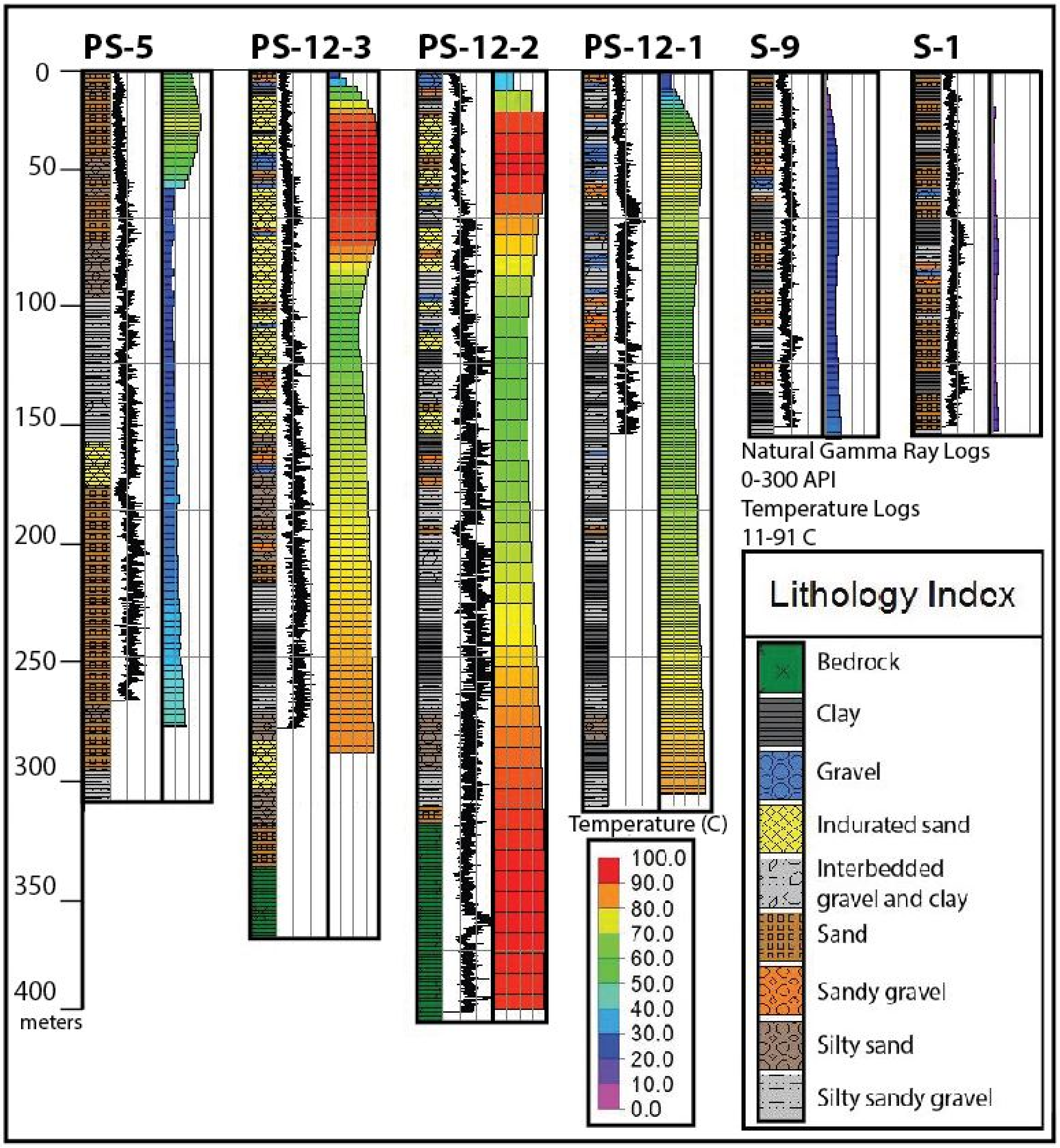

Figure 3.15: Lithology, gamma ray, and temperature curves for selected wells.

3.5 Sample Analytical Techniques

3.5.1 Reflectance Spectroscopy

Visible near infrared to shortwave infrared (VNIR-SWIR) reflectance spectra were acquired over the 400-2500 nm wavelength region with an Analytical Spectral Devices (ASD) FieldSpec Pro and a high-intensity contact probe using a white Spectralon panel as reference. Each sample was measured by holding the probe perpendicular to a preferentially flat or smooth surface to minimize measurement errors associated with stray light. Reflectance spectra were recorded every seven centimeters to detect detailed variations in the mineral spectral absorption features with depth. In the VNIR-SWIR wavelength region, hydroxyl, hydrate, and carbonate anions as well as transition elements (dominantly iron) produce distinctive absorption features (Hunt, 1977). These spectral features can be used to investigate mineral assemblages or variations in specific mineral chemistry that may be related to changing alteration conditions. For example, the depths and wavelength positions of absorption features, such as those related to AlOH and FeOH compounds, can be utilized as proxies for the extent and magnitude of hydrothermal alteration (Calvin et al., 2010; Haest et al., 2012; Harraden et al., 2013; van Ruitenbeek et al., 2005) (Figure 3.17). Geochemical signatures of hot fluids are recorded in subsequent alteration minerals where the fluids emanate from a deeper source. Reflectance spectroscopy is cost-effective and can accommodate large numbers of samples in a relatively short amount of time compared to XRD or XRF (Calvin et al., 2010).

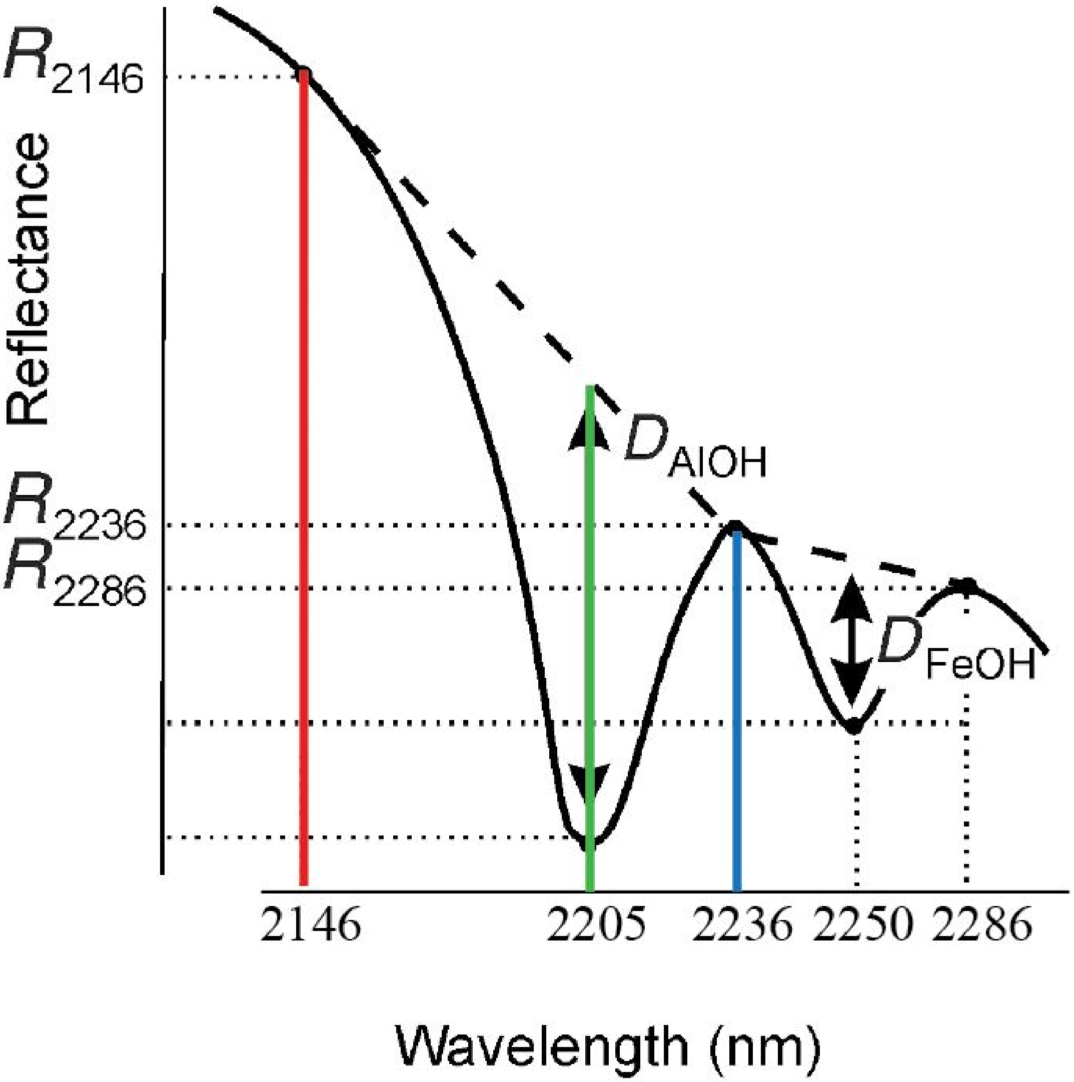

Figure 3.16: AlOH and FeOH absorption features. Red, green, and blue bands define the AlOH absorption feature. Modified from van Ruitenbeek et al. (2005).

Pre-processing of the acquired spectra involved calibrating the data to absolute reflectance using a reflectance spectrum of the Spectralon white reference panel and the use of a 'jump correction' to remove wavelength dependent offsets associated with the boundaries between the different sensor arrays of the ASD system. This pre-processing is performed using the Spectral Analysis and Management System (SAMS) software package (SAMS, 2005). The pre-processed spectra are compiled into a spectral library file that was imported into the ENVI (Environment for Visualizing Images) software package. To better visualize the vertical changes in spectral reflectance properties an IDL (Interactive Data Language) script (provided by C Haselwimmer) was used to build a hyperspectral image cube that stacks spectral data against sample depth to provide a convenient method for visualizing the results (Figure 3.18). Using ENVI, false color composites of three spectral bands focused on specific mineral absorption features were produced to qualitatively investigate the range of mineral assemblages and variation in alteration intensity with depth. A continuum-removal procedure (Clark and Roush, 1984) was applied to the hyperspectral cube to better enhance the depth of specific absorption features as well as remove slope effects that impact the absorption depths and wavelength positions. Qualitative interpretation of major spectral classes manifested in the data was undertaken with reference to the USGS Digital Spectral Library (Clark et al., 2007) in order to identify the dominant mineral assemblages. Using scripts implemented in IDL, the continuum-removed depth and wavelength position of major mineral absorption features in the VNIR-SWIR was determined from the spectral data. These scripts were based on procedures adapted from Haest et al. (2012) that involved fitting polynomial curves of various orders of magnitude to the continuum-removed spectra for different absorption features. The spectra are stacked and continuum removed to highlight the profile subtleties for clarity of comparison (Figure 3.18). Red (2145 nm), green (2205 nm) and blue (2235 nm) define the ALOH absorption feature to distinguish Al-rich mineral phases by color association as a function of absorption depth (Figure 3.18). The resultant spectral parameters were used to determine specific mineral assemblages following the procedures outlined by Haest et al. (2012) as well as providing variables that were cross-compared with the results of methylene blue and XRD analyses. Analysis of the sample spectra was also undertaken using The Spectral Geologist (TSG) software package to provide an independent check concerning the interpreted mineral assemblages (Figure 3.19).

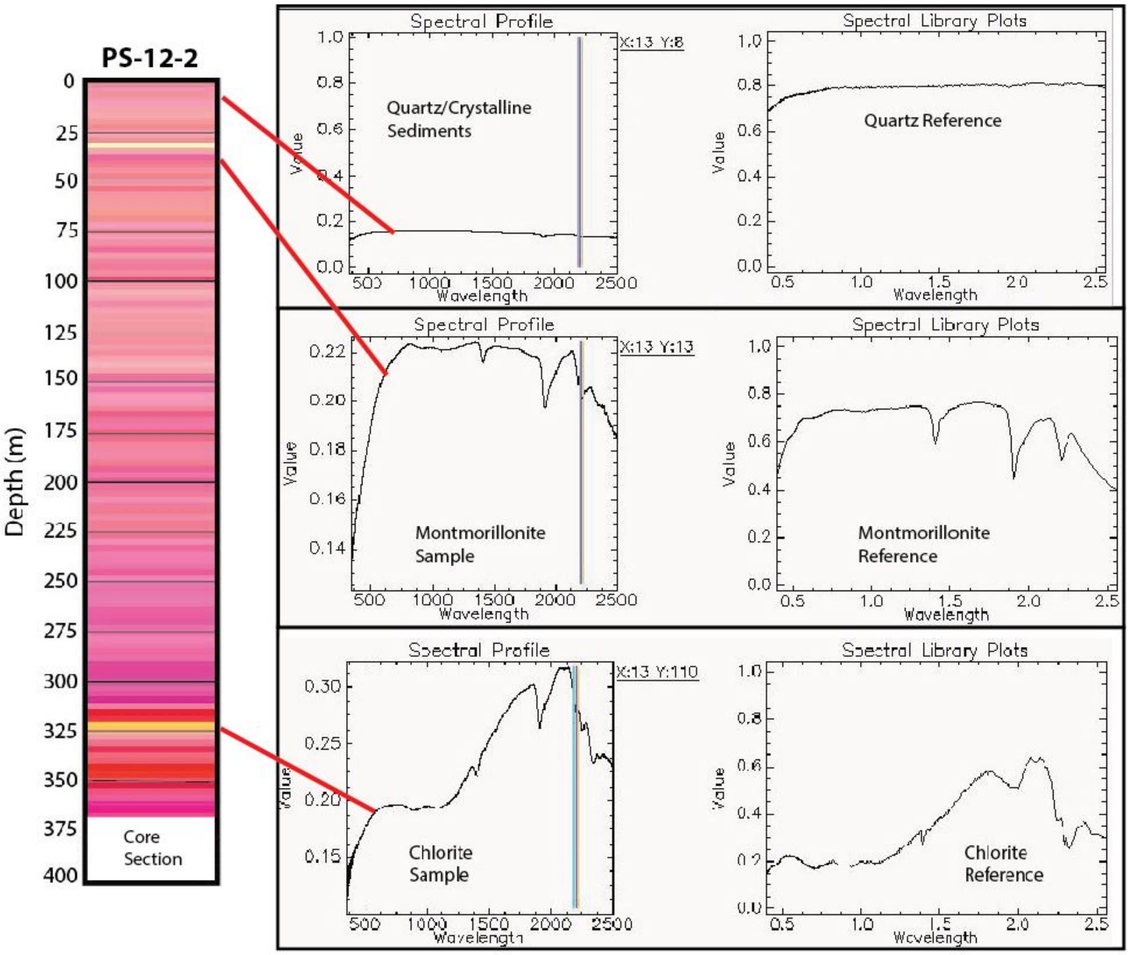

Figure 3.17: Hyperspectral image cube of PS-12-2. Stacked spectra corresponds to sample depth for a total of 375 m depth. Reference mineral spectra (USGS Spectral Library) have been selected: montmorillonite (magenta), chlorite (yellow), muscovite (red), illite and kaolinite (blue), and highly crystalline sediments with quartz as an example (white to very light pink-magenta).

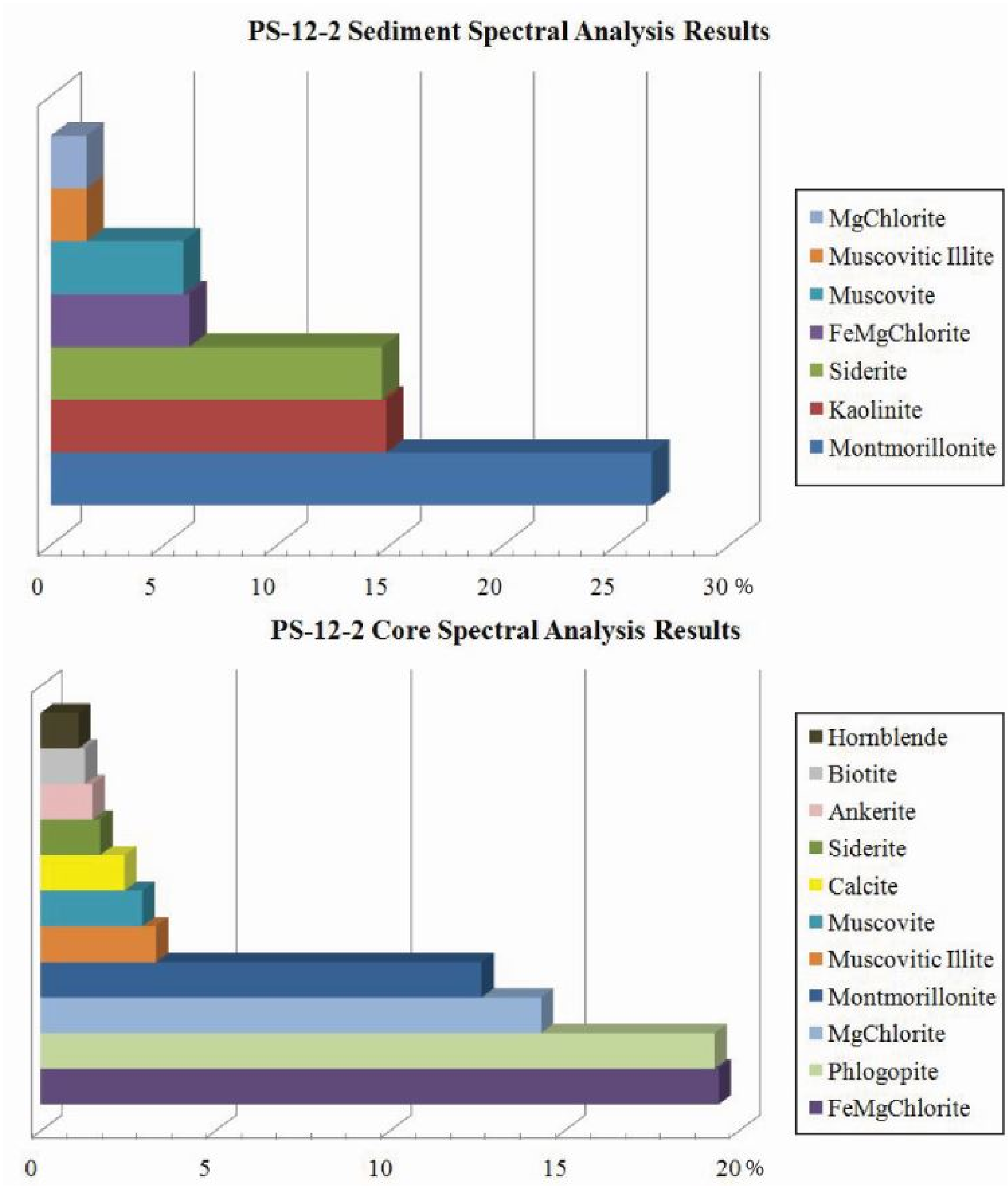

Figure 3.18: The Spectral Geologist spectral analysis mineral results. Results are listed from most abundant to least abundant for both PS-12-2 sediments and core.

Analysis of the reflectance spectra indicates alteration mineral assemblages within the well sediments and core samples comprised of various clays and micas. The dominant mineral assemblages include montmorillonite and chlorite (Figure 3.18). The absorption features of OH at 1400 nm, H_2O at 1900 nm, and specifically the AlOH absorption feature at 2205 nm with shoulder peaks at 2160 nm and 2240 nm are strong indicators of montmorillonite. Chlorite was identified by low reflectance in the visible spectrum, the multiple absorptions in the H_2O band, and a small AlOH absorption on the shoulder of the much more pronounced FeOH band at 2250 nm and MgOH band from 2330-2450 nm. However, muscovite and kaolinite, detected in XRD, were not as easily separated by visual determination in spectral analysis due to the mixed-layer nature of the clay samples and ambiguities in the spectral absorption features. The USGS reference spectra for mixed montmorillonite-kaolinite offered the closest resemblance to sample spectral profiles, but this particular mineral assemblage is almost indistinguishable from pure montmorillonite reference spectra.

To further characterize the extent of alteration within the samples, the White Mica Alteration Index (WMAI) was calculated. This index is the ratio of the AlOH absorption depth of white mica to the depth of the FeOH absorption feature in chlorite (van Ruitenbeek et al., 2005); the ratio increases with white mica relative to the abundance of chlorite (Figure 3.20). WMAI values that plot higher than 0.75 are interpreted to be mostly white mica while chlorite dominates the lower half at 0.5 and below (van Ruitenbeek et al., 2005). The relative Al content of the white micas determines the wavelength position of the AlOH absorption feature and changes with temperature, hydrothermal fluid chemical substitution, and the mineral composition of the host rock type (van Ruitenbeek et al., 2005). Figure 3.20 is a WMAI scatter plot of wavelength values within 2190-2215 nm that is the characteristic range of the AlOH absorption band. The WMAI for the PS-12-2 sediments tend to exhibit a relatively low Al content possibly as a result of increased temperature (100+ °C) or evolving hydrothermal fluid chemistry (van Ruitenbeek et al., 2005). Figure 3.21 shows a similar distribution of WMAI values for the sediments of PS-12-1 and PS-12-3. The deeper sediments and shallow basement surface rock cuttings of PS-12-2 and PS-12-3 plot in or near the chlorite dominant range. The PS-12-2 core displays a wide spectrum of variable white mica-chlorite values. The Spectral Geologist program, designed for automated mineral detection using spectral data, produced results that indicate the abundance of (Fe,Mg) chlorite relative to a lesser amount of white micas such as muscovite and paragonite (Figure 3.19).

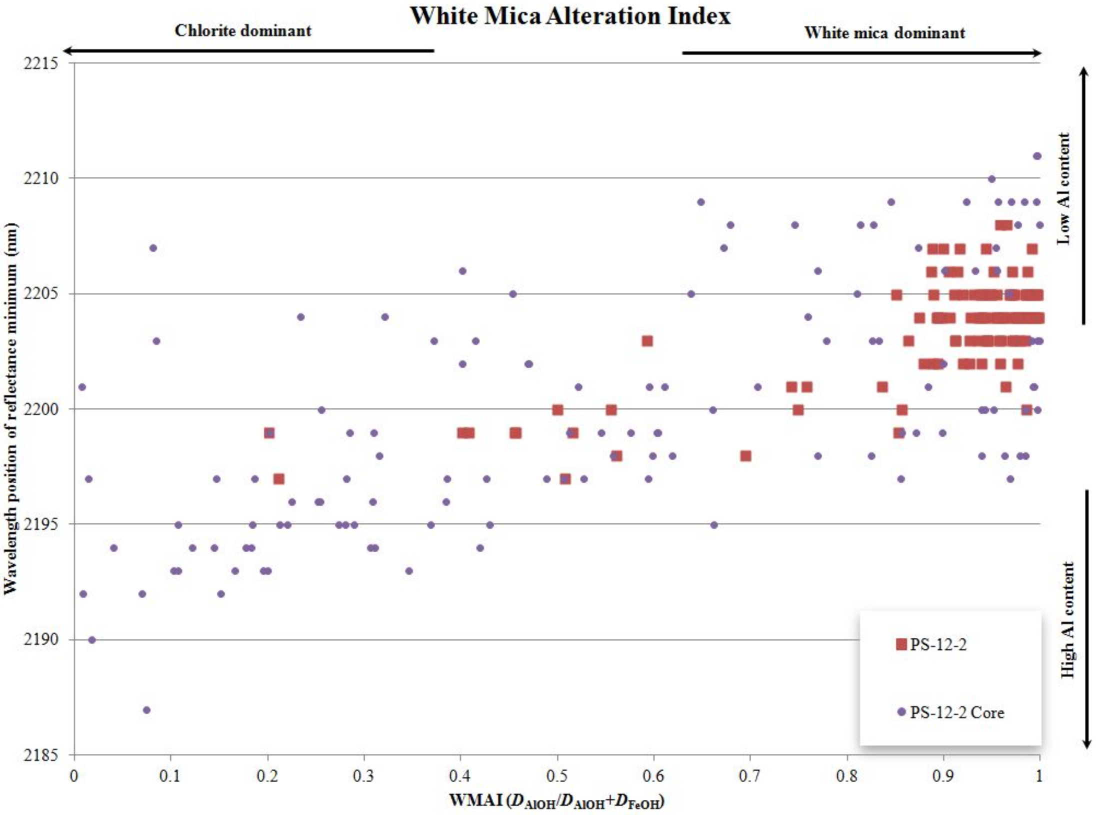

Figure 3.19: White Mica Alteration Index scatter plot for PS-12-2. AlOH and FeOH absorption feature depth and wavelength position changes are plotted.

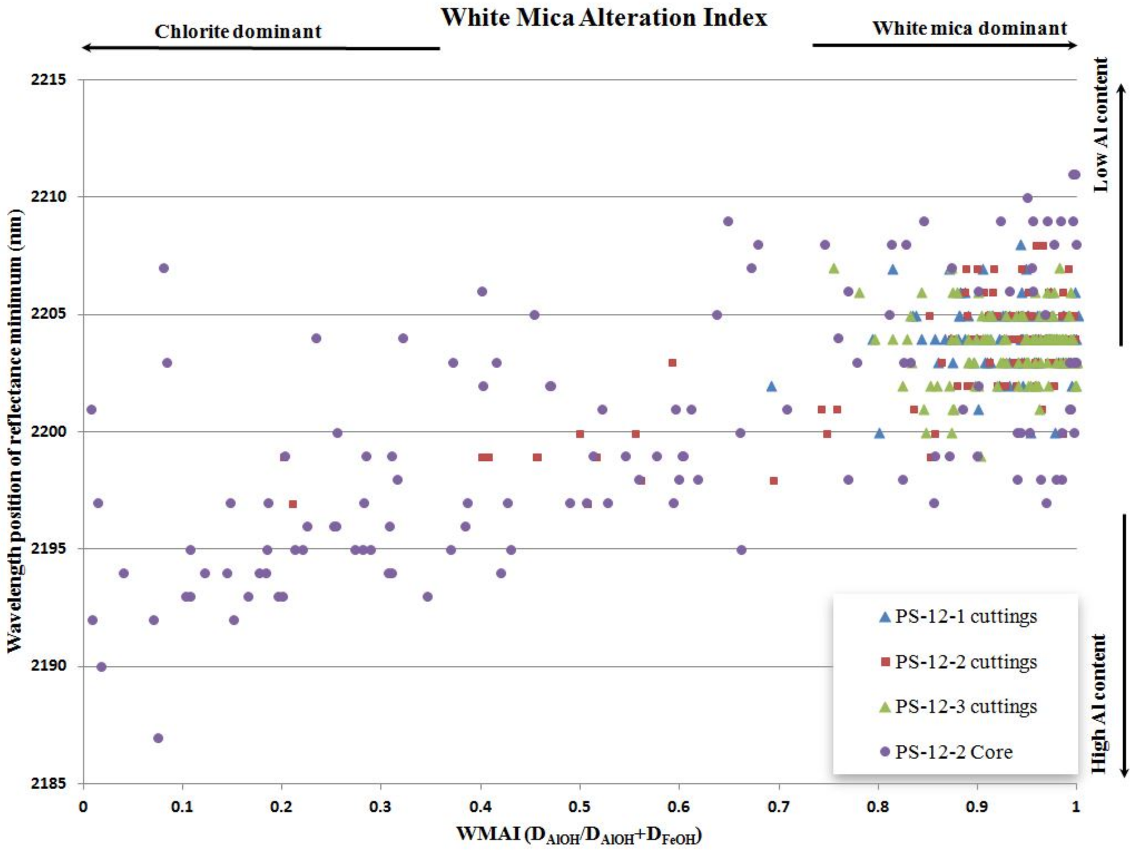

Figure 3.20: White Mica Alteration Index scatter plot for selected wells. PS-12-1, PS-12-2 (and core section), and PS-12-3 AlOH and FeOH absorption feature depth and wavelength position changes are plotted.

3.5.2 Methylene Blue Titration

Methylene blue (MeB) analysis is a common approach to determining the composition of clays intercepted in geothermal exploration (Gunderson et al., 2000). This analysis requires titration of methylene blue into solution containing a powdered sample of clay. In solution, methylene blue is a cationic dye with the molecular structure $C_{16}H_{18}N_3S^+$ that readily adsorbs onto smectite clays due to their very high cation exchange capacity and hydrogen bonding with the alumino-silicate lattice structure (Santamarina et al., 2002; Yukselen and Abidin, 2008). It is an important application as smectite clays form in temperatures in excess of 50 °C and conversion to illite composition begins at 80 °C and becomes increasingly dominant above 100 °C (Gunderson et al., 2000). The results of MeB analysis of clay-rich samples can be combined with zones of low resistivity to delineate areas of possible high-temperature alteration in association with the migration of geothermal fluids (Gunderson et al., 2000). For this analysis, 78 clay samples were analyzed with methylene blue titration.

The procedure used for the methylene blue analysis is provided in Harvey (1993). The main purpose of this method is to fully saturate the clay particles with a methylene blue solution. Drop counts of the methylene blue-clay solution are recorded until a blue halo forms on the paper (Figure 3.22). This halo forms as a result of full adsorption of methylene blue onto the clay structure where the excess methylene blue is suspended in the solution. For each one ml of methylene blue solution required for saturation, 1% swelling clay is estimated. The composition of the clay and a calibrated quantification of $\%_{\text{smectite}}$ is typically ascertained by x-ray diffraction. A range of smectite content was detected in the clay samples in the MeB analysis.

For well PS-12-1, the MeB analysis showed an increase in smectite percentage with depth. The top of the well had an average of 2-3% smectite, which increased to 8.5% near the bottom of the well. In PS-12-2, high values of MeB saturation indicate smectite content up to 10% occurring at 200-300 m depth. PS-12-3 displayed a similar trend and average to PS-12-2. However, it only had a high of 7.5% smectite. The table of MeB values for these wells is located in Appendix B.1-B.3.

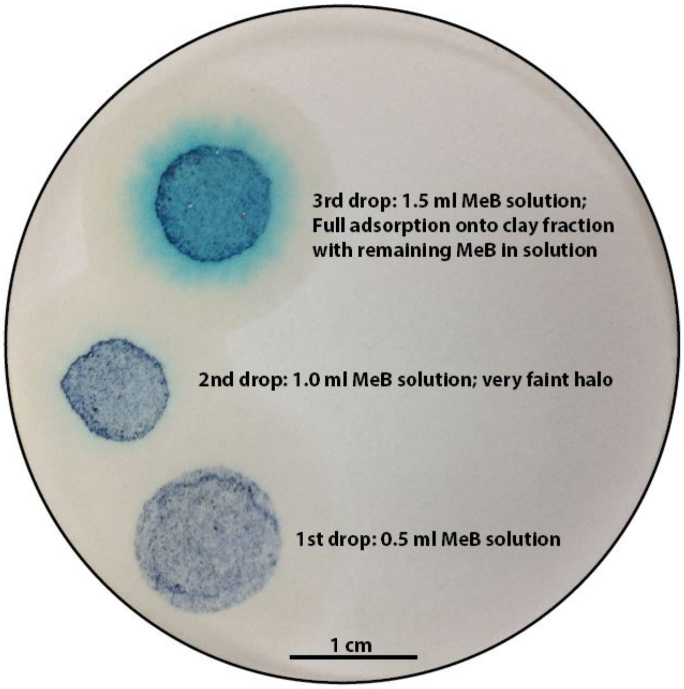

Figure 3.21: Methylene blue solution "halos". Halos indicate excess MeB (Methylene blue) remaining in solution after full adsorption onto free clay fraction in the prepared mixture.

3.5.3 X-ray Diffraction Analysis

Samples were analyzed using the PANalytical X'PERT PRO Materials Research Diffractometer (MRD) x-ray diffraction (XRD) in the Advanced Instrumentation Lab at the University of Alaska Fairbanks. Using a CuKα source, the analytical range was from 2-59 °2θ with a 0.01 step size and 15 seconds per step. Four clay samples obtained from drill cuttings from PS-12-2 were prepared for oriented clay x-ray diffraction analysis. The clays were decanted, separated from >2μm particles, and saturated with a 2M solution of $MgCl_2$ as expanding with an index cation yields predictable results that allow for differentiation of the clay mineralogy (Bain et al., 1987). The clays were then oriented in a vacuum filter apparatus and placed on glass slides. Separate XRD runs were completed after air-drying and ethylene glycolation. Expandable clays like smectites, principally montmorillonite, shift in measured Å peaks of 10 Å air-dried at 7 °2θ to 14 Å at 5 °2θ with ethylene glycol (Mosser-Ruck et al., 2005). The results of XRD analysis are compared to the results of the other methods to test the agreement of mineral determinations.

The common minerals detected in the XRD results include abundant montmorillonite, common illite/chlorite, kaolinite, and minor biotite (Figure 3.23). Peak matches within the 2-59 °2θ range and respective d-spacings for known minerals show a strong match with montmorillonite clay. Peak position and count intensity matches with other minerals may be slightly variable as the samples were oriented with the C-axis of the clays preferentially aligned. Thus, correlations to peaks of other mineral structures at a specific °2θ are limited to the 001 line. Peaks on other lines and orientations may not show up. When considering a mineral identification, this orientation served as a mechanism for filtering out other mineral structures by looking at database results of measured °2θ angles and d-spacing values at the 001 line.

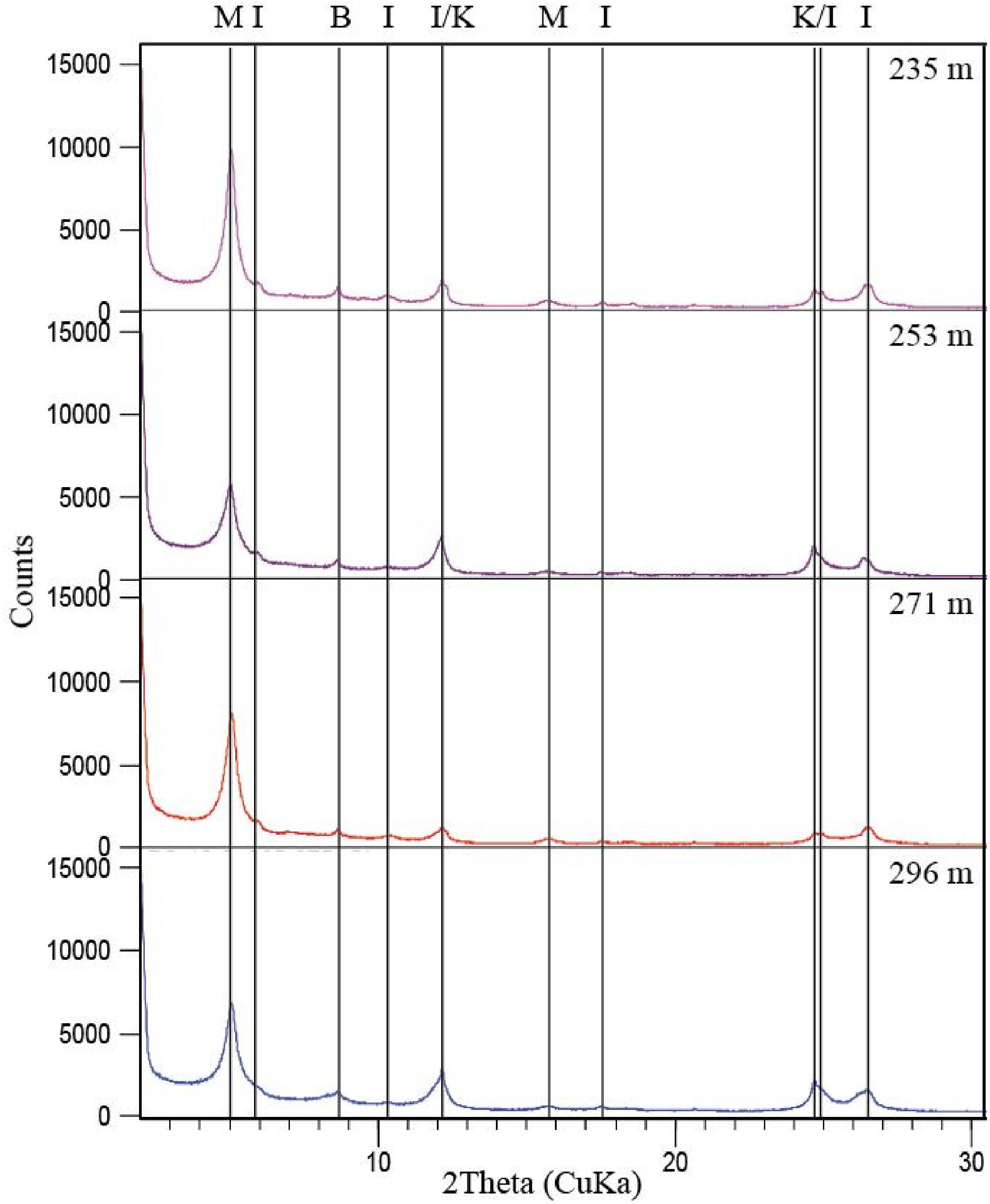

Figure 3.22: XRD results of PS-12-2 clay samples. XRD detected (M) Montmorillonite, (I) Illite, (K) Kaolinite, (B) Biotite from depths of 235-296 m in well PS-12-2. Results are dominated by montmorillonite with variable abundances of illite and kaolinite composition and minor biotite.

3.5.4 Thin-section Characterization

The thin-sections were created from selected samples that represent the three distinct lithologies present in the PS-12-2 core. The bedrock is composed of mica schist with a granitic pegmatite dike and a diabase dike. A thin-section was also created from a field sample of a previously identified granitic pegmatite dike for comparison (Turner et al., 1979). Photomicrographs of the biotite schist bedrock, pegmatitic dike, diabase dike, and the contact of the pegmatitic dike and biotite schist are illustrated (Figure 3.24). The pegmatitic dike contains plagioclase and quartz minerals of sizes ranging from 0.5-2 cm. Minor biotites are seen in the pegmatite at the contact with the biotite schist. The diabase dike has <3 mm sized hornblende crystals and several thin (<1 mm) quartz-filled veins with a groundmass of very fine plagioclase crystals. Fine-grained pyrite (only discernible in reflected light) is very common as a replacement mineral along both dike-schist contacts.

Mineral alteration seen in thin-sections of the core is limited to micas at or near dike contacts, pyritization in quartz veins and mineral contacts, and hornblende replacement in the deeper diabase dike sections. Minor alteration is present in some biotites producing a mottled sweeping extinction. Mineral degradation and the early stages of hornblende replacement by quartz are visible. The inspection for clay content in thin-section and precise alteration accessory mineralogy is best pursued in scanning electron microscopy and microprobe analysis, both of which are expensive endeavors and were not undertaken in this research.

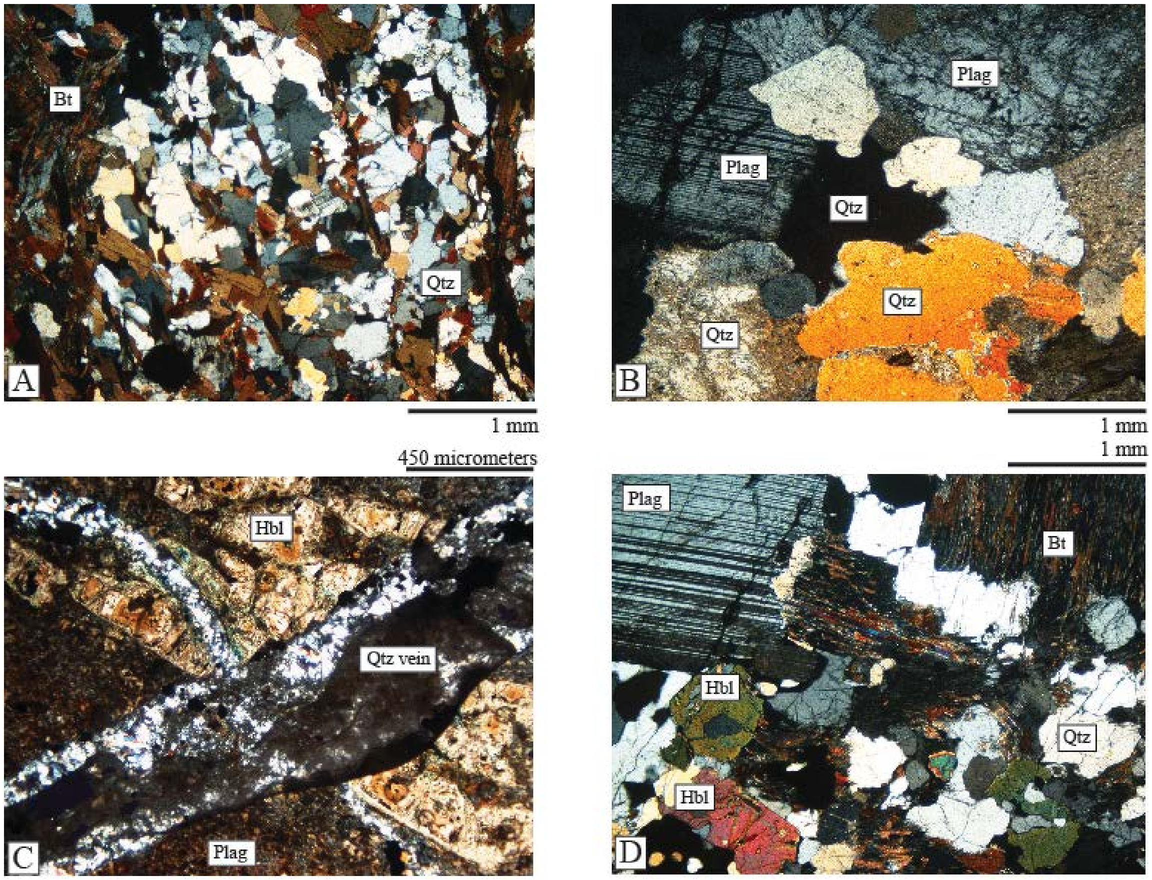

Figure 3.23: Thin-section photomicrographs of bedrock core samples. All images are under crossed polars. [A] Representative sample of the biotite (Bt) schist. Minor alteration is present in some biotites. [B] Pegmatitic dike with large plagioclase (Plag) and quartz (Qtz). [C] Diabase dike with a 3 mm hornblende (Hbl) crystal cut by two quartz veins with a groundmass of plagioclase. Mineral degradation and the early stages of hornblende replacement by quartz are visible. [D] Contact of the pegmatitc dike and biotite schist. Hornblende, quartz, plagioclase, and biotite are common.

3.6 Discussion of Analytical Results

The sediments and mica schist bedrock are experiencing hydrothermal alteration as evidenced by a mineral assemblage of montmorillonite, illite, and kaolinite, as well as a host of accessory minerals. The mixed montmorillonite, illite, and kaolinite clays suggest low-temperature alteration between 80-120 °C in both the sediments and bedrock.

The AlOH absorption depth and methylene blue estimated smectite content is plotted for wells PS-12-1, PS-12-2, and PS-12-3 with the aim of correlating montmorillonite-rich horizons as proxies for hydrothermal alteration (Figure 3.25). Discovering these zones of hydrothermal alteration can highlight the pathways, both past and present, of hydrothermal fluid flow in the geothermal system. The AlOH absorption depths for each well show a general increasing trend to the bedrock surface, yet smaller scale variations do not typically correlate directly well-to-well. One notable exception is the two data points in PS-12-1 at ~30 m depth that exhibit significant absorption up to 0.07-0.09%. These two points are indicators of montmorillonite on their respective spectral profiles. When compared to the other wells, AlOH absorption increases appear to occur at the same depth. However, this is limited to only a few data points and the absorption features of PS-12-2 and PS-12-3 are too subtle for a well-supported correlation. The methylene blue data for each well show a trend similar to the increasing trends of the AlOH absorption features to the bedrock surface. Each well exhibits low values (<3% smectite) until 130 m depth where the wells display an increase in smectite content to the bedrock. Also, similar to the AlOH trends, small scale correlations between wells are not achievable. Increasing the sample data may help to resolve this issue.

Examination of the methylene blue and AlOH absorption data reveals broad similarities yet there is a lack of correlations at a higher frequency (Figure 3.25). Both methods produce trends with depth that signify increases in montmorillonite in all three wells. PS-12-2, for example, shows the trends with depth against lithology, temperature, and mineralogy as detected through The Spectral Geologist and XRD (Figure 3.26). Methylene blue and AlOH absorption both increase and decrease in identified clay-rich intervals. It is important to note that AlOH absorption is not uniquely a montmorillonite or smectite indicator and could be indicating the presence of other minerals as well. Also, the methylene blue analysis is only a measure of its affinity to the smectite clays in suspension. Montmorillonite is a specific smectite clay and other smectite clays in the sample solution could affect the outcome of estimated montmorillonite content. The discrepancy in the two trends may also be the result of heterogeneity of the clays and sediments. Increases in illite or kaolinite relative to montmorillonite could produce the variation observed in both trends. This is supported by Figure 3.26 where plotted XRD results show multiple clay minerals are detected throughout the selected well cutting samples. Temperature also does not appear to greatly influence the higher frequency changes of the two methods (Figure 3.26). This suggests the heterogeneity of the clay-rich intervals may be influenced by other environmental conditions.

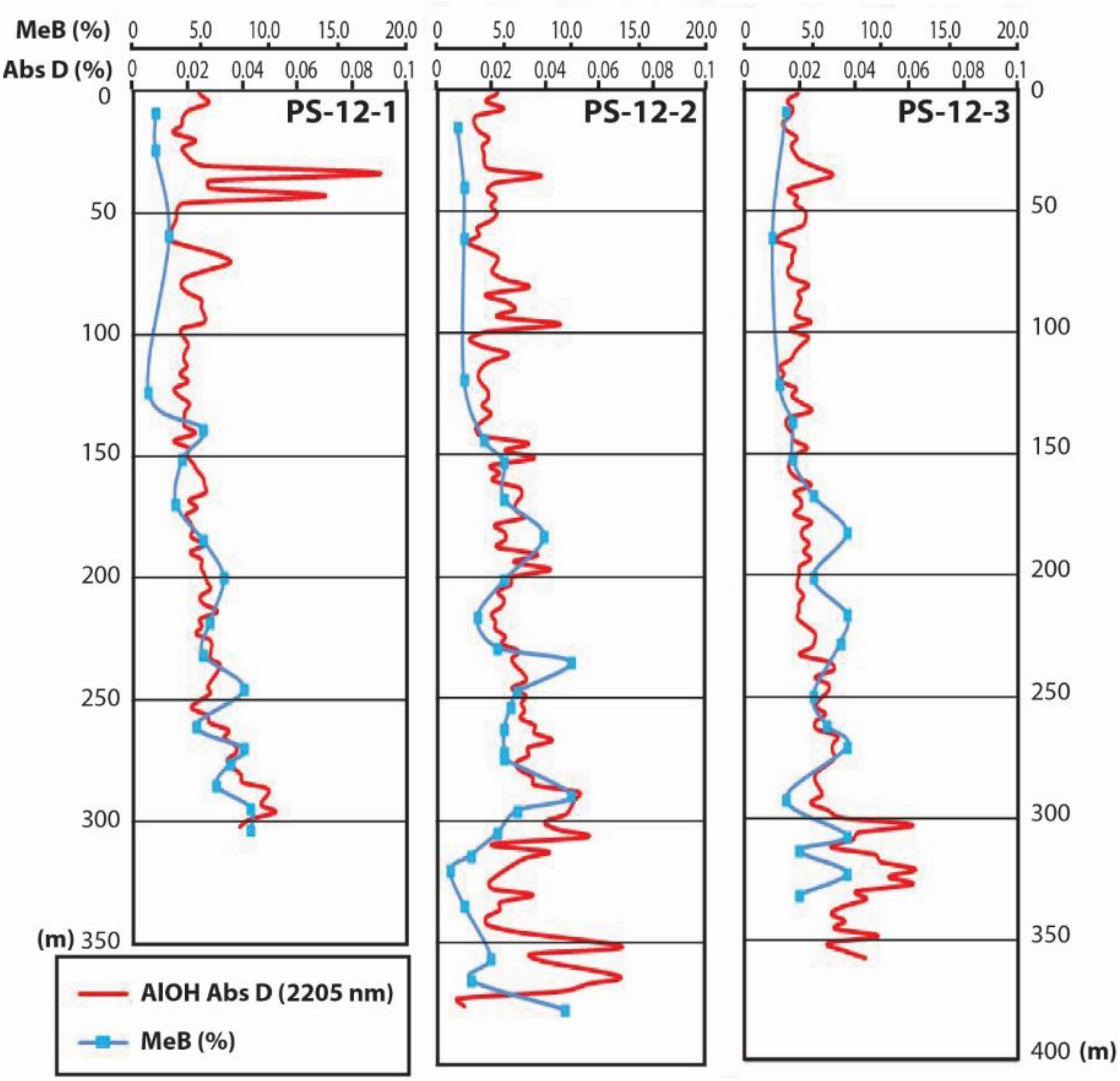

Figure 3.24: AlOH absorption depths and methylene blue results combined plot. AlOH absorption feature depth (AlOH D) at the 2200 nm wavelength (or approximately located at the maximum depth of absorption for this specific feature) and methylene blue estimated smectite content in percent (MeB %) plotted against depth for wells PS-12-1, PS-12-2, and PS-12-3. Absorption depth is measured in total percent absorbed light (not reflected).

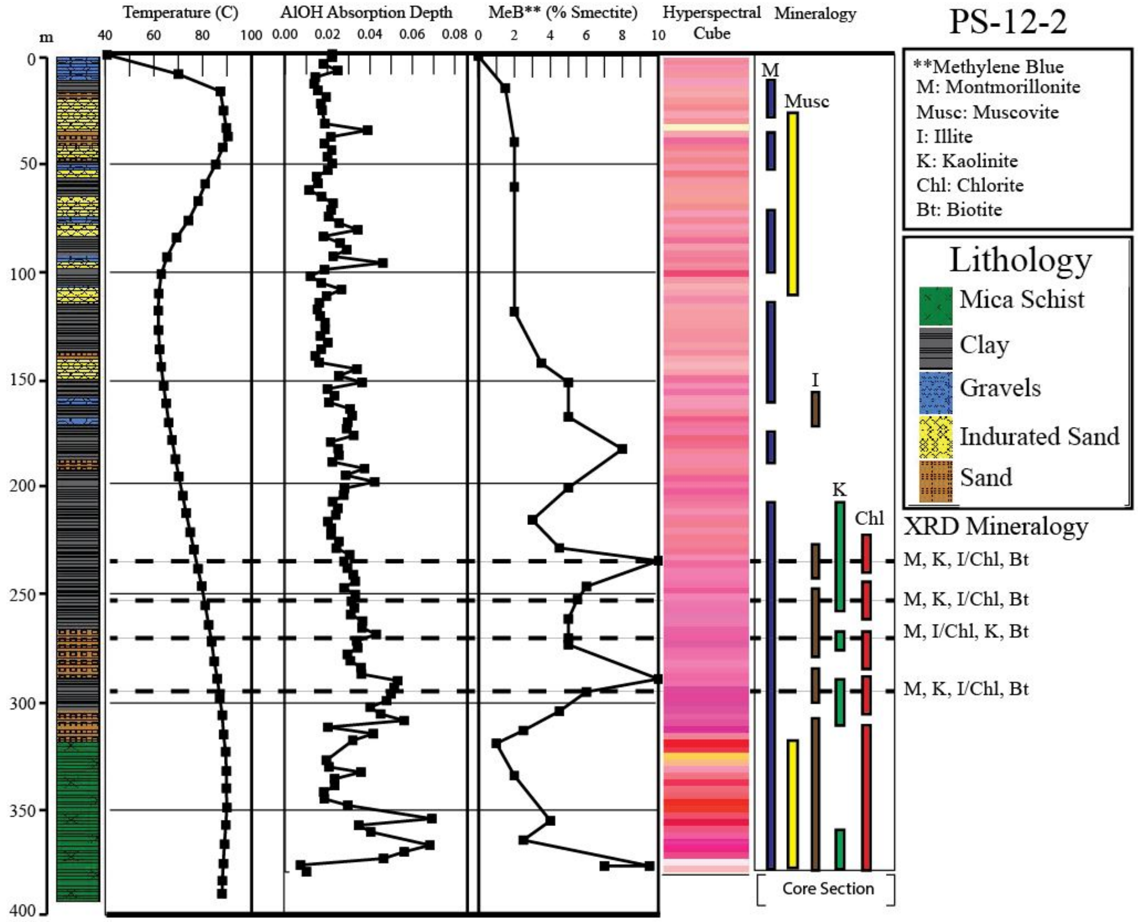

Figure 3.25: Lithology, temperature, spectral, and methylene blue analysis plot. A correlation of results for PS-12-2. All data sets are compared to detect changes in mineralogy that relate to the degree of past hydrothermal alteration.

The degree of alteration present in the Pilgrim Hot Springs wells resembles an argillic alteration facies with the assemblage of white micas and clays, dominantly kaolinite, montmorillonite, and illite (Mas et al., 2006). The formation of these clays is strongly dependent on fluid temperature and also on fluid chemistry (Browne, 1978). The presence of kaolinite indicates an environment with temperature and pH conditions necessary to strip the alkalis from muscovites as well as iron, calcium, and magnesium from montmorillonite through the process of hydrolysis (Guilbert and Park, 1986). The montmorillonite in the PS-12-2 core provides further evidence for argillic-style alteration as it is a common alteration product in many ore vein deposits and hydrothermal systems (Guilbert and Park, 1986; Browne, 1978). Similarly, illite and chlorite typically require a temperature range of 100-200+ °C for formation and are commonly used as a geothermometer (Gunderson et al., 2000; Harvey and Browne, 2000; Lagat, 2007). The temperatures required for the mixed-layer smectite-illite clays detected in the well samples are most likely the result of the hydrothermal alteration within the system and would require greater burial depth for conversion to illite through diagenetic processes alone (Jennings and Thompson, 1986). Chlorite, although common in geothermal systems, is most likely derived from the low-grade metamorphics of the nearby mountains and dike intrusions in the basement that may have had more impact on mineralizing the shallow basement than hydrothermal processes. The low-grade metamorphism and dike intrusions of the bedrock may likely be responsible for the abundant presence of chlorite and mineral replacement in the dikes, as the temperatures required for their crystallization are well above any other hydrothermal alteration features observed in the sediments. Regardless, extensive pyritization and the clay mineral assemblage suggest an argillic-style alteration facies that is present in both the core and sediments.

The alteration assemblage points to past temperatures at or slightly elevated above current conditions of hydrothermal activity at Pilgrim Hot Springs. The presence of abundant pyrite and the clay mineral assemblage of montmorillonite, illite, and kaolinite is a common feature of both low- and high-temperature geothermal systems around the world (Browne, 1978). The various geothermal systems of Yellowstone in Wyoming, The Geysers in California, many systems in New Zealand, the Philippines, and Iceland all contain the presence of these particular minerals (Browne, 1978). The lack of high temperature (>150 °C) alteration in the sediments may indicate that the heat source remained nearly constant through time.

Chapter 4: Lithostratigraphic and Temperature Model Development

4.1 RockWorks15 Model Parameters

RockWorks15, a geologic modeling program from Rockware, was used to create the visual model to generate cross-sections and maps for data comparison. All Pilgrim Hot Springs well data were imported into the program for mapping, contouring, visual analysis, and 3D modeling. The model encompasses an area of 4 km^2 that includes the observed anomalous thawed ground of the hot springs and surrounding boundary of permafrost (Figure 4.1). The node density of the model is 20 m laterally in the X-axis and Y-axis and ~2 m (5 ft) along the Z-axis. Lithologic observations made from describing drill cuttings were directly imported into the program as discrete intervals within each digital well log.

Well data points, both lithologic and temperature, are interpolated via an anisotropic modeling algorithm. The anisotropic algorithm constrains the interpolation of values to the nearest data points in the surrounding model nodes much like connecting a series of dots. This method is most applicable to continuous downhole data sets similar to the lithologic and temperature logs. The inverse method, isotropic modeling, assigns node values in between wells with an equal distribution in all directions. This interpolation of data does not reflect the real-world spatial variability of the sediments or hydrologic controls on the temperatures. The anisotropic algorithm more realistically constrains the data in interpolation as well as extrapolation to the model boundaries.

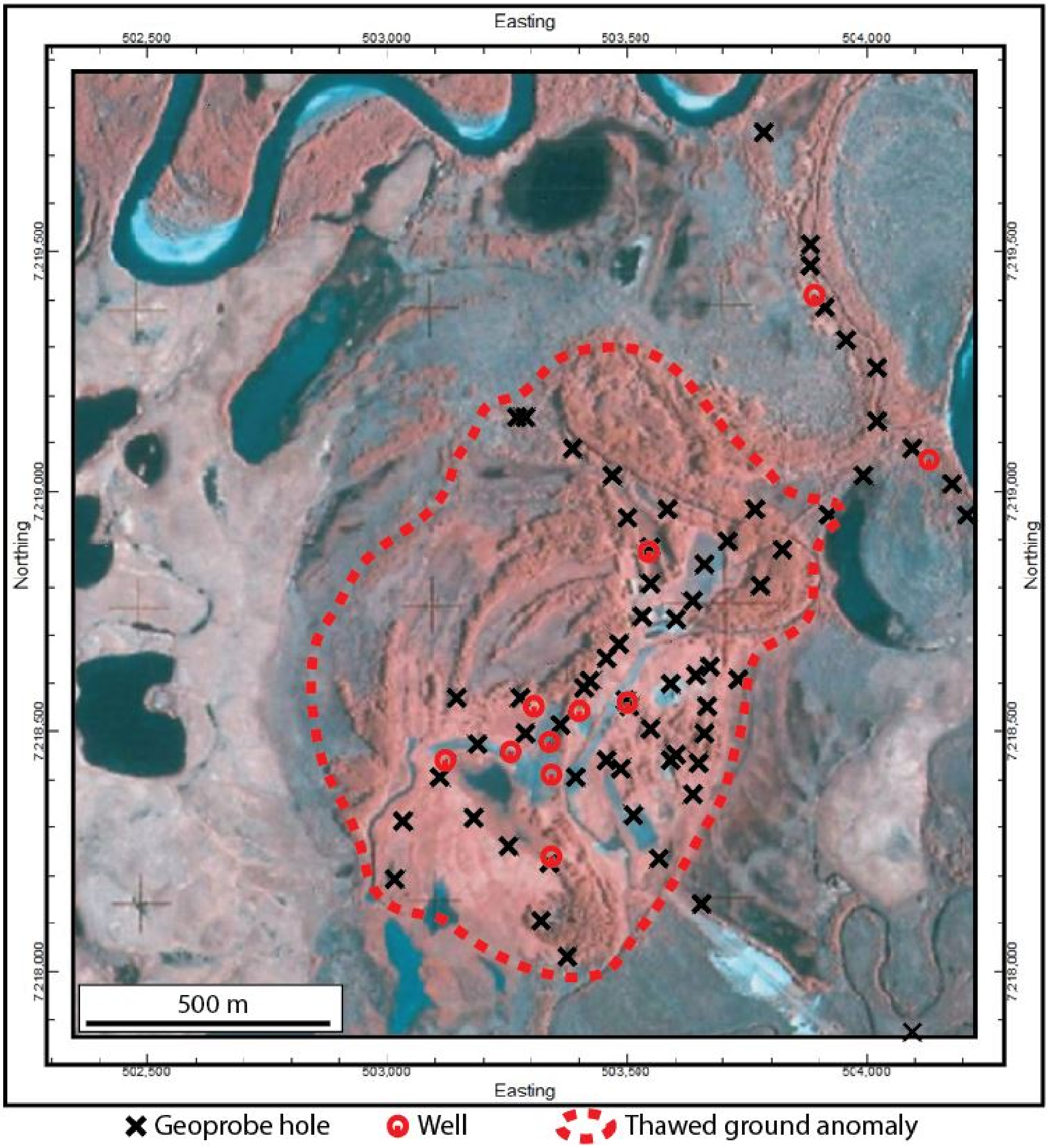

Figure 4.1: RockWorks15 conceptual model dimensions. Boundaries of the RockWorks15 model includes all Geoprobe and well locations. The model dimensions are 4 km^2. The map is a USGS Alaska High-Altitude Photography near-infrared image.

4.2 Model Assumptions and Limitations

Assumptions and Limitations

Several assumptions were integrated into the construction of this model:

- The porosity and permeability values obtained from published sources are accurate and can be applied to sediment analysis of well cuttings for this model.
- The geophysical well logs, most notably gamma ray, can be reliably correlated across the site to provide the best understanding of the subsurface stratigraphy.
- Well temperature data reflects a fully equilibrated ambient temperature.

The conceptual model is also restricted by limited understanding of the structural geology controlling fluid flow under Pilgrim Hot Springs. The placement and orientation of any faults at depth or offset in sediment layers between wells is difficult to ascertain due to relatively small area of exploration. The lack of any seismic reflection data makes interpreting the bedrock surface difficult as well. Another limitation to the model is the confidence in the sampling and sediment description reports of previous exploration drilling at the site. Without clarity on the conditions and procedure of sediment classification during the earlier drilling, previous lithologic logs utilized in the conceptual model have the potential to be overgeneralized or miss thinner, yet important sediment intervals.

4.3 Data Integration

4.3.1 Lithostratigraphic Model

Unconsolidated to poorly consolidated Quaternary alluvial, fluvial, glaciolacustrine, and brackish lagoon sediments ranging from clay to gravel were intercepted in the wells to depths of 320 m where the mica schist basement was encountered below. Characterization of the drill cuttings from each well were used to produce lithologic logs that provide the framework for development of a conceptual geological model of the geothermal system. The sediments were characterized based on mineralogy, grain shape, sorting, and distribution of grain size from clay, silt, very fine-coarse sand, and gravels. The sediment characterization also provides porosity and permeability values that are important as input parameters for the numerical reservoir model.

In Figure 4.2, a SW-NE cross-section is used to demonstrate the lithostratigraphic stacking of the underlying sediments. Both N-S and E-W cross-sections are seen in the 3D model image (Figure 4.3). Coarse sand is the most common sediment type derived from the edge of the proximal alluvial apron. Several laterally extensive clay layers are evident and are most abundant in PS-12-1. The thickest and most extensive clay-rich layer seems to be located between depths of 200-275 m, about 50 m above the buried basement surface, and is intercepted in wells PS-12-1, PS-12-2, and PS-12-3. Another clay layer above the basement at ~300 m is present in all of the deep wells except

PS-12-3. The extensive clay layers may have formed during periods of increased subsidence relative to sedimentation or during high sea level as a marine-influence brackish lagoon. Understanding more about these clay layers beyond their geometry and alteration is outside of the scope of this work. Beneath this clay is a zone of silty sand that extends down to the basement-sediment contact. There are other laterally extensive clay layers and they are typically grey and silty-sandy (Figure 4.2). The lenses of gravel, most likely fluvial channel lag, have the highest primary porosity of the sediments and allow for the best communication of groundwater into the system as well as hydrothermal fluid migration. The gravels are typically thin and interbedded with clay or form distinct layers in the indurated zones.

Indurated sediments occur in the subsurface to the basement with varying degrees of cementation. The indurated sediments have a clean silica cement and tend to be moderate to well-sorted silty sand. The cement was analyzed through XRD and was found to be principally silica with trace amounts of muscovite and calcite (Woodward-Clyde, 1983). Penetration of these zones occurred in every well with the exception of S-1 and S-9. Induration seems to be greatest around PS-4 and forms a "chimney" with various lateral splays up section (Figure 4.4).

The composition of the bedrock is a mica schist that was determined from the lowermost ~20 m of core from the well PS-12-2. Bedrock was also intercepted in PS-12-3 with possible difference in depth. Due to the obliqueness of the cross-section, the actual change in depth to bedrock between the two holes is less dramatic than Figure 4.2

indicates. The maximum difference is ~10 m where the depth to bedrock in PS-12-3 might be lower. The exact bedrock contact while drilling PS-12-3 was ambiguous and was only indicated by an increase in mica flakes in the well cuttings. If this is a small offset and not the effect of changing surface topography, this could be evidence of a fault at depth. However, the orientation and dip of the probable fault remains elusive.

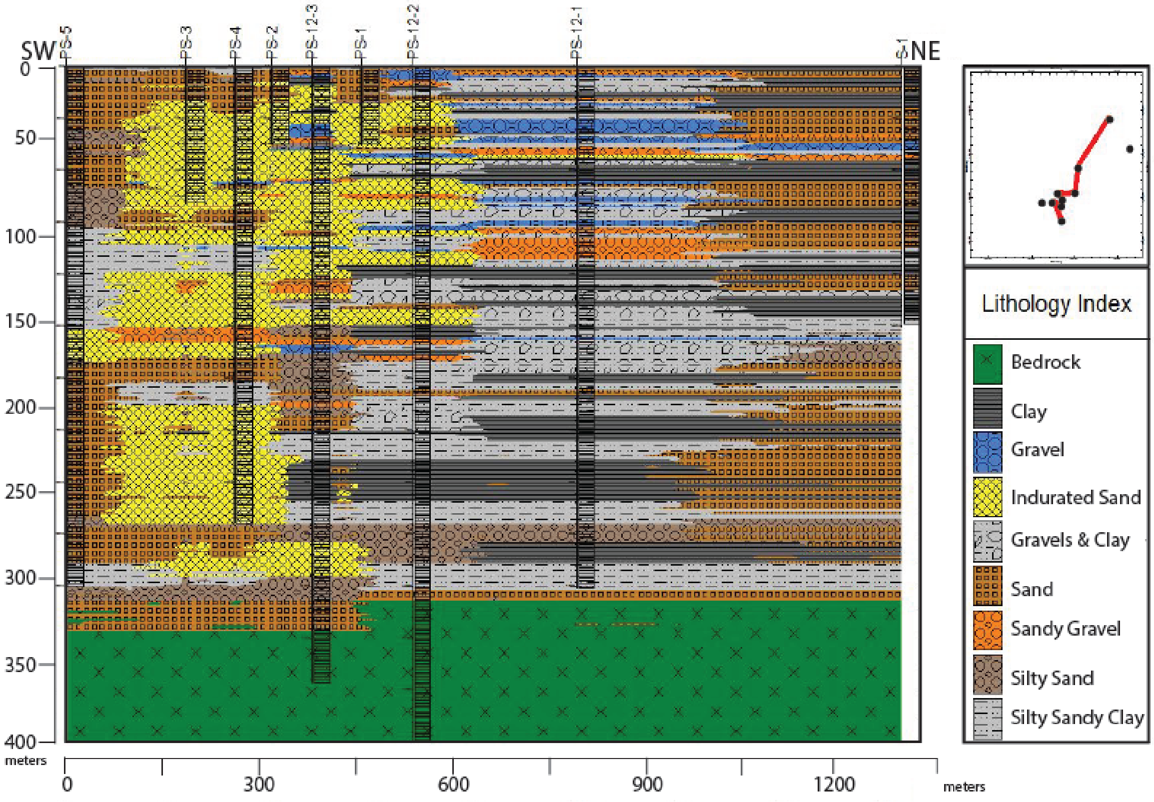

Figure 4.2: Southwest-northeast cross-section of interpolated lithologic logs. Created in RockWorks15.

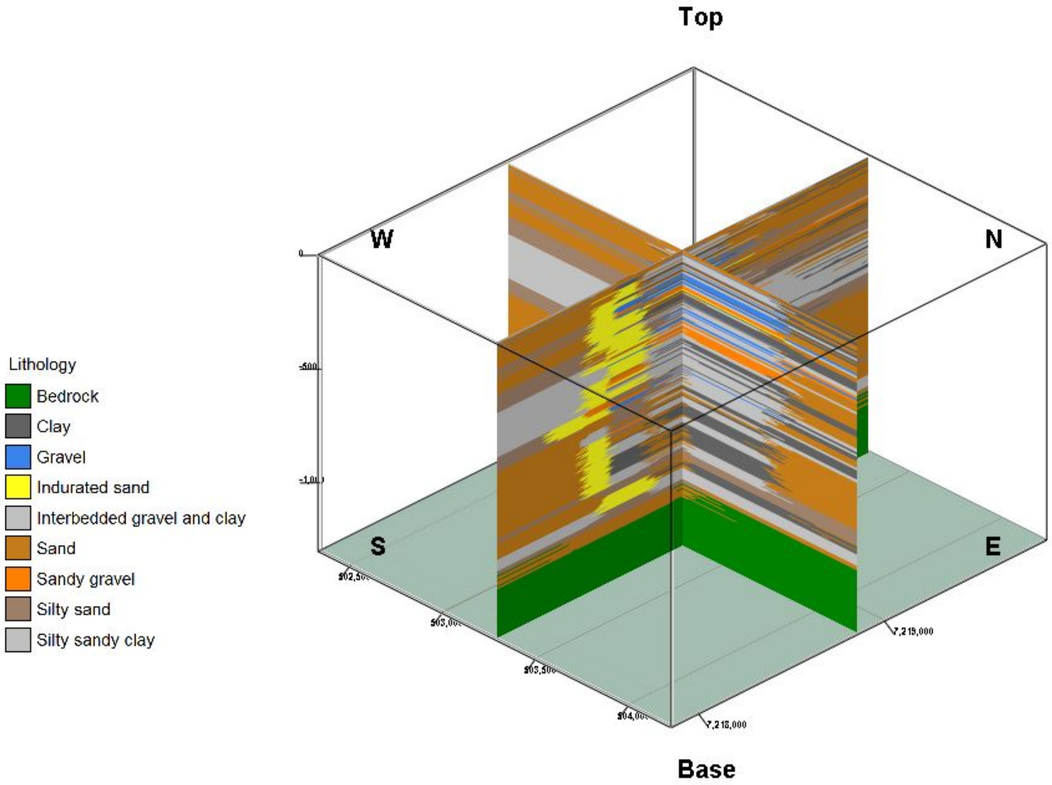

Figure 4.3: RockWorks15 3D model of the interpolated lithologic logs. Reservoir stratigraphy is interpolated between wells and extrapolated out of the model area.

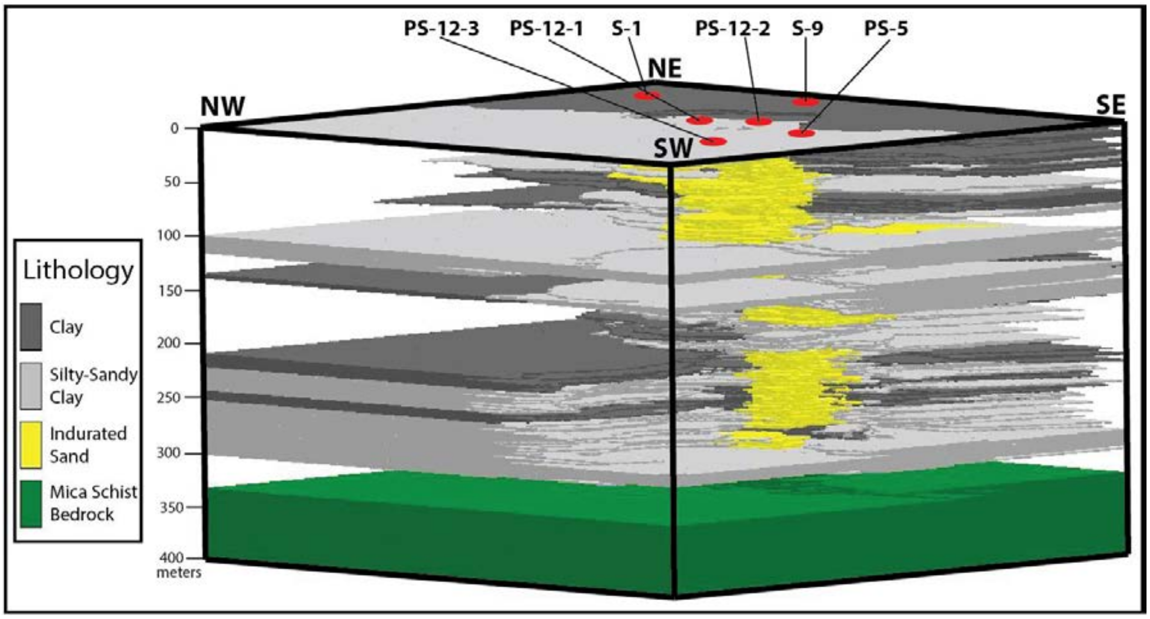

Figure 4.4: RockWorks15 3D model of major clay intervals and indurated zone. Modeled low permeability hydraulic barriers of clay intervals and the indurated zone with a "chimney-style" morphology extending from basement to surface. The six deepest wells are plotted on top.

4.3.2 Temperature Model

Temperature logs from the 11 wells and 64 Geoprobe holes were incorporated into the RockWorks15 isotropic model to produce the distribution (Figure 4.5). This temperature model has the same dimension of 4 km^2 as the lithostratigraphic model. The conditions of the model include the highest temperature 91 °C measured at depth to the lowest temperature of 1 °C measured in the permafrost. The permafrost temperatures were measured in Geoprobe holes to establish background temperatures. This range highlights the anomalously high heat of the hot springs in the center of the model. The western, southeastern, and eastern boundaries are marked by permafrost to depths of 100 m. The model extrapolated the cold background temperatures with a slightly increasing temperature gradient down to the bottom of the model. The increasing gradient of background temperatures surrounding the hot springs in the model is influenced by interaction with the hotter fluids at depth. The 40-50 °C isotherms extend from the center of the model to the southwest. Similarly, 40-50 °C isotherms are close to or below the basement surface on the edges of the model. The river cuts off the northwest corner of the model where no Geoprobe or well data is available.

To achieve an overall temperature distribution that reflects current observations from the field and other independent observations (Chittambakkam et al., 2013; Daanen et al., 2012; Haselwimmer et al., 2011), control wells were inserted into the model by using Geoprobe temperature data. The control wells were synthetically replicated from actual Geoprobe holes that intersected permafrost. The wells were placed at the model boundaries to simulate realistic conditions and constrain the temperature model iteration. Three control wells (two on the western boundary and one in the southeast corner) were placed down to 30 m depth where the pink, ~1 °C isotherms are seen in the model to make the permafrost more robust (Figure 4.5). With a more constrained temperature model, the isotherms better reflect the nature of the geothermal reservoir.

The vertical and horizontal temperature distributions show the center of the geothermal system where the north-south and east-west cross-sections intersect (Figure 4.6). The geothermal system forms a large plume from the basement to the shallow subsurface. The width of the plume gradually decreases upwards where three depth slices and two cross-sections show the narrow neck of the 90+ °C temperatures of the plume between wells PS-12-1, PS-12-2, and PS-12-3 (Figure 4.7-4.8). The characteristics of the temperature model combined with the framework of the geologic model produce a cohesive conceptual model of Pilgrim Hot Springs discussed in the next chapter.

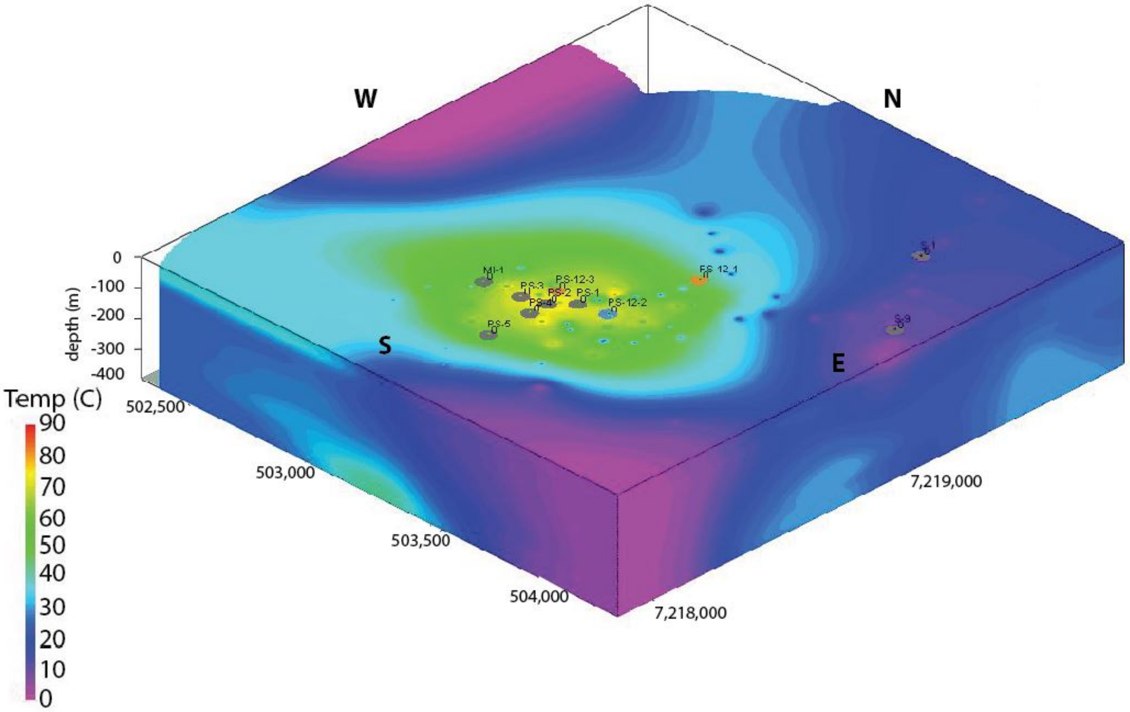

Figure 4.5: Southeastern view of the RockWorks15 temperature model. The total depth is 400 m and 4 km^2 wide. All eleven wells from the site are plotted.

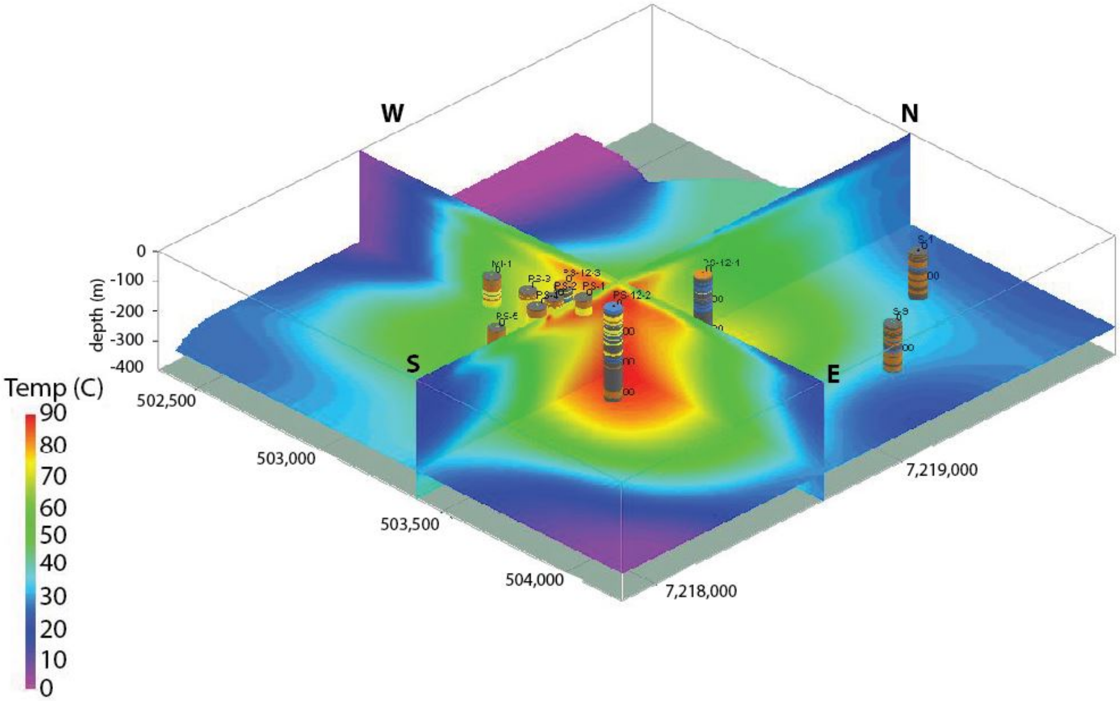

Figure 4.6: Vertical and horizontal slices of the RockWorks15 temperature model. A southeastern view of the RockWorks15 temperature model with north-south and east-west cross-sections and a 300 m depth horizontal temperature distribution slice slightly above the basement surface. All eleven wells are plotted as reference points.

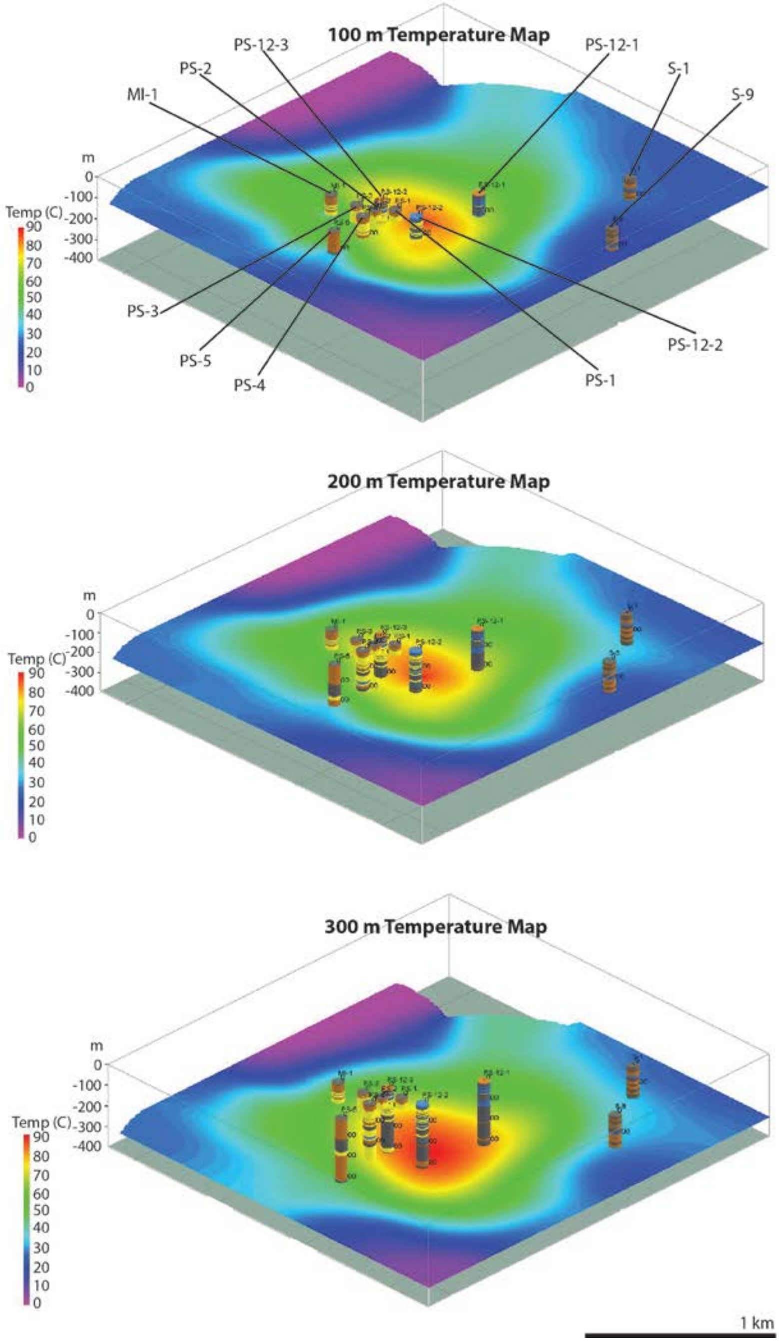

Figure 4.7: Three depth maps of the RockWorks15 temperature model result. A southeastern view of three depth slices at 100, 200, and 300 m from the RockWorks15 temperature model indicate the extent of the higher temperature distribution which narrows from the basement surface to the shallow subsurface. All eleven wells are plotted as reference points.

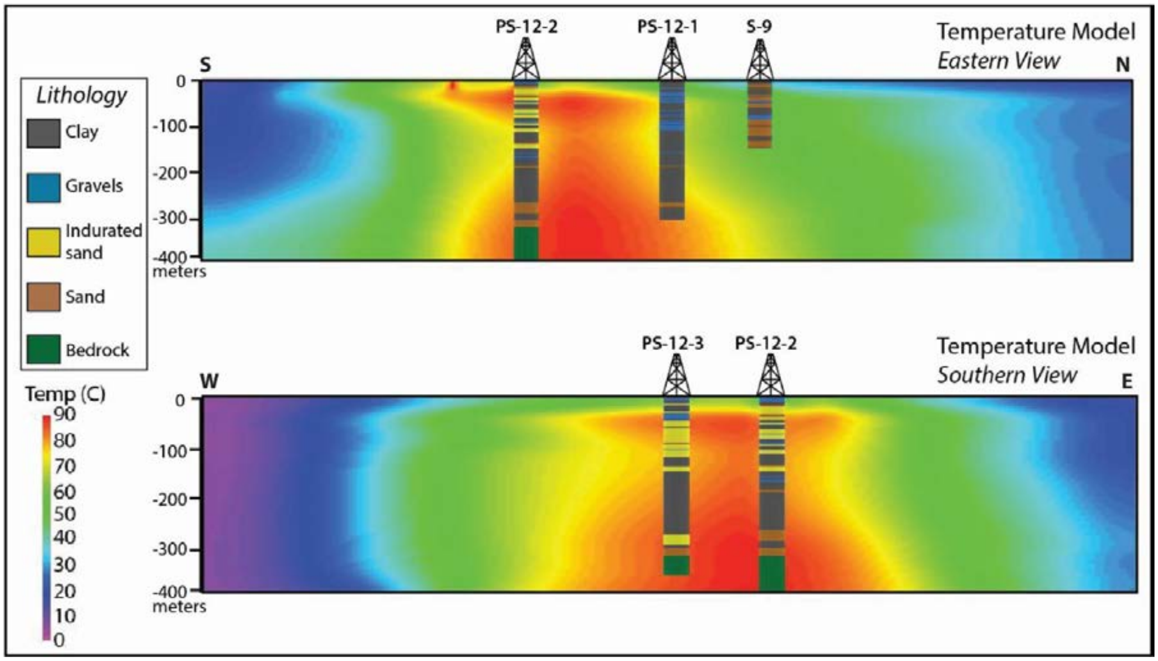

Figure 4.8: Two cross- sections of the RockWorks15 temperature model. The top is an eastern view (N-S) and the bottom is a southern view (W-E). Reference wells show lithostratigraphic units. The profiles are 2 km wide.

Chapter 5: Development of the Conceptual Model

5.1 Introduction

The goal of building a conceptual model of a particular resource is to best assess the gathered data as a cohesive picture of where different observed anomalies may correlate (Cumming, 2009). This provides possible targets for exploration. Essentially, this conceptual model integrates the cross-section of interpreted stratigraphy and structure, interpolated temperature isotherms, and mapped geophysical and geochemical surveys. These are overlaid to highlight the framework of the geothermal system. Understanding the geothermal system through a conceptual model allows for the prediction of subsurface conduits for the migration of hydrothermal fluids.

In order to achieve this understanding, several data sets are assessed and used to develop the conceptual model. Initially, lithostratigraphic relationships are surmised from lithologic and geophysical well logs. These relationships include comparing well log response to lithology and correlating from well to well. The correlations guide the construction of the 3D lithostratigraphic model as constraints to anisotropic interpolation and extrapolation to the model boundaries. The same process is conducted for temperature data with temperature logs being directly imported into the model software to create points for anisotropic interpolation. Temperature and lithostratigraphic integration demonstrates the geologic controls of isotherm placement through generating model profiles. The MT data can be directly applied to the lithostratigraphic and temperature relationships as indicated by changes in low-to-high resistivity. These data sets comprise the conceptual model.

The interpretations of the geothermal system through this conceptual model are not without limitations. The spatial extent of the data gathered at the site was greatly limited by access on stable ground and existing trails. This includes the MT stations placed around the site that had to avoid flooded fields and permafrost, suitable ground for drill pad placement for the drilling locations of the deep wells, and general road/trail access for vehicle and heavy equipment. The largest constraint of the conceptual model is the lack of deep well lithostratigraphic and temperature data outside of the NE-SW lineated density of wells on site. The density of the well data, both Geoprobe and deep well, is greatest in the middle of the model which inherently produces biases on the consideration of various scenarios on the transport of hydrothermal fluids in the subsurface. However, no compelling evidence has been discovered as of yet that would justify drilling deeper wells outside of this trend on the hot springs site.

The conceptual model is complemented by the numerical model which evaluates the temperature and fluid flow conditions at Pilgrim Hot Springs for the purposes of testing the total energy flux estimation and deeper reservoir location. The sediment descriptions and lithostratigraphic architecture presented in this conceptual geologic model have been incorporated into the numerical model to provide permeability calculations for a more effective fluid flow model.

5.2 Discussion of the Conceptual Model

In general, the Pilgrim geothermal system can be subdivided into a shallow outflow aquifer and a deeper reservoir beneath a clay cap connected by a very narrow conduit with 91 °C upflow (Figure 5.1). Temperature logs increase to 91 °C at 25-50 m with a reversal at 30-100 m. The isotherm distribution is visually interpreted from temperature logs (Figure 5.1). The peak in temperature is the result of the outflow of geothermal fluids and the increasing temperature gradient is due to the heating of the deeper geothermal reservoir. The outflow direction is mostly concentrated to southwest and northeast. All wells show an increasing temperature gradient below the reversal with differing rates. The temperature gradients suggest the upflow is located between PS-12-1, PS-12-2, and PS-12-3. Stratigraphic correlations based upon well log data indicate several clay layers throughout the section with a dominant clay horizon at 200-300 m depth. Induration in the sediments is mostly concentrated between wells PS-4 and PS-12-3 and occurs from basement to the shallow subsurface with a chimney-like shape.

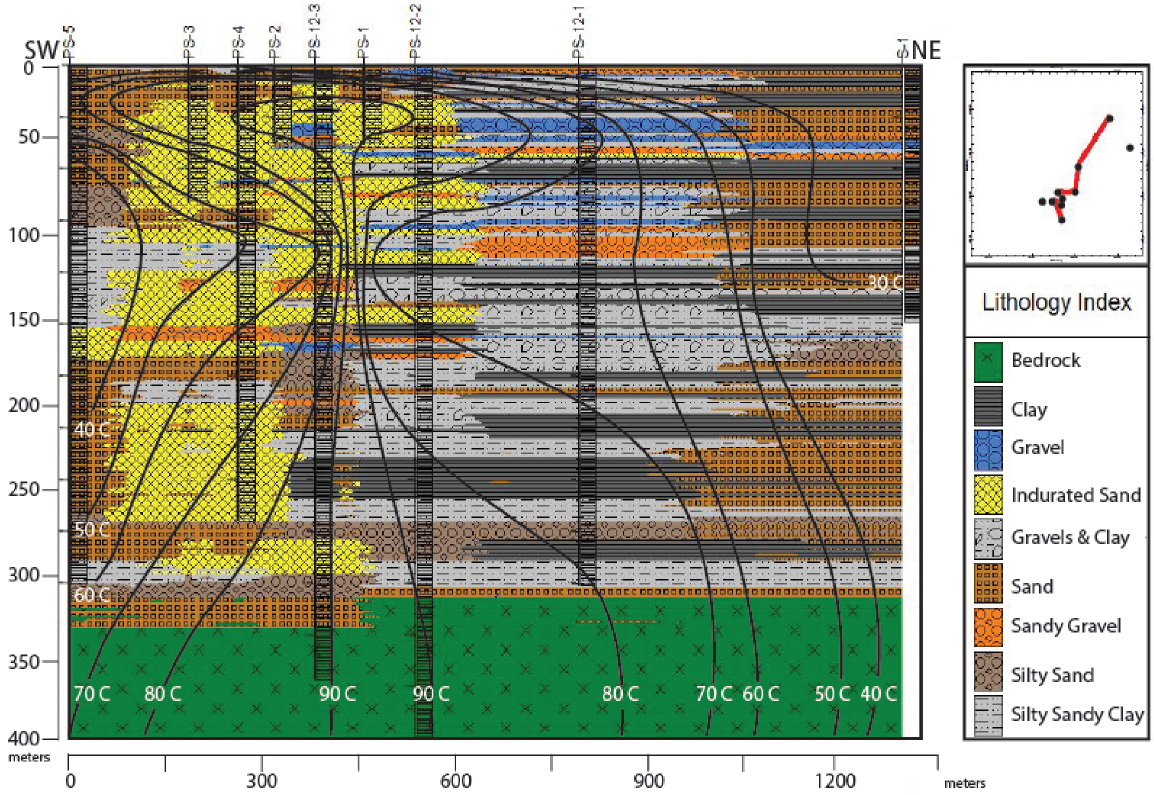

Figure 5.1: Stratigraphic cross-section of the geologic model with isotherms. Temperature isotherms are derived from the temperature model and indicate a shallow outflow aquifer above 100 m, a narrow upflow from 100 m to 300 m, and a deeper reservoir connecting to the system in the vicinity of PS-12-2 and PS-12-3.

Regarding the lithostratigraphic and temperature data, the conceptual model contains a data set greatly restricted in the size of inspection area. This is the result of the density of well data occurring in a small area, many as close as 100 m, and along a SW-NE trend. This trend makes confident extrapolation into other areas of the model that lack well data difficult. Inferring the extent of the modeled lithostratigraphic units and isotherms without well data is achieved through the geophysical surveys, notably the MT survey. The combination of MT ground-based resistivity and temperature data may delineate the upflow of hydrothermal fluids from depth. The temperature data of both the deep wells and shallow Geoprobe holes guide the modeled isotherms. However, the MT does not directly image the high-temperature fluids, but rather the associated hydrothermal alteration products in the sediments and bedrock (Cumming, 2009). The spectral investigation of AlOH absorption and estimated smectite content through methylene blue analysis reveal a close relationship of low MT resistivity and hydrothermal alteration (Figure 5.2). This can be used to elucidate the areas of past and present alteration through the interaction with hydrothermal fluids. By these proxies, the location of the upflowing fluids can be inferred.

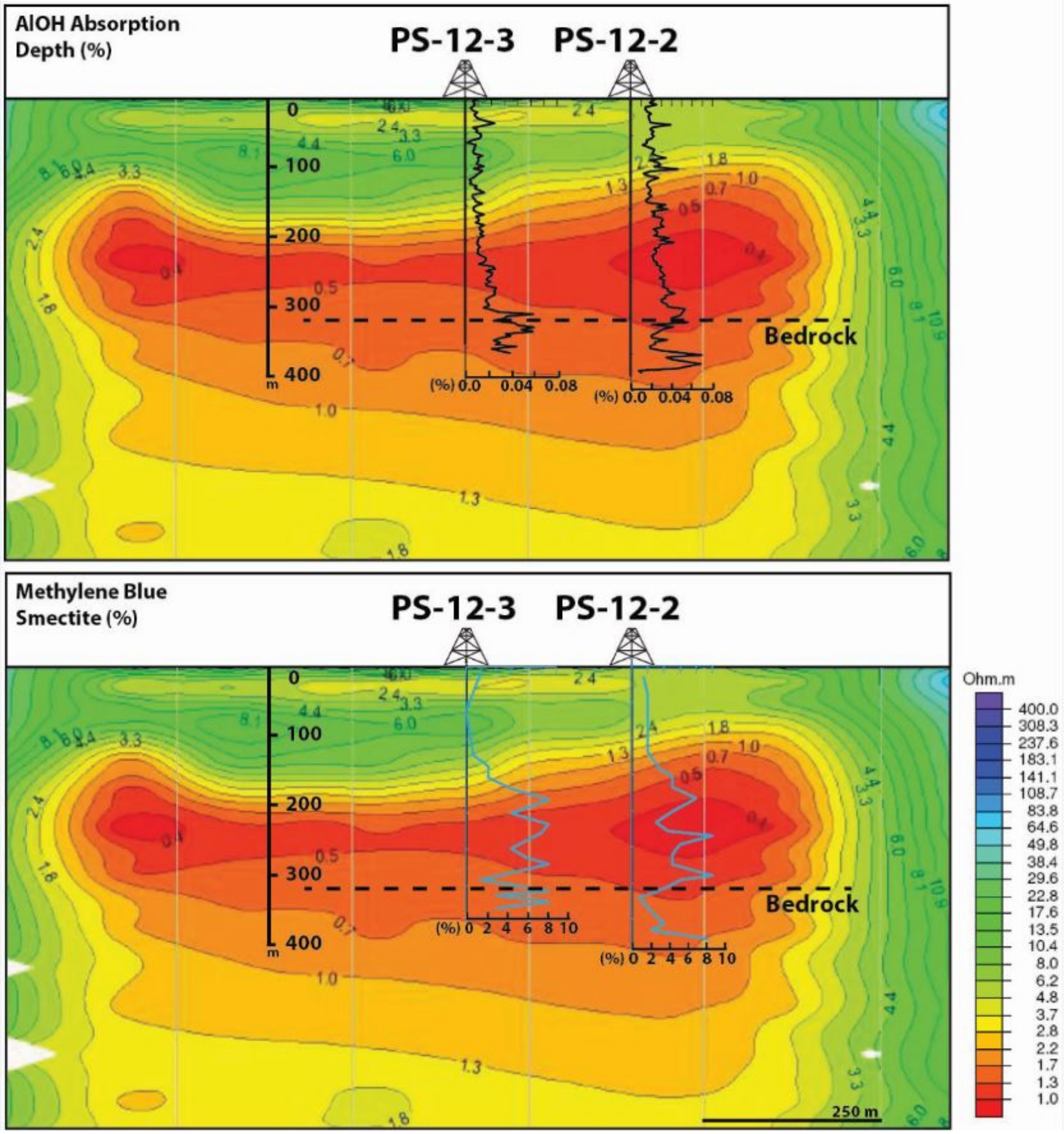

Figure 5.2: AlOH absorption and methylene blue results plotted on MT profile. An example MT resistivity profile is used for comparison to AlOH absorption (top) and methylene blue analysis (bottom). Both methods correspond with an increase in AlOH absorption and estimated smectite content as proxies for hydrothermal alteration in the low resistivity zone. MT data provided by FUGRO (2012).

MT and temperature distribution plan maps are used to highlight the various elements of the geothermal system and demonstrate the extent of associated alteration. The base of the shallow thermal aquifer is located at 50 m depth and shows an area of low resistivity (<3 ohm-m) constrained by >70+ °C isotherms between wells PS-12-1, PS-12-2, and PS-12-3 (Figure 5.3). The conductor is most likely discontinuous altered clay (smectite) layers, common low-temperature (<100 °C) hydrothermal alteration products, as no clay intervals appear laterally continuous through all the wells at this depth. The western and southern resistive zones bordering the hot springs are due to permafrost. With present day temperatures and interpreted alteration in the MT map showing a similar spatial extent, the outflow is apparently discharging hot fluids at this location and depth without much lateral movement or migration from this area through time. Both the 100 m and 200 m MT and temperature maps show similar-sized conductive and high temperature zones, respectively (Figures 5.4-5.5). At 100 m, the hottest temperatures are modeled to occur slightly to the northwest of PS-12-2 while the MT map shows a conductive zone of proportional size to the southeast of the same well. This discrepancy may result from the temperature model prediction of where the high temperatures occur. At this depth, the model is relying on 11 wells as control points for isotherm placement and all wells are displaying a temperature reversal at this depth. The higher temperatures could just as likely be placed at the approximate location of the conductive zone in the MT map. Both maps suggest the conduit feeding the outflow is narrow (<100 m) and difficult to predict as well as resolve through modeling.

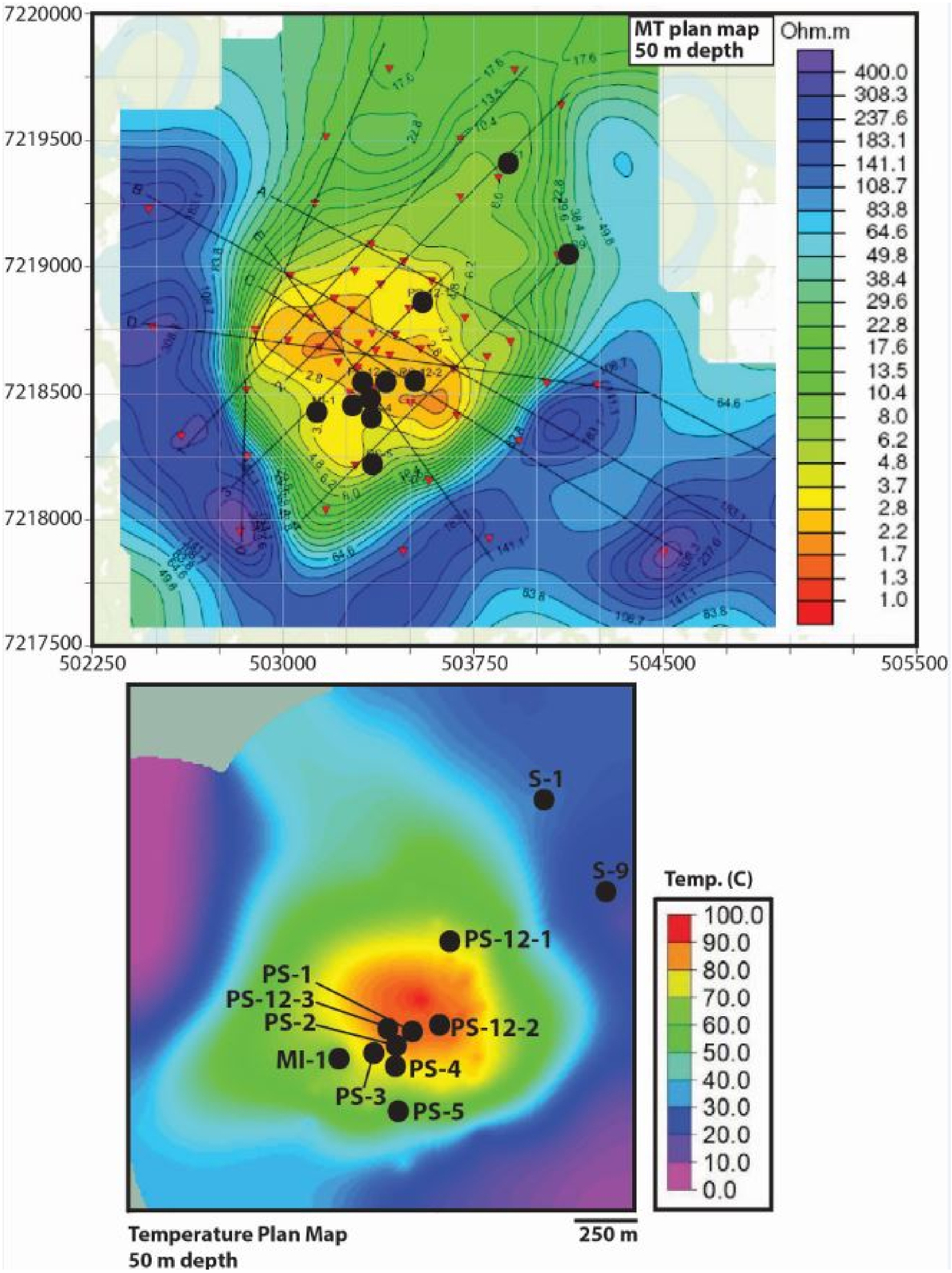

Figure 5.3: MT and RockWorks15 temperature model plan maps at 50 m depth. The red triangles indicate MT station location.

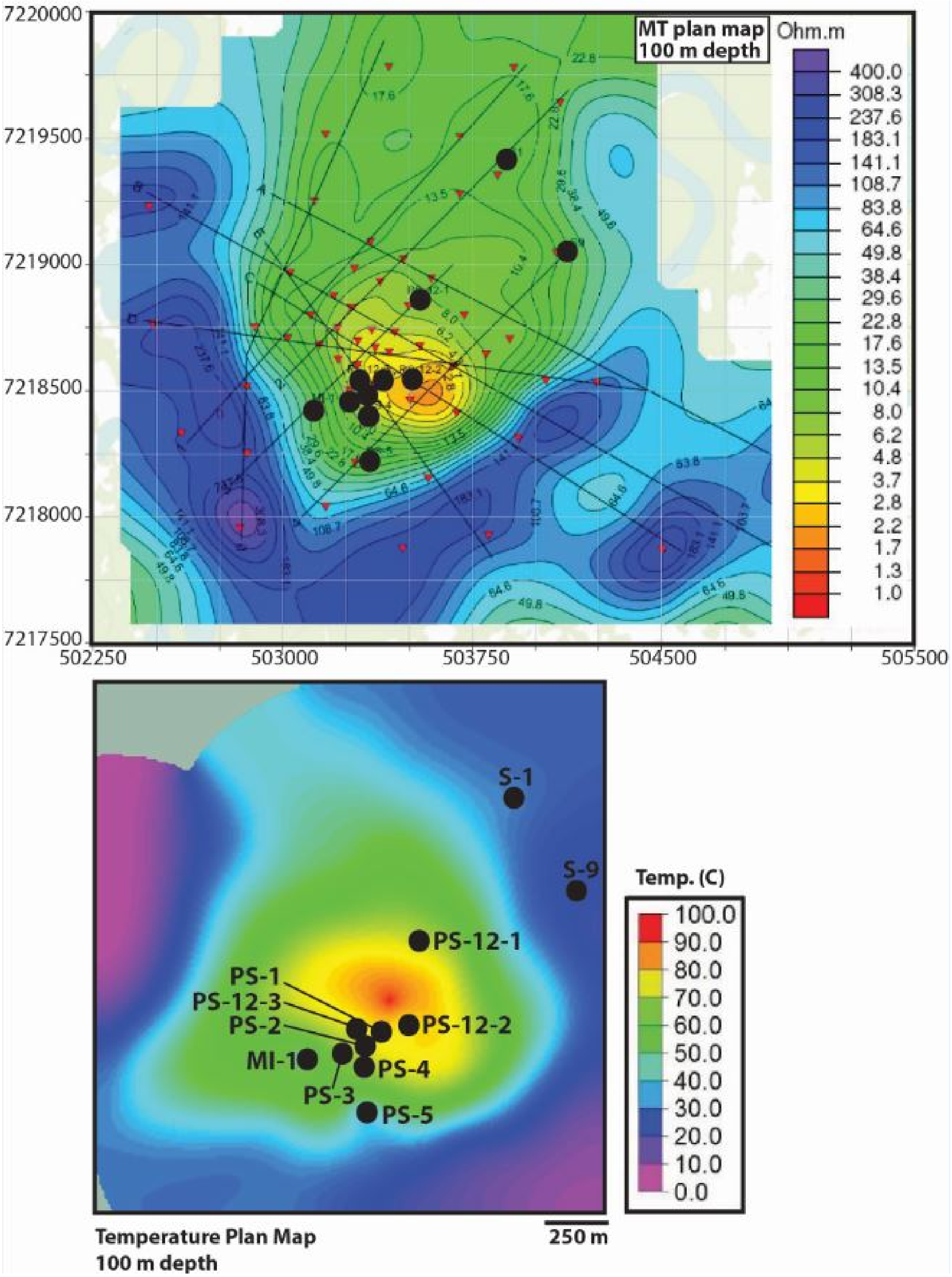

Figure 5.4: MT and RockWorks15 temperature model plan maps at 100 m depth. The red triangles indicate MT station location.

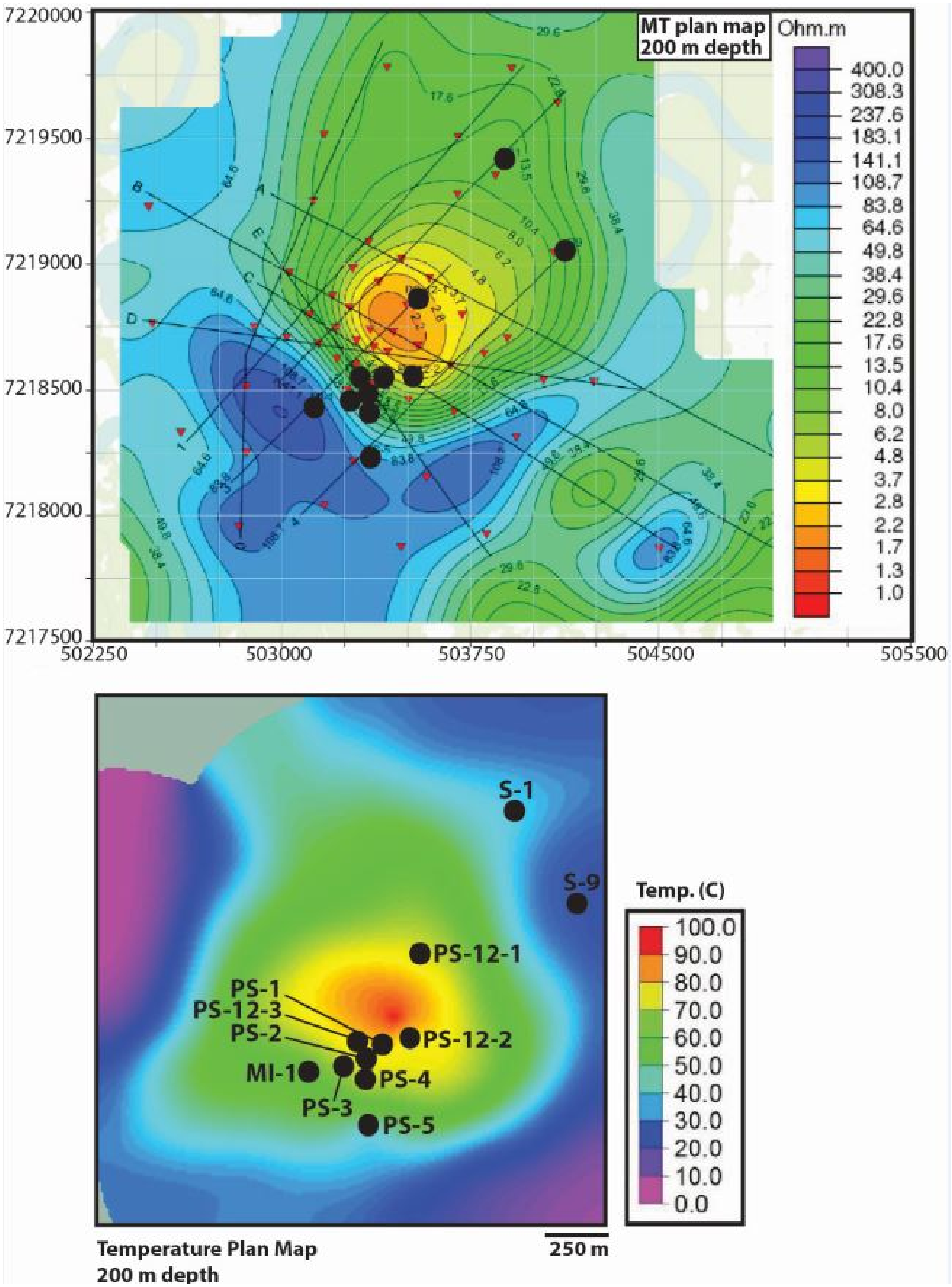

Figure 5.5: MT and RockWorks15 temperature model plan maps at 200 m depth. The red triangles indicate MT station location.

The 200 m depth maps both indicate a broader zone of conductivity and zone of higher temperatures as all the wells show an increasing temperature gradient. The numerous intervals of interbedded clays, sands, and gravels at this depth may be effectively transmitting hydrothermal fluid across the wells, protecting against the colder meteoric water. The 300 m depth maps show a significant difference in interpreted alteration due to high conductivity and the predicted zone of high temperatures. Until this depth, both data sets demonstrate a reliable correlation of alteration and high temperature fluids. However, the MT suggests a zone of increased conductivity in a large area that centers near PS-12-1 and bends back away from wells PS-12-2 and PS-12-3. This is surprising as the temperature map of the same depth indicates a large area of high temperatures centered between these wells with PS-12-2 being the hotter well at 91 °C and PS-12-1 at 80 °C. Both wells display similar values of estimated smectite content and AlOH absorption at this depth, indicating that both have experienced similar degrees of alteration. Also, the mineral assemblage of mixed smectite-illite and kaolinite clays have very similar abundances at this depth in both wells (Appendix B.1-B.3) and form in the active hydrothermal flow regime of fluid circulation (Mas et al., 2006). This means both wells have been subject to nearly the same extent of hydrothermal alteration in the past. However, the MT shows a more conductive signature at PS-12-1 and higher temperatures are centered on PS-12-2. This is interpreted to mean that the conductive signature, associated with smectite clay development, possibly shows a large clay layer extending from PS-12-1 to the north, west, east, and tapers around PS-12-2 and PS-12-3 where the clay abruptly pinches out and hot fluids may migrate up and around its edge. The pinch out is supported by the southwestern wells PS-4 and PS-5 where this interval contains sands and indurated sediments, thus the loss of the conductive signature.

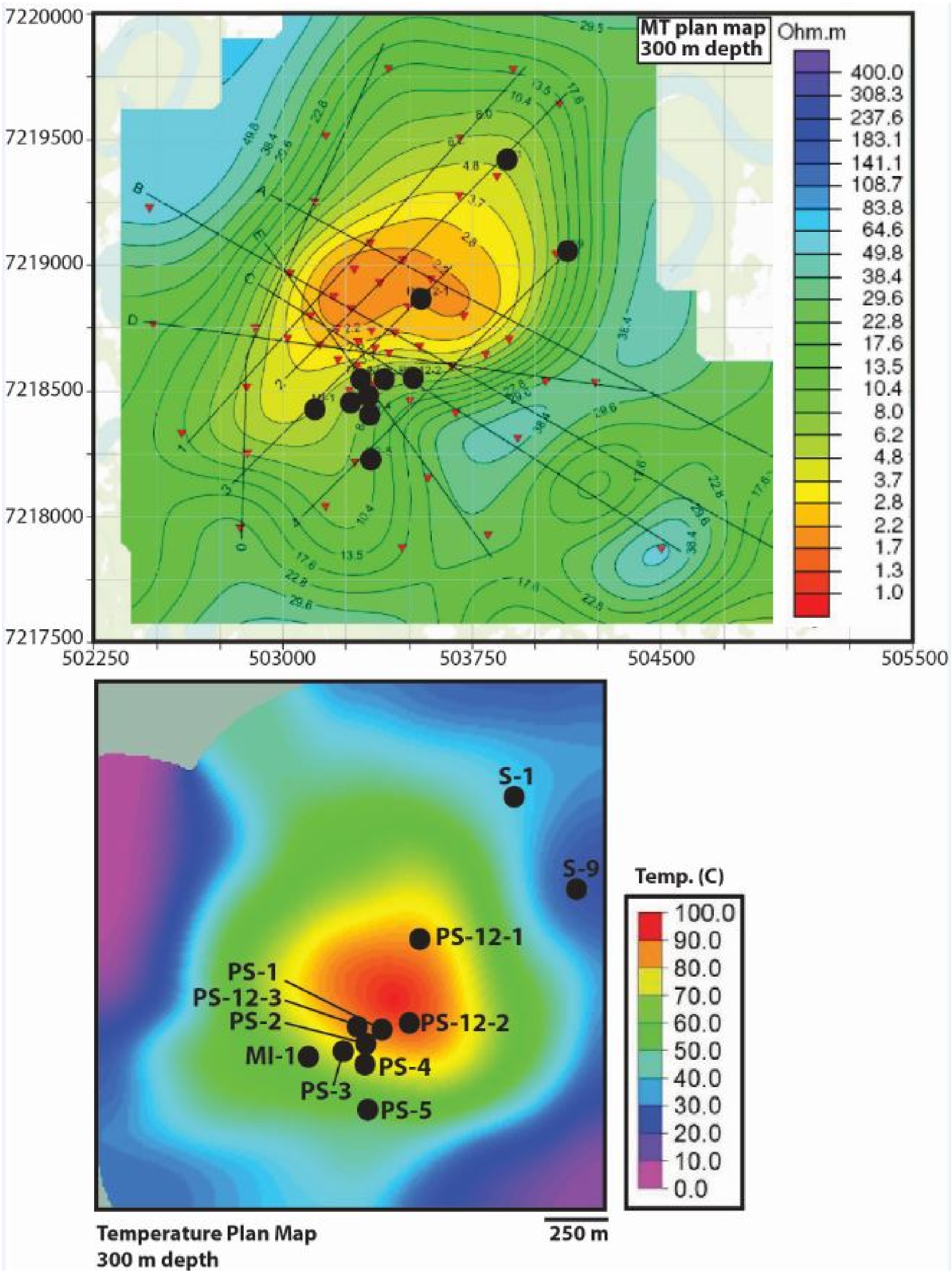

Figure 5.6: MT and RockWorks15 temperature model plan maps at 300 m depth.

The hot fluids are seemingly upwelling from a location closest to PS-12-2 due to the highest bottomhole temperature of 91 °C at the basement-sediment contact. The outflow temperatures in PS-12-2, PS-1, PS-2, PS-3, and PS-12-3 all exhibit 90-91 °C temperatures, meaning rapid and/or insulated transport to the shallow subsurface through a conduit of significant permeability. This interpreted location of the upflow is also supported by the extent of the indurated sediments. The cement of the indurated sand is dominantly composed of silica, as verified by x-ray diffraction analysis (Woodward-Clyde, 1983). All wells (with the exception of S-1 and S-9) show induration down to depths of 150 m (PS-12-1 with a very thin 3 m indurated interval at 60 m), PS-4 with induration to 250 m, and PS-12-3 being indurated to 275 m. PS-12-2 is not indurated at this interval above bedrock, maybe due to size of the sediments. From 300-320 m, PS-12-2 has coarse sand that is more porous than the silty-fine sand where induration occurs. Smaller pore spaces in the finer sediments tend to become cemented through precipitation from super-saturated fluids first whereas larger pore spaces in the coarse sand are often preserved and non-cemented (Cox et al., 2002). With high temperatures centered around PS-12-2 and dense induration occurring close to the bedrock surface in PS-12-3, the upflow is predicted to occur between the two wells from the bedrock fracture and/or fault conduit. This location plots underneath wells PS-1 and PS-2. Although both are shallow wells of only 50 m depth, these wells are very well indurated and PS-2 in particular, "vigorously degassed" at 15 m depth during drilling (Kline, 1980). The composition of the gas was guessed to be CO_2. Liss and Motyka (1994) sampled H_2 in Pilgrim wells and discovered the highest concentrations in PS-1. These gas concentrations may imply close proximity to rapidly upwelling hot fluids where tightly-sealed indurated sediments retain the exsolved gases directly from the fluids. Regardless, considering an estimated diameter of <100 m for the upflow conduit, the best placement of this conduit appears to between PS-12-2 and PS-12-3.

A simple conceptual model of MT profiles and isotherms is shown in Figures 5.7-5.8. MT Profile D shows a large, very low resistivity pattern (<1 ohm-m) from 150 m to 400 m that extends into the top of the basement and is sharply bounded by increasingly resistive zones on the west (left) and east (right) (Figure 5.7). Areas of high resistivity values are interpreted as permafrost (0-100 m) and cold regional groundwater influx. The <0.5 ohm-m zone matches very closely to the modeled stratigraphy of the thick clays from 200-275 m in wells PS-12-2 and PS-12-3 (Figure 5.8). The clay interval is a mixed layer clay and resembles a low permeability, low resistivity clay cap to a geothermal reservoir underneath (Cumming, 2009). A shallow, flat, low resistivity layer of 2.4 ohm-m at 50 m depth aligns with the indurated zone in MI-1 and PS-12-1 (Figure 5.8). A deep conductor at ~800 m depth appears in Figure 5.8 as marked by the blue box. This is an artifact of the 3D MT modeling algorithm that projects the conductor into infinite size beyond the spatial boundaries of the survey data range. Above the blue box is a strongly conductive zone beneath MI-1 and stretches to PS-5 in other MT cross-sections. This zone could be the result of smectite clay development in the bedrock through hydrothermal fluid flow contact or localized heterogeneity in the mica schist bedrock. Turner et al. (1979) mapped local graphitic schist in the bedrock exposures in the Kigluaik Mountains. If graphite is present in the bedrock beneath Pilgrim, it would result in a very conductive signature and would transmit fluids very efficiently due to its mineral structure (Cumming, 2012). Both interpretations are inherently difficult to prove or disprove with the lack of bedrock drilling on the western edge of the hot springs site. However, PS-5 has a bottomhole temperature of <50 °C just 50 m above the bedrock surface. This makes extensive smectite development in the shallow bedrock seem unlikely. In the event that it is smectite from past alteration, the clay is likely plugging fractures or faults and mitigating vertical flow to a point of entry into the sediments closer to the center of the hot springs area. This is incorporated into the cross-sections as lateral splays of decompressing heated fluids exiting the bedrock fractures shown as kinks in the isotherms at the bedrock surface.

Groundwater flows from the resistive western and eastern boundaries into the system where it eventually mixes with the outflow. A blue resistive zone under MI-1 shows how the cold water enters the system from the south and west from under the permafrost (Figure 5.8). Realistically, the flow is generally directed into the cross-section and continues to the north towards the Pilgrim River. The thermally-buoyant outflow emanates out from the top of the 91 °C plume with a stronger flow to the west and southwest above the influx. Isotherm placement is based on the distribution of temperatures from the wells. The tightly-spaced isotherms of 90-60 °C indicate low permeability correlating to clay layers and indurated sediments (Cumming, 2009) (Figure 5.7). Similarly, the close 30-80 °C isotherms converge at the top of the clay cap of the geothermal reservoir. A deeper heat source of 100+ °C has been placed under the

PS-12-2, although the exact depth and location is hypothetical and only corresponds with the dip of the low resistive zone into the bedrock.

The conceptual model proposes a shallow outflow aquifer in the indurated sediments with a thin clay cap at 50 m depth. The upflow has been placed between PS-12-2 and PS-12-3, although it is very narrow (<100 m) and the exact location is uncertain. A small convection cycle may feed into the influx of cold water where cooler outflowing fluid mixes with the meteoric water. The upflow of the 91 °C geothermal fluids is a vertical conduit from basement to outflow and is constrained by the low permeability indurated sediments. The upflow also correlates well with the indurated zone possibly due to the porosity and permeability of the cemented sand that acts as a reservoir for geothermal fluids and can vertically transmit fluid with less heat loss than unconsolidated sediments. When contemplating future drilling targets, drilling between PS-12-2 and PS-12-3, close to PS-1, is the most promising location. Both the MT and temperature maps suggest lower temperatures any direction more than 500 m outside of the area from MI-1 to PS-12-1. This is evidenced by colder Geoprobe hole data and an increase in resistivity.

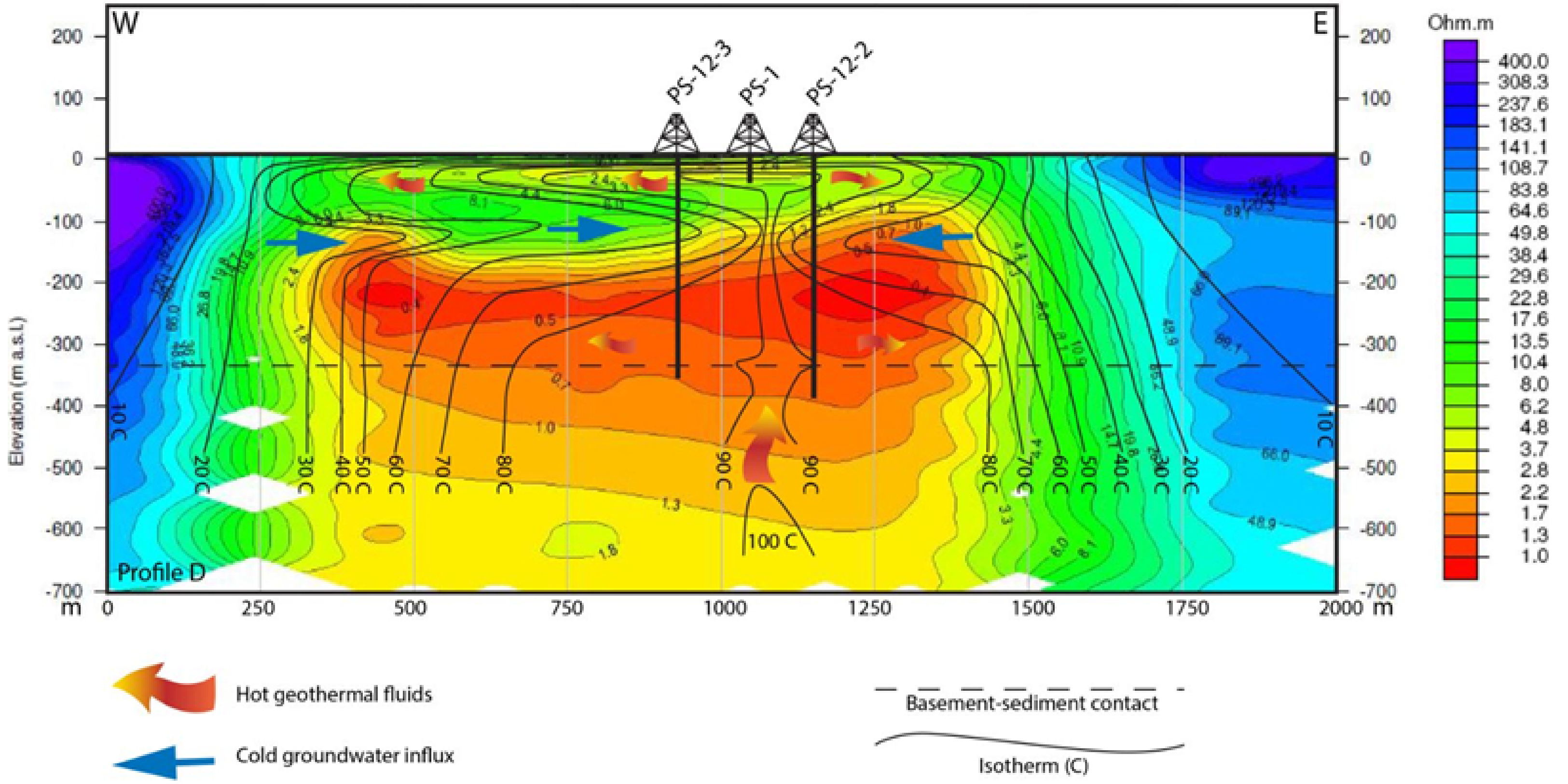

Figure 5.7: Simple conceptual model cross-section utilizing the W-E Profile D of the MT survey. Isotherms are plotted from 10-100 °C with hot fluid and cold fluid arrows to indicate direction of flow. Bedrock-sediment contact has been dashed to indicate approximate extent.

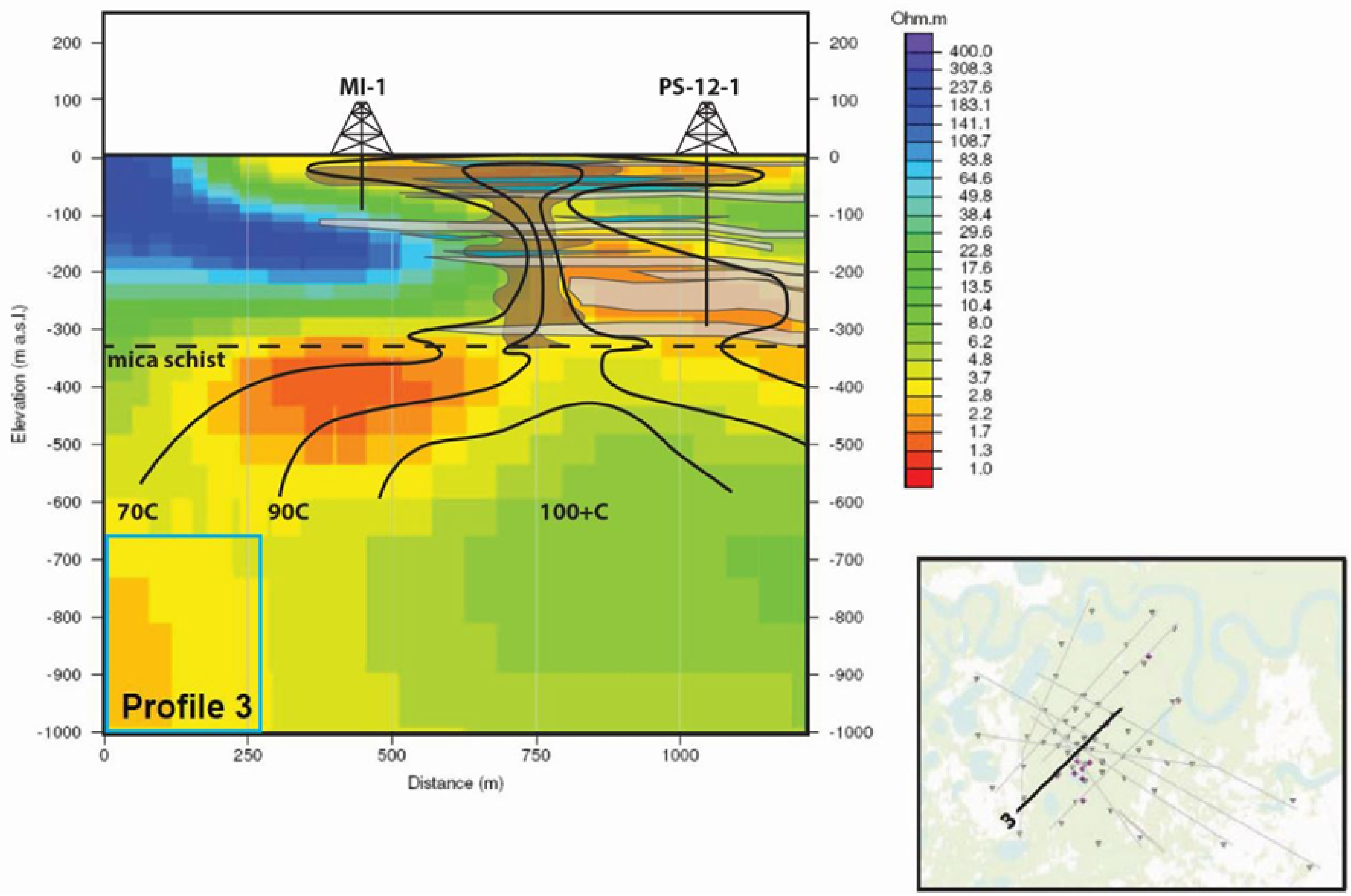

Figure 5.8: 3D MT Profile 3 overlaid with lithostratigraphy. Clay is gray, gravels are blue, and the induration is shaded in brown. SW is left and NE is right. MT data provided by FUGRO (2012).

As indicated in the broader, yet more shallowly focused electromagnetic survey, the conductive signature of the geothermal system at Pilgrim shows a narrow extent west-east and a larger extent north-south marked by the red boxes (Figure 5.9). The extent of the geothermal system is inferred from the occurrence of permafrost at the system's boundaries. With resolution only to 100 m depth, the shallow conductive response from outflowing hydrothermal fluids discharging into the groundwater and river extends as much as 4 km to the north at the base of Hen and Chicken Mountain. The conductive signal could be the result of the increased salinity of the northern directed regional groundwater flow mixing with the geothermal fluids which would make the system appear much larger in the north-south cross-section. Geoprobe shallow temperature surveying and an MT survey could be used to evaluate the conductive response, specifically to the northeast where Turner and Forbes (1980) identified a small thermal expression at the base of Hen and Chicken Mountain.

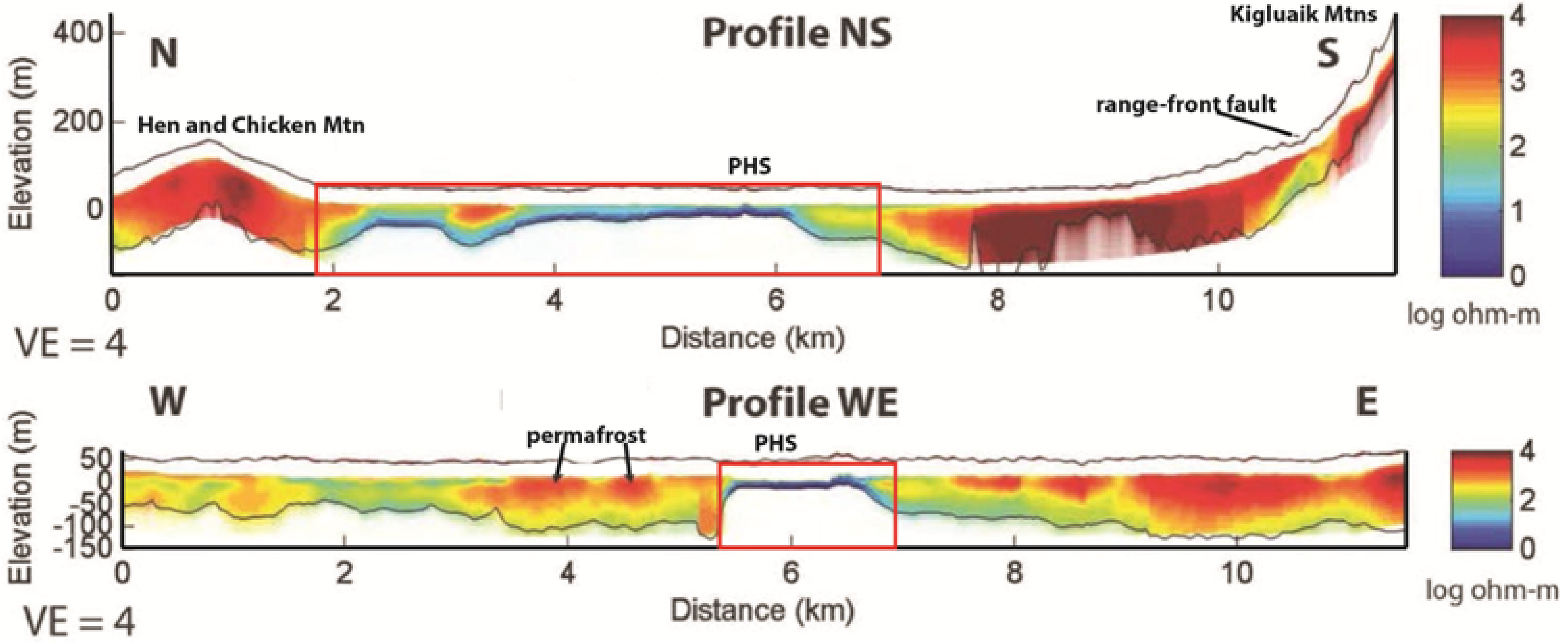

Figure 5.9: USGS airborne electromagnetic resistivity survey of the Pilgrim River Valley surrounding the hot springs area (McPhee and Glen, 2012).

5.3 Conceptual Model in a Regional Context

When considering the structural style and sedimentary architecture of the Pilgrim River valley alluvial basin with limited subsurface lithologic data, comparison to analogue basins can provide context for discerning the basin morphology. The Basin and Range geologic province in the Western U.S. contains many low-temperature geothermal systems that exhibit similar characteristics to Pilgrim. The structural controls on many Basin and Range systems are large normal faults commonly with step-overs, fault intersections, and terminations (Cashman et al., 2012). Heat for the geothermal systems is derived from deep circulation along the major fault systems (Blackwell and Kelley, 1994). Models for rift valley and asymmetric alluvial basin stratigraphy commonly include wide aprons of coarse-grained sand to gravel alluvium along the range faults and less extensive finer sediment fill in the center at the distal edges of the alluvial fans (Blackwell and Kelley, 1994; Bosworth and Morley, 1994; Okaya and Thompson, 1985). Lacustrine and floodplain clays, deposited during periods of subsidence in active extension, act as low permeability aquicludes that promote heat retention in the migrating hydrothermal fluids. The coarse-grained alluvial gravels form thick wedges along the deeper portions of the basin and thin distally (Blackwell and Kelley, 1994). These gravels allow mixing with groundwater or cross-range flow and typically exhibit depressed isotherms where heat loss is greatest (Blackwell and Kelley, 1994). Low permeability sediments are necessary for shallow geothermal systems to exist in alluvial basins because they facilitate heat conduction from upflowing fluids (Blackwell and Kelley, 1994).

The facies model examples mentioned above of asymmetric alluvial basin stratigraphy guided the understanding of the Pilgrim River Valley basin in the context of the geophysical survey results and field observations. Figure 5.10 shows the idealized cross-section of overlapped isostatic gravity, ground magnetic, and aeromagnetic resistivity data with fault orientations drawn to scale to illustrate the basin. The ground magnetic line shows an anomalously low value while the isostatic gravity dips in response to a relative increase in gravity. Low values in the ground electromagnetic survey possibly indicate hydrothermal fluid flow zones that reduce the magnetization of the bedrock (Schwering and Karlin, 2012). The Pilgrim Hot Springs conceptual model is placed in the context of this figure.

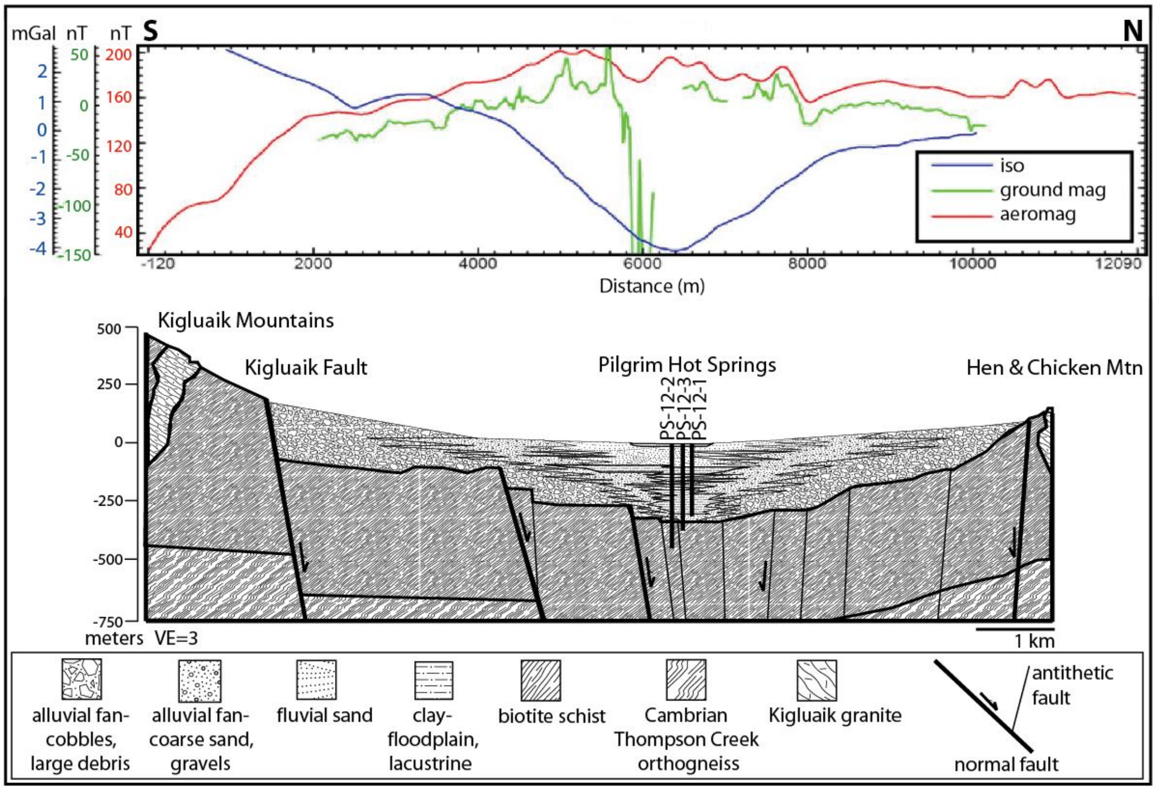

Figure 5.10: Interpreted basin cross-section of the Pilgrim River Valley. Interpreted from isostatic gravity (iso), ground magnetic (ground mag), aeromagnetic (aeromag), and drilling data as well as measured strikes and dips of fault planes that intersect the surface. The cross-section is south to north (left to right). Survey data provided by Jonathan Glen.

In a larger context, Pilgrim Hot Springs may be located in an area of significantly deep and numerous fractures and faults in the underlying graben. Miller et al. (1975) concluded from a regional aeromagnetic survey conducted in 1972 that the springs may be fed from an east-west trending conductive fault extending from the Bendeleben fault into the vicinity of Pilgrim Hot Springs. This was also previously proposed by Sainsbury et al. (1969). The bedrock and surficial geologic map, however, has a major ~N-S directed fault projected across the basin that transects the western edge of the thawed ground at Pilgrim (Turner et al., 1979). The fault is placed here due to a ~1 m terrace that runs roughly in the same direction. The terrace is most likely the result of frost-heaving in the active layer of the permafrost where frozen soils expand, causing an uplift in the immediate subsurface, as it forms an arc around the thawed ground anomaly. Both the Bendeleben and Kigluaik Mountains are bounded on the south and north respectively by range-front normal faults with opposite directions of dip (Figure 5.11). The convergence of these two faults can be explained by a transfer fault to accommodate the change in dip (McDannell, 2011). A series of offsets occur in the lithologic contacts south of the location of the proposed transfer fault (Figure 5.11). These offsets display movement consistent with the motion of the transfer fault orientation (Figure 5.11). The en echelelon-style step-overs of the Kigluaik range-front fault may be the result of movement along the transfer fault. The significance of this inferred fault may suggest locally deep faulting and intense fracturing of the bedrock which may be hydraulically conducive to deeply circulating hydrothermal fluids. However, any number of smaller fault splays from this transfer fault could be feeding directly into the hot springs and this fault by itself is not a likely target for deep drilling. The fault could also be a remnant of older tectonism that resolved the difference in stress direction of the surrounding faults and is no longer active or conductive. Regardless, it is likely the mica schist bedrock below Pilgrim Hot Springs is significantly fractured and may explain the location of the hot springs and its connection to a deeper heat source.

The highly speculative heat source has been investigated by numerous researchers and at present, no single heat source has been identified (Liss and Motyka, 1994; Miller et al., 1975; Turner and Forbes, 1980; Woodward-Clyde, 1983). Liss and Motyka (1994) posit the source has a mantle component. This is based on gas chemistry of helium 3/4 isotope values of 0.9 that are well below volcanic origin, but elevated for a crustal source (Liss and Motyka, 1994). They favor a deep circulation origin of the heated fluids. Miller et al. (1975) mention that although Seward Peninsula has experienced geologically recent volcanic activity, no hot springs or any thermal expressions have been discovered in or around the basaltic or intermediate volcanic rocks. Evoking a magmatic source for Pilgrim related to the young volcanism must explain why no fumeroles or any other related-geothermal systems presently exist in those areas. Miller et al. (1975) conclude that the saline and nonsaline fluids sampled in Seward Peninsula geothermal systems resemble deeply circulating meteoric fluids based on preliminary chemical and isotopic data. These fluids may still be interacting with different heat sources such as radiogenic plutons at depth. However, evidence suggests these fluids have a strong component of deep-circulation through large fault systems and fracture networks as well.

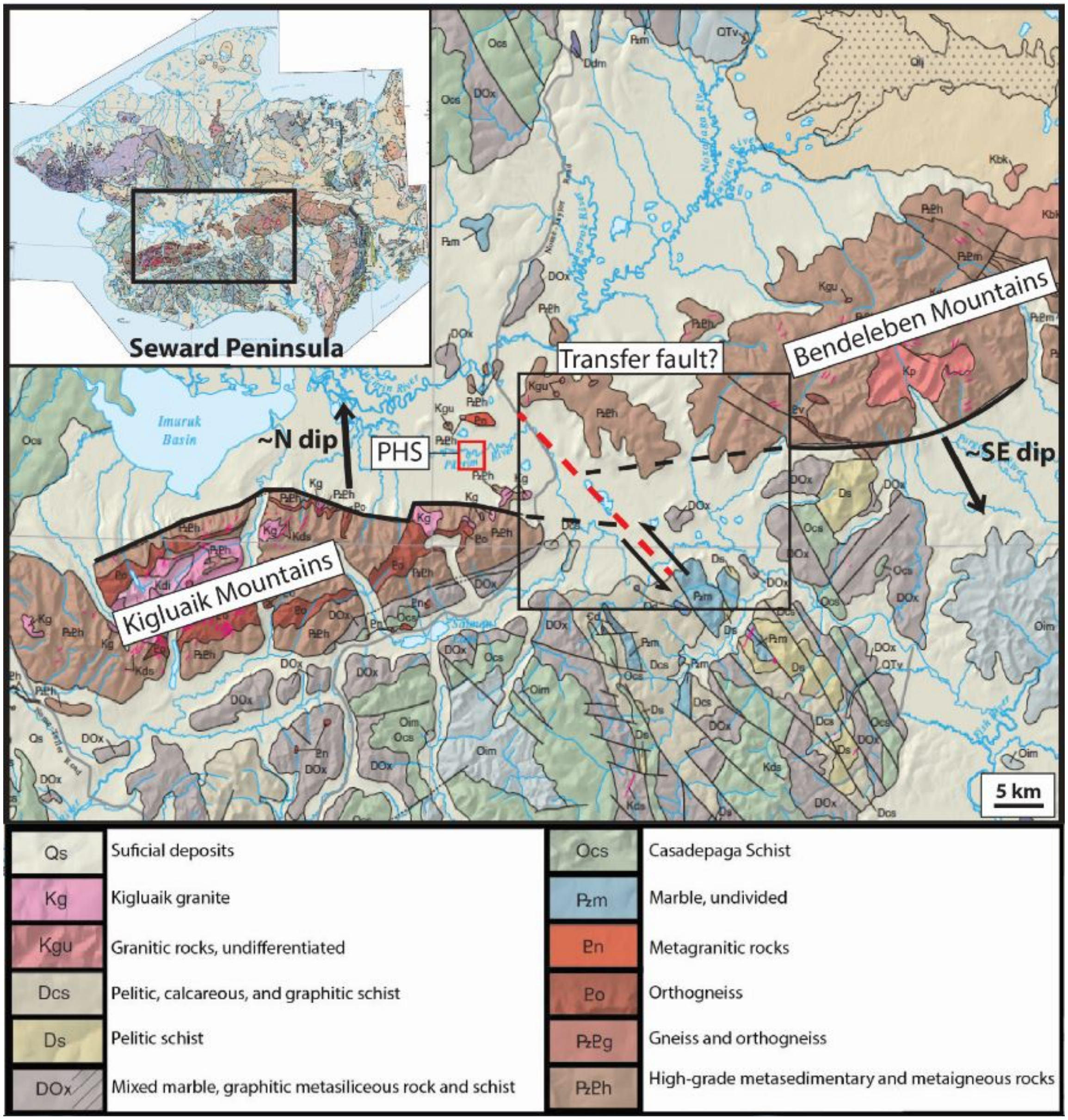

Figure 5.11: Location map of the inferred transfer fault. Map modified from Till et al. (2011).

Chapter 6: Conclusions and Recommendations

6.1 Conclusions

A conceptual model is presented to demonstrate the lithostratigraphic architecture as a control on the fluid migration pathways of the Pilgrim Hot Springs geothermal system. Results of the conceptual model show the geothermal system is comprised of Quaternary sediments down to 320 m depth that overlie a mica-schist basement. Based on temperature, geophysical well logs, MT survey, and lithologic data, the system can be subdivided into a shallow outflow aquifer and a deeper bedrock reservoir beneath a clay cap connected by a very narrow, <100 m wide, conduit with 91 °C upflow. The temperature gradients suggest the upflow is located between PS-12-2 and PS-12-3. Lithostratigraphic correlations based upon well log data indicate several clay layers throughout the section with significant clay horizons at 100 and 200-300 m depth. These clay layers act as major hydraulic barriers to vertical fluid migration and mitigate horizontal flow of geothermal fluids and regional groundwater. Magnetotelluric resistivity data matches closely to the modeled stratigraphy where thick clays from 200-300 m in wells PS-12-1, PS-12-2, and PS-12-3 correlate to the <0.5 ohm-m zone in the MT cross-sections. Reflectance spectroscopy and methylene blue titration detect highly conductive smectite clays in this zone as well as illite and kaolinite. Induration in the sediments is mostly concentrated between wells PS-4 and PS-12-3 and occurs from the shallow subsurface to the basement surface. The indurated sediments may also facilitate hydrothermal fluid flow by insulating higher permeability coarse sand and gravels.

Potential production from this resource is limited to where sufficient permeability exists in connection to the upflow. The silty sands beneath the clay layer at ~300 m close to PS-12-2 could have a high enough temperature and flow to be a feasible target for a large diameter production well. Additionally, extensive pyritization and a hydrothermal alteration clay mineral assemblage suggest an argillic-style alteration facies. This points to past temperatures at or slightly elevated above current conditions of hydrothermal activity at Pilgrim Hot Springs. The conceptual model supports production from this resource in those subsurface zones where there is sufficient permeability and connectivity with the upflow zone.

6.2 Recommendations

Further evaluation of the site is required to produce the upflow source from the bedrock fault or fracture network feeding the hot springs. A deep seismic survey would provide critically needed information for depth to bedrock changes across the basin as well as identify major structural features of the bedrock. If a large transfer fault is located nearby, seismic surveying would be needed to delineate zones of increased fracturing or faulting that may be directing upwelling hydrothermal fluids. Geoprobe shallow temperature surveying and a smaller, more targeted MT survey of the thermal expression at the base of Hen and Chicken Mountain would also be beneficial in understanding the deeper bedrock reservoir. If these two sites are connected by the same conduit, this may imply that Pilgrim Hot Springs is a surface expression of a much larger reservoir at depth.

The next step in assessing the Pilgrim Hot Springs geothermal resource is the integration of new drilling data to test the interpretations of the current conceptual model. The zone of high permeability coarse sands above the basement surface in connection to the upflow between PS-12-1, PS-12-2, and PS-12-3 is being targeted for drilling. A production well and temperature gradient slimhole wells will be drilled in the fall of 2013. This will serve to increase the accuracy of the predicted framework of the geothermal reservoir and the understanding of the upflow location and trajectory. Success of these efforts will determine the viability of Pilgrim Hot Springs as a resource with electric power production capability.

References

Amato, J. M., Wright, J. E., Gans, P. B., Miller, E. L., 1994. Magmatically induced metamorphism and deformation in the Kigluaik gneiss dome, Seward Peninsula, Alaska, Tectonics, 13, 2, 515-27.

Amato, J. M., Miller, E. L., 2004. Geologic map and summary of the evolution of the Kigluaik Mountains gneiss dome, Seward Peninsula, Alaska, Geological Society of America Special Papers, 380, 295-306.

Amato, J. M., Toro, J., Miller, E. L., Gehrels, G. E., Farmer, G. L., Gottlieb, E. S., Till, A. B., 2009. Late Proterozoic–Paleozoic evolution of the Arctic Alaska–Chukotka terrane based on U-Pb igneous and detrital zircon ages: Implications for Neoproterozoic paleogeographic reconstructions, Geological Society of America Bulletin, 121(9-10), 1219-1235.

Amato, J. M., Miller, E. L., Hannula, K. A., 2002. Orthogonal flow directions in extending continental crust: An example from the Kigluaik gneiss dome, Seward Peninsula, Alaska, Geological Society of America Special Papers, 360, 133-146.

Amato, J. M., Miller, E. L., Wright, J. E., McIntosh, W. C., 2003. Dike swarms on Seward Peninsula, Alaska, and their implications for the kinematics of Cretaceous extension in the Bering Strait region, Canadian Journal of Earth Sciences, 40, 6, 865-886.

Bain, D. C., Smith, B. F. L., Wilson, M.J., 1987. A handbook of determinative methods in clay mineralogy, Blackie, London, 1-248.

Barclay, D. J., Wiles, G. C., Calkin, P. E., 2009. Holocene glacier fluctuations in Alaska, Quaternary Science Reviews, 28, 21, 2034-2048.

Bear, J., 1972. Dynamics of fluids in porous media, American Elsevier, 765 p.

Beard, D. C., Weyl, P. K., 1973. Influence of texture on porosity and permeability of unconsolidated sand, AAPG Bulletin, 57, 2, 349-369.

Beget, J. E., Hopkins, D. M., Charron, S. D., 1996. The largest known maars on earth, Seward Peninsula, northwest Alaska, Arctic, 49, 1, 62-69.

Biswas, N.N., Pujol, J., Tytgat, G., Dean, K., 1986. Synthesis of seismicity studies for western Alaska, Tectnophysics, 131, 369-392.

Biswas, N. N., Tytgat, G., 1988. Intraplate seismicity in Alaska, Seismological Research Letters, 59, 4, 227-233.

Blackwell, D. D., Kelley, S., 1994. Implications of facies models on geothermal systems in the Basin and Range province, Geothermal Resources Council Transactions, 18, 3-5.

Bosworth, W., Morley, C.K., 1994. Structural and stratigraphic evolution of the Anza rift, Kenya, Tectonophysics, 236, 93-115.

Brigham-Grette, J., 2001. New perspectives on Beringian Quaternary paleogeography, stratigraphy, and glacial history, Quaternary Science Reviews, 20, (1–3), 15–24.

Browne, P.R.L., 1978. Hydrothermal alteration in active geothermal fields, Annual Review Earth Planetary Science, 6, 229-250.

Bundschuh, J., Suarez Arriaga, M.C., 2010. Introduction to the numerical modeling of groundwater and geothermal systems, fundamentals of mass, energy, and solute transport in poroelastic rocks, Multiphysics Modeling, vol. 2, Taylor & Francis Group, London, UK, 479 p.

Calkin, P. E., Kaufman, D. S., Przybyl, B. J., Whitford, W. B., Peck, B. J., 1998. Glacier regimes, periglacial landforms, and Holocene climate change in the Kigluaik Mountains, Seward Peninsula, Alaska, USA, Arctic and Alpine Research, 154-165.

Calvin, W., Lamb, A., Kratt, C., 2010. Rapid characterization of drill core and cutting mineralogy using infrared spectroscopy, Geothermal Resource Council Transactions, 34, 761-764.

Cashman, P. H., Faulds, J. E., Hinz, N. H., 2012. Regional variations in structural controls on geothermal systems in the Great Basin, Geothermal Resources Council Transactions, 36, 25-30.

Chittambakkam, A. Daanen, R. P., Haselwimmer, C., Prakash, A., Holdmann, G., 2013. Development of a reservoir stimulation model at Pilgrim Hot Springs, Alaska using Tough2, Proceedings, Thirty-eighth Workshop on Geothermal Reservoir Engineering, Stanford University, Stanford, California, SGP-TR-198.

Clark, R.N., Roush, T.L., 1984. Quantitative analysis techniques for remote sensing applications, Journal of Geophysical Research: Solid Earth, 89, 6329-6340.

Clark, R.N., Swayze, G.A., Wise, R., Livo, E., Hoefen, T., Kokaly, R., Sutley, S.J., 2007. USGS digital spectral library splib06a: U.S. Geological Survey, Digital Data Series 231.

Cox, M., Preda, M., Harbison, J., 2002. Importance of indurated sand layers to groundwater flow in Quaternary coastal settings, Moreton Bay, Balancing the Groundwater Budget, Proceedings of the 7th IAH National Groundwater Conference, Darwin.

Cross, R. S., Freymueller, J. T., 2008. Evidence for and implications of a Bering plate based on geodetic measurements from the Aleutians and western Alaska, Journal of Geophysical Research, 113.

Cumming, W., 2009. Geothermal resource conceptual models using surface exploration data, Proceedings, Thirty-Fourth Workshop on Geothermal Reservoir Engineering Stanford University, SGP-TR-18.

Cumming, W. 2012. Personal communication on MT inversion modeling and lithostratigraphic-temperature comparisons.

Daanen, R. P., Chittambakkam, A., Haselwimmer, C., Prakash, A., Mager, M., Holdmann, G., 2012. Use of COMSOL multiphysics to develop a shallow preliminary conceptual model for geothermal exploration at Pilgrim Hot Springs, Alaska, Geothermal Resource Council Transactions, 36, 631-635.

Dumitru, T.A., Miller, E.L., O'Sullivan, P.B., Amato, J.M., Hannula, K.A., Calvert, A.T., Gans, P.B., 1995. Cretaceous to recent extension in the Bering Strait region, Alaska, Tectonics, 14, 549-563.

Finzel, E. S., Flesch, L. M., Ridgway, K. D., 2011. Kinematics of a diffuse North America–Pacific–Bering plate boundary in Alaska and western Canada, Geology, 39, 9, 835-838.

Fitts, C. R., 2002. Groundwater science, Academic Press, An Imprint of Elsevier Science, London, England.

FUGRO, 2012, Pilgrim Springs-Alaska magnetotelluric (MT) survey final report for University of Alaska Fairbanks.

Fujita, K., Mackey, K. G., McCaleb, R. C., Gunbina, L.V., Kovalev, V. N., Imaev, V. S., Smirnov, V. N., 2002. Seismicity of Chukotka, northeastern Russia, in Miller, E.L., et al. eds., Tectonic evolution of the Bering Shelf-Chukchi Sea-Arctic margin and adjacent landmasses: Geological Society of America Special Paper 360, 259-272.

Glassley, W. E., 2010. Geothermal Energy: Renewable Energy and the Environment, Taylor & Francis US, 320 p.

Guilbert, J.M., Park, Jr., C.F., 1986. The geology of ore deposits, WH Freeman, 985 p.

Gunderson, R., Cumming, W., Astra, D., Harvey, C., 2000. Analysis of smectite clays in geothermal drill cuttings by the methylene blue method for well site geothermometry and resistivity sounding correlation, Proceedings, World Geothermal Congress, Kyushu-Tohoku, Japan, 1175-1181.

Haest, M., Cudahy, T., Laukamp, C., Gregory, S., 2012. Quantitative mineralogy from infrared spectroscopic data. I. Validation of mineral abundance and composition scripts at the Rocklea Channel iron deposit in Western Australia, Economic Geology, 107, 209-228.

Harraden, C.L., McNulty, B.A., Gregory, M.J., Lang, J.R., 2013. Shortwave infrared spectral analysis of hydrothermal alteration associated with the pebble porphyry copper-gold-molybdenum deposit, Iliamma, Alaska, Economic Geologist, 108, 483-494.

Harvey, C., 1993. Simplified methylene blue test for estimation of swelling clays, GNS Science, Annotated by W. Cumming, 2004 and 2010.

Harvey, C., Browne, P., 2000. Mixed-layer clays in geothermal systems and their effectiveness as mineral geothermometers, Proceedings World Geothermal Congress 2000, Kyushu-Tokoku, Japan, 1201-1205.

Haselwimmer, C., Prakash, A., Holdmann, G., 2011. Geothermal exploration in Pilgrim, Alaska using airborne thermal infrared remote sensing, Geothermal Resources Council Transactions, 35, 805-810.

Heise, W., Bibby, H. M., Caldwell, T. G., Bannister, S.C., Ogawa, Y., Takakura, S., Uchida, T., 2007. Melt distribution beneath a young continental rift: The Taupo Volcanic Zone, New Zealand, Geophysical Research Letters, 34, 6 p.

Hunt, G. R., 1977. Spectral signatures of particulate minerals in the visible and near infrared, Geophysics, 42, 3, 501-513.

Jennings, S., Thompson, G.R., 1986. Diagenesis of Plio-Pleistocene sediments of the Colorado River Delta, Southern California, Journal of Sedimentary Petrology, 56, 1, 89-98.

Kline, J.T., 1980. Test Drilling Report--Procedures and results of the two test holes drilled at Pilgrim Springs, Alaska in October and November 1979, Alaska Division of Geological and Geophysical Surveys report, 20 p.

Kolker, A.M., Kennedy, B.M., Newberry, R.J., 2008. Evidence for a crustal heat source for low-temperature geothermal systems in the Central Alaskan Hot Springs Belt, Geothermal Resources Council Transactions, 32, 225-230.

Lagat, J., 2007. Hydrothermal alteration mineralogy in geothermal fields with case examples from Olkaria Domes geothermal field, Kenya, United Nations University-Geothermal Training Programme Short Course II on Surface Exploration for Geothermal Resources.

Liss, S.A., Motyka, R.J., 1994. Pilgrim Springs KGRA, Seward Peninsula, Alaska: Assessment of fluid geochemistry, Geothermal Resources Council Transactions, 18, 213-219.

Lofgren, B.E., 1983. Results of drilling, testing, and resource confirmation-geothermal energy development at Pilgrim Hot Springs, Alaska: Unpublished report of Alaska, Woodward-Clyde Consultants to Alaska Division of Energy and Power Development.

Mackey, K. G., Fujita, K., Gunbina, L. V., Kovalev, V. N., Imaev, V. S., Koz'min, B. M., Imaeva, L. P., 1997. Seismicity of the Bering Strait region: Evidence for a Bering block, Geology, 25, 11, 979-982.

Mas, A., Guisseau, D., Mas, P., Beaufort, D., Genter, A., Sanjuan, B., Girard, J.P., 2006. Clay minerals related to hydrothermal activity of the Bouillante geothermal field (Guadeloupe), Journal of Volcanology and Geothermal Research, 158, 380-400.

McDannell, K. T., 2011. Exhumation in the Bendeleben Mountains (Seward Peninsula, Alaska) constrained by (U-Th)/He thermochronology, M.S. Geology thesis, West Virginia University, 46 p.

McPhee, D. K., Glen, J. M., 2012. Airborne geophysical surveys illuminate the geologic and hydrothermal framework of the Pilgrim Spring geothermal area, Alaska, American Geophysical Union Fall Meeting, Sand Francisco, California.

Miller, T. P., Barnes, I., Patton Jr., W.W., 1975. Geologic setting and chemical characteristics of hot springs in west-central Alaska, Journal Research U.S. Geological Survey, 3, 2, 149-162.

Miller, J. K., Prakash, A., Daanen, R. P., Haselwimmer, C., Whalen, M., 2013. Geologic model of the geothermal anomaly at Pilgrim Hot Springs, Seward peninsula, Alaska, 38th Workshop on Geothermal Reservoir Engineering, Stanford University, SGP-TR-198.

Mosser-Ruck, R., Devineau, K., Charpentier, D., Cathelineau, M., 2005. Effects of ethylene glycol saturation protocols on XRD patterns: A critical review and discussion, Clays and Clay Minerals, 53, 6, 631-638.

Okaya, D. A., Thompson, G. A., 1985. Geometry of Cenozoic extensional faulting: Dixie Valley, Nevada, Tectonics, 4, 107-125.

Page, R.A., Biswas, N.N., Lahr, J.C., Pulpan, H., 1991. Seismicity of continental Alaska, in Slemmons, D.B., Engdahl, E.R., Zoback, M.D., Blackwell, D.D., eds., Neotectonics of North America: Boulder, Colorado, Geological Society of America, Decade Map Volume 1.

Page, R. A., Plafker, G., Pulpan, H., 1995. Block rotation in east-central Alaska: A framework for evaluating earthquake potential, Geology, 23, 629-632.

Palacky, G.J., 1988. Resistivity characteristics of geologic targets, Electromagnetic methods in applied geophysics, 3, 53-129.

Ruppert, N. A., 2008. Stress map for Alaska from earthquake focal mechanisms, in Active Tectonics and Seismic Potential of Alaska, Geophys. Monogr. Ser., 179, edited by J. T. Freymueller et al., 351–367.

Sainsbury, C. L., Hudson, T., Kachadoorian, R., Richards, T. R., Todd, W. E., 1969. Reconnaissance geologic maps and sample data, Teller A-1, A-2, A-3, B-1, B-2, B-3, C-1, and Bendeleben A-6, B-6, C-6, D-5, D-6 quadrangles, Seward Peninsula, Alaska: U.S. Geological Survey open-file report, 49 p.

SAMS, 2005. Spectral Analysis and Management System, <sams.projects.atlas.ca.gov>, 25 October 2013.

Santamarina, J.C., Klein, K.A., Wang, Y.H., Prencke, E., 2002. Specific surface: determination and relevance, Canadian Geotechnical Journal, 39, 233-241.

Schwering, P. C., Karlin, R. E., 2012. Structural interpretation and modeling of the Dixie Meadows geothermal prospect using gravity and magnetic data, Geothermal Resources Council Transactions, 36, 53-58.

Shepherd, R. G., 1989. Correlations of Permeability and Grain Size, Ground Water, 27, 5, 633-8.

Swenson, R.F., Wartes, M.A., LePain, D.L., Clough, J.G., 2012. Fossil fuel and geothermal energy sources for local use in Alaska: Summary of available information, Special Report 66, State of Alaska DNR, Division of Geological & Geophysical Surveys.

Till, A. B., Dumoulin, J.A., 1994. Geology of Seward Peninsula and Saint Lawrence Island, The Geology of Alaska, The Geology of North America, 141-152.

Till, A. B., Dumoulin, J. A., Werdon, M. B. Bleick, H. A., 2011. Bedrock geologic map of the Seward Peninsula, Alaska, and accompanying conodont data, US Department of the Interior, U. S. Geological Survey.

Turner, D. L., Forbes, R. B., 1980. A geological and geophysical study of the geothermal energy potential of Pilgrim Springs, Alaska, Geophysical Institute, University of Alaska, UAF R-271, 165 p.

Turner, D. L., Swanson, S. E., 1981. Continental rifting; A new tectonic model for the central Seward Peninsula, Geophysical Institute, University of Alaska, UAG R-284, 7-36.

Turner, D.L., Swanson, S., Forbes, R. B., Maynard, D., 1979. Geologic map of the Bendeleben A-6 and eastern part of the Teller A-1 quadrangles, Alaska.

University of Alaska Fairbanks, 2012. Validation of innovative exploration techniques, Pilgrim Hot Springs, Phase 1 Final Report for the DOE Grant DE-EE0002846, September 2012, 103 p.

van Ruitenbeek, F. J.A., Cudahy, T., Hale, M., van der Meer, F. D., 2005. Tracing fluid pathways in fossil hydrothermal systems with near-infrared spectroscopy, Geology, 33, 7, 597-600.

Woodward-Clyde, 1983. Results of drilling, testing, and resource confirmation: Geothermal energy development at Pilgrim Springs, Alaska, Woodward-Clyde Report, 102 p.

Yukselen, Y., Abidin, K., 2008. Suitability of the methylene blue test for surface area, cation exchange capacity, and swell potential determination of clayey soils, Engineering Geology, 102, 38-45.

Appendix A

Spectral assessment of mineral abundances.

Table A.1: Mineral abundance for PS-12-1.

PS-12-1	
Mineral	**%**
Montmorillonite	34.18
Siderite	15.89
Kaolinite	14.22
Muscovite	6.39
Palygorskite	4.33
Magnesite	3.22
Aspectral	3.16
Muscovitic Illite	1.65
Ankerite	1.36

Table A.2: Mineral abundance for PS-12-2.

PS-12-2	
Mineral	**%**
Montmorillonite	26.57
Kaolinite	14.83
Siderite	14.64
FeMgChlorite	6.13
Muscovite	5.86
Aspectral	3.25
Palygorskite	2.51
Ankerite	2.08
Magnesite	1.75
Muscovitic Illite	1.58
MgChlorite	1.58

Table A.3: Mineral abundance for PS-12-2 core.

PS-12-2 Core	
Mineral	**%**
FeMgChlorite	19.43
Phlogopite	19.31
MgChlorite	14.34
Montmorillonite	12.64
Palygorskite	6.94
Muscovitic Illite	3.31
Muscovite	2.92
Calcite	2.4
Siderite	1.71
Ankerite	1.49
Biotite	1.27
Hornblende	1.09

Table A.4: Mineral abundance for PS-12-3.

PS-12-3	
Mineral	**%**
Montmorillonite	25.65
Siderite	18.48
Kaolinite	13.8
Aspectral	4.24
Muscovite	2.3
Muscovitic Illite	1.37
Ankerite	1.07

Appendix B

Methylene blue (MeB) titration results.

Table B.1: Estimated smectite content per sediment sample for PS-12-1.

PS-12-1				
MeB concentration: 3.742 g/L				
Duplicate sample (D)				
Sample (ft)	**Depth (m)**	**Weight (g)**	**MeB (mls)**	**%Smectite**
25-35	9	1.002	1.5	1.5%
75-85	24	1.000	1.5	1.5%
190-200	59	1.001	2.5	2.5%
400-410	123	1.003	1.0	1.0%
450-460	139	1.003	5.0	5.0%
490-500	151	1.003	3.5	3.5%
550-560	169	1.003	3.0	3.0%
550-560D*	169	1.000	3.0	3.0%
600-610	184	1.002	5.0	5.0%
650-660	200	1.000	6.5	6.5%
710-720	218	1.000	5.5	5.5%
753-763	231	1.002	5.0	5.0%
800-810	245	1.003	8.0	8.0%
850-860	261	1.000	4.5	4.5%
880-890	270	1.001	8.0	8.0%
900-910	276	1.002	7.0	7.0%
930-940	285	1.001	6.0	6.0%
960-970	294	1.000	8.5	8.5%
990-1000	303	1.000	8.5	8.5%
*D=Duplicate analysis for QC				

Table B.2: Estimated smectite content per sediment sample for PS-12-2.

PS-12-2				
MeB concentration: 3.742 g/L				
Duplicate sample (D)				
Sample (ft)	**Depth (m)**	**Weight (g)**	**MeB (mls)**	**%Smectite**
45-55	15	1.002	1.5	1.5%
125-135	40	1.003	2.0	2.0%
195-205	61	1.002	2.0	2.0%
385-395	119	1.004	2.0	2.0%
465-475	143	1.004	3.5	3.5%
495-505	152	1.003	5.0	5.0%
545-555	168	1.002	5.0	5.0%
595-605	183	1.002	8.0	8.0%
655-665	201	1.000	5.0	5.0%
705-715	216	1.001	3.0	3.0%
705-715D*	216	1.002	3.0	3.0%
745-755	229	1.002	4.5	4.5%
765-775	235	1.003	10.0	10.0%
805-815	247	1.002	6.0	6.0%
825-835	253	1.003	5.5	5.5%
855-865	262	1.002	5.0	5.0%
885-895	271	1.002	5.0	5.0%
895-905	274	1.003	5.0	5.0%
945-955	290	1.004	10.0	10.0%
965-975	296	1.002	6.0	6.0%
995-1005	305	1.002	4.5	4.5%
1025-1035	314	1.001	2.5	2.5%
1045-1055	320	1.003	1.0	1.0%
1093-1103	335	1.003	2.0	2.0%
1163-1173	356	1.000	4.0	4.0%
1193-1203	365	1.003	2.5	2.5%
1233-1243	377	1.003	9.5	9.5%
1233-1243D*	377	1.002	8.0	8.0%
*D=Duplicate analysis for QC				

Table B.3: Estimated smectite content per sediment sample for PS-12-3.

PS-12-3				
MeB concentration: 3.742 g/L				
Duplicate sample (D)				
Sample (ft)	**Depth (m)**	**Weight (g)**	**MeB (mls)**	**%Smectite**
24-34	9	1.002	3.0	3.0%
193-203	60	1.003	2.0	2.0%
393-403	121	1.002	2.5	2.5%
443-453	137	1.003	3.5	3.5%
493-503	152	1.002	3.5	3.5%
543-553	167	1.003	5.0	5.0%
593-603	182	1.004	7.5	7.5%
653-663	201	1.002	5.0	5.0%
703-713	216	1.003	7.5	7.5%
743-753	228	1.002	7.0	7.0%
813-823	249	1.001	5.0	5.0%
853-863	262	1.003	6.0	6.0%
883-893	271	1.001	7.5	7.5%
953-963	292	1.003	3.0	3.0%
953-963D*	292	1.001	3.0	3.0%
1003-1013	307	1.004	7.5	7.5%
1023-1033	313	1.003	4.0	4.0%
1083-1093	332	1.001	7.5	7.5%
1153-1163	322	1.000	4.0	4.0%
*D=Duplicate analysis for QC				

Appendix C

X-ray diffraction results of glycolated clay samples.

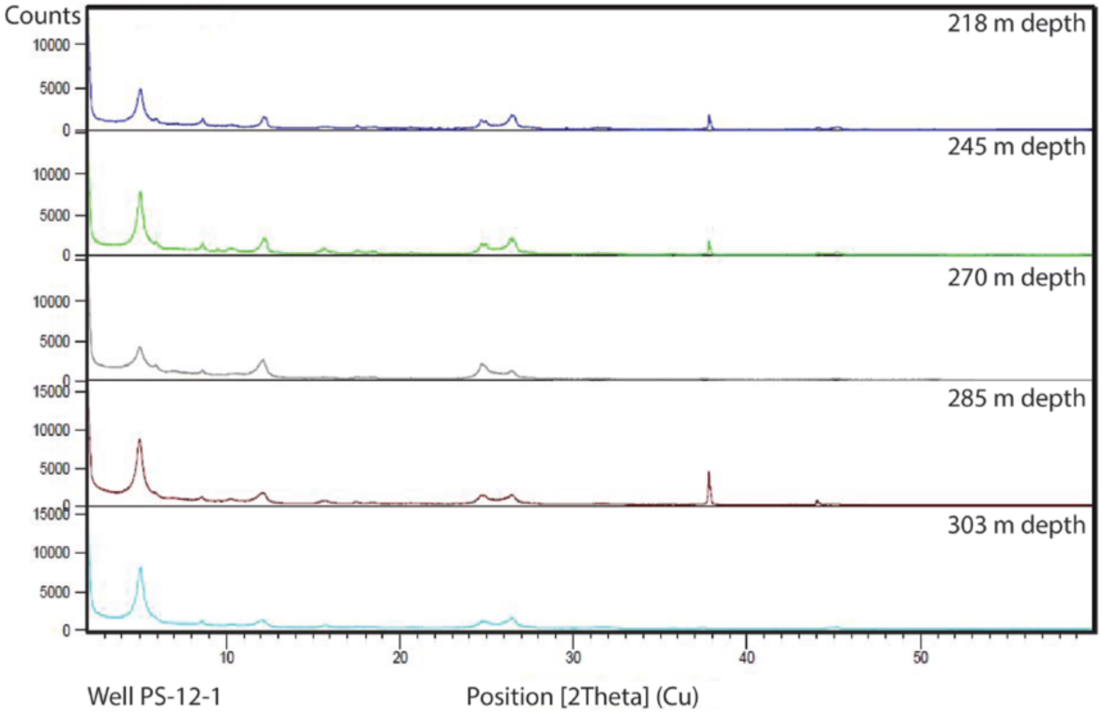

Figure C.1: X-ray diffraction results of glycolated clay samples for well PS-12-1.

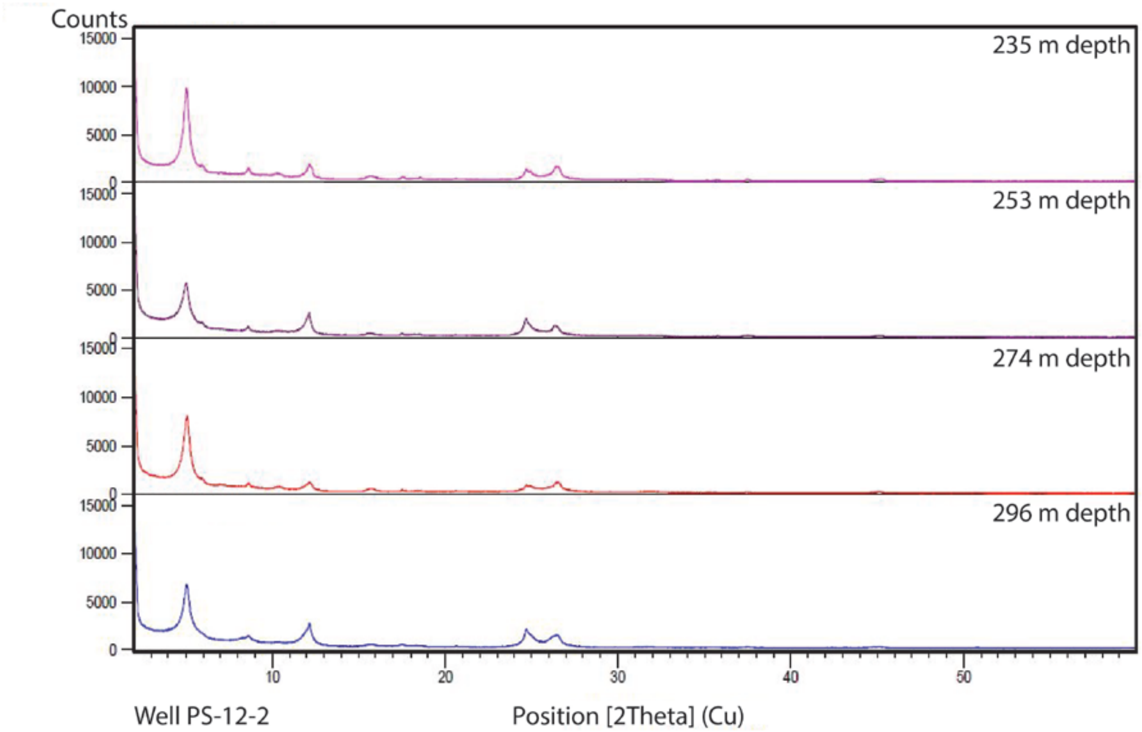

Figure C.2: X-ray diffraction results of glycolated clay samples for well PS-12-2.

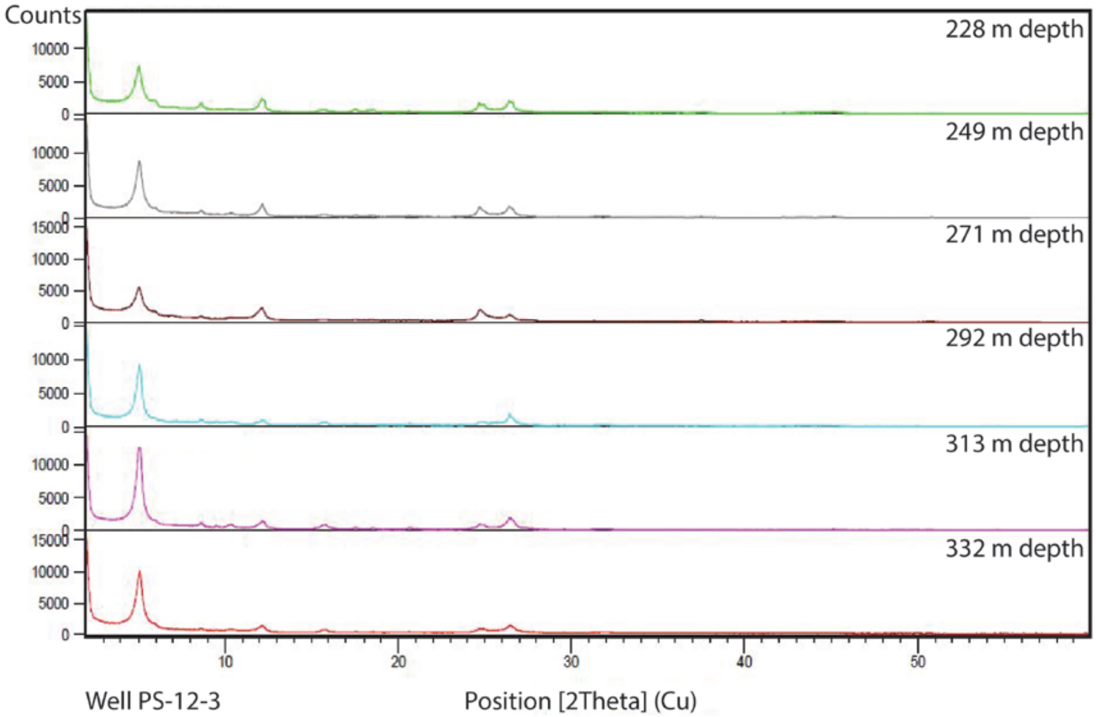

Figure C.3: X-ray diffraction results of glycolated clay samples for well PS-12-3.